The Thesis Committee for Chad Allen Greene certifies
that this is the approved version of the following thesis:

Low-Frequency Acoustic Classification
of Methane Hydrates

APPROVED BY

SUPERVISING COMMITTEE:

_____

Preston S. Wilson, Supervisor

_____

Mark F. Hamilton

_____

Richard B. Coffin

Low-Frequency Acoustic Classification of Methane Hydrates

by

Chad Allen Greene, B.S.

THESIS

Presented to the Faculty of the Graduate School of

The University of Texas at Austin

in Partial Fulfillment

of the Requirements

for the Degree of

MASTER OF SCIENCE IN ENGINEERING

THE UNIVERSITY OF TEXAS AT AUSTIN

December 2010

To Dr. Wochner.

Acknowledgments

I stood on the stepstone when school days was o'er
And longed for the time to go by
Now that it's gone, I stand here tonight
To bid this old stepstone goodbye.

Goodbye dear old stepstone, goodbye to my home
God bless the ones that I leave with a sigh
I'll cherish fond mem'ries when I am gone
To ramble this wide world alone.

I stand on my stepstone at eventide now
The wind whistles by with a moan
The fields will be whitening, but soon I'll be gone
Goodbye to my stepstone and home.

Goodbye dear old stepstone, goodbye to my home
God bless the ones that I leave with a sigh
I'll cherish fond mem'ries when I am gone
To ramble this wide world alone.

'Tis sad to be parted from those that we love
Strange faces we see every day
Each heart string of mine is broken in time
When I think of those dear ones at home.

Goodbye dear old stepstone, goodbye to my home
God bless the ones that I leave with a sigh
I'll cherish fond mem'ries when I am gone
To ramble this wide world alone.

Bascom Lamar Lunsford wrote this song about finishing school, leaving home, and taking on the world by himself. Upon the completion of my master's

degree, I feel many of his same sentiments. However, I know I won't be ramblin' this wide world alone. I know I will always have, as I have always had, the abiding love and support of my parents. Mom and Dad, you laid down the stepstones on my path toward this degree and I will forever appreciate and love you for it. Thank you for you for all that you have done for me—I certainly wouldn't be here without you. Thanks also to my advisor, Preston Wilson. Whether in class, in the lab, or at sea, you have always taken the time to help me understand acoustics, to help me be a better scientist, and to help me find my way in life. To all who have been there for me and helped me along this sometimes toiling path, thank you. God bless all of you, whom I love; God bless you, whom I leave with a sigh. Thank you to my office mates, my friends, and my professors; thank you my dear stepstones, and goodbye.

CHAD ALLEN GREENE

Low-Frequency Acoustic Classification
of Methane Hydrates

Chad Allen Greene, M.S.E.
The University of Texas at Austin, 2010

Supervisor: Preston S. Wilson

Methane hydrates are naturally-occurring ice-like substances found in permafrost and in ocean sediments along continental shelves. These compounds are often the source of cold seeps—plumes which vent methane into aquatic environments, and may subsequently release the potent greenhouse gas into the atmosphere. Methane hydrates and methane gas seeps are of particular interest both for their potential as an energy source and for their possible contribution to climate change. In an effort to improve location of hydrates through the use of seismic surveys and echo-sounding technology, this work aims to describe the low-frequency (10 Hz to 10 kHz) acoustic behavior of methane gas bubbles and methane hydrates in water under simulated ocean-floor conditions of low temperatures and high pressures. Products of the experiments and analysis presented in this thesis include (a) passive acoustic techniques for measurement of gas flux from underwater seeps, (b) a modified form of Wood's model of low-frequency sound propagation through a bubbly

liquid containing real gas, and (c) low-frequency measurements of bulk moduli and dissociation pressures of four natural samples of methane hydrates. Experimental procedures and results are presented, along with analytical and numerical models which support the findings.

Table of Contents

x

List of Tables

List of Figures

List of Symbols and Abbreviations

a	van der Waals constant given by Eq. 3.19
atm	atmospheres hydrostatic pressure, 1 atm = 101,325 Pa
b	van der Waals constant given by Eq. 3.19
B	bulk modulus, $B = \kappa^{-1}$
B_h	bulk modulus of hydrate, $B_\mathrm{h} = \kappa_\mathrm{h}^{-1}$
BSR	bottom-simulating reflector
c	sound speed in a fluid
c_g	sound speed of gas
$c_\mathrm{g,0}$	sound speed of gas at STP
c_h	sound speed of hydrate
c_l	sound speed of a liquid
c_m	low-frequency sound speed of a mixture
$c_\mathrm{m,f}$	freefield low-frequency sound speed of a mixture
$c_\mathrm{m,m}$	measured low-frequency sound speed of a mixture
c_n	sound speed corresponding to mode n
CH_4	methane
C_2H_6	ethane
C_3H_8	propane
C_4H_{10}	butane, isobutane
CM	Cascadia Margin
d	depth
d_i	inner diameter
d_o	outer diameter
D_g	thermal diffusivity of gas
DAQ	data acquisition system
f	frequency in Hertz
f_0	resonance frequency in Hertz
f_1	lower resonance frequency in Hertz
f_2	higher resonance frequency in Hertz
f_meas	measurement frequency
f_n	frequency corresponding to mode n
f_s	recording sampling rate

$F_\text{px-mm}$	pixels-to-millimeters conversion factor
FFT	fast Fourier transform
g	gravity
G	shear modulus
GHSZ	gas hydrate stability zone
GM	Gulf of Mexico
h	liquid column height
HFR	high flow rate
HM	Håkon Mosby
i	index
j	$\sqrt{-1}$
k	stiffness
k_a	equivalent acoustic stiffness
k_m	mechanical stiffness
l	shape mode number
L	resonator tube length
LED	light-emitting diode
LFR	low flow rate
m	mass
m_a	equivalent acoustic mass
m_h	mass of hydrate sample
m_m	mechanical mass
M	molecular mass
n	mode number
N	total number of elements in an array
N_2	nitrogen
N_b	total number of bubbles
p	acoustic pressure
P	absolute hydrostatic pressure
P_atm	atmospheric pressure
P_c	critical pressure
P_r	reduced pressure
$P_\text{d,DQH}$	methane hydrate dissociation pressure
$P_\text{d,PP}$	methane hydrate dissociation pressure
PVC	polyvinyl chloride
r	distance from a source
r_0	equilibrium bubble radius

r_a	major radius of ellipse
r_b	minor radius of ellipse
r_l	relative amplitude of oscillation
RTD	resistance temperature detection
R	universal gas constant ≈ 8.314472 J[K mol]$^{-1}$
sI	hydrate structure I
sII	hydrate structure II
sH	hydrate structure H
S	salinity
S_l	spherical harmonic for shape mode l
SF_6	sulfur hexafluoride
SNB	simulated natural bottom
SPL	sound pressure level
STP	standard temperature and pressure
t_b	duration of analysis window
$t_{i,0}$	analysis window start time
$t_{i,\mathrm{end}}$	analysis window end time
T	temperature [K]
T_c	critical temperature
T_r	reduced temperature
V	volume
V_b	bubble volume
V_g	volume of gas
V_h	volume of hydrate sample
V_l	volume of liquid
V_m	volume of mixture
V_os	volume of an oblate spheroid
V_sphere	volume of a sphere
V_thresh	signal voltage amplitude threshold
V_tot	total gas volume
VSA	vector signal analyzer
w	numerical element index
W	power spectral density
Y	amplitude vector of recorded signal
Z	compressibility factor
β	generalized void fraction given by Eq. 3.1

β_{g}	gas void fraction given by Eq. 3.2
β_{h}	hydrate volume fraction given by Eq. 4.1
γ	ratio of specific heats
δ	delta function
ΔL	change in resonator column length
ζ	damping coefficient given by Eq. 3.8
κ	compressibility
κ_{g}	compressibility of gas
κ_{h}	compressibility hydrate sample
κ_{l}	compressibility of liquid
κ_{m}	compressibility of mixture
λ	acoustic wavelength
μ	viscosity
μ_{l}	liquid viscosity
ν	polytropic index
ρ	density
ρ_{g}	density of gas
$\rho_{\mathrm{g},0}$	density of gas at STP
$\rho_{\mathrm{g},\mathrm{c}}$	critical density
ρ_{h}	density of hydrate
ρ_{l}	density of fluid surrounding a bubble
ρ_{m}	density of fluid a mixture
σ	surface tension
Φ	argument given by Eq. 2.3
χ	argument given by Eq. 2.4
ω	angular frequency
ω_0	angular acoustic resonance frequency
$\omega_{0,\mathrm{m}}$	angular mechanical resonance frequency
$\Im$	imaginary part mathematical operator
$\Re$	real part mathematical operator
$\wp(r_0)$	number of bubbles per unit volume

Chapter 1

Introduction

It has been shown that levels of atmospheric methane, particularly from latitudes 65°N to 70°N, have been rising in recent decades [1]. This increase has been linked to an acceleration of methane ebullition from thermokarst, or thaw, lakes and offshore marine environments [2, 3]. It is suspected that two major sources of the gas include destabilization of subsurface methane hydrates and production of methane resulting from the thawing of organic matter contained in permafrost; however, controversy exists over the extent to which these sources contribute to atmospheric methane levels [4–8]. This debate is fueled in part by significant discrepancies in estimates of global quantities of gas hydrates, which currently span several orders of magnitude [9–14]. Methane is a potent greenhouse gas, having the ability to trap as much as 25 times the solar energy of carbon dioxide by molecule, and thus, it is of particular interest in the fragile arctic environments which drive global climates [15]. Furthermore, both of the aforementioned major sources of arctic methane ebullition—hydrate dissociation and thaw-induced methane production—are highly sensitive to increases in local temperatures [16]. Implications are that natural or anthropogenic increases in arctic temperatures could potentially trigger a positive-feedback loop of arctic warming and global climate change [17–19].

In addition to climate research, interest in underwater gas seeps lies in their potential for exploitation as a fuel source [20]. Methane is high in energy, and, if economically feasible to capture, could help reduce our dependence on oil. In an effort toward the development of a multimodal remote sensing system for monitoring methane ebullition in underwater environments, this thesis explores new acoustic techniques for measurement of underwater gas content and determination of hydrate stability. Presented here are three laboratory experiments in which (a) bubble sizes were measured by analyzing the sounds they radiated at birth, (b) sound speeds of bubbly liquids containing ideal and real gases were measured as a function of hydrostatic pressure and gas volume fraction, and (c) bulk moduli and dissociation pressures of four natural gas hydrate samples were measured through active acoustic means.

1.1   Road Map of Thesis

The first acoustic technique described in this thesis uses passive recording of a model methane seep to measure its gas flow rate. Background and motivation for the experiment are presented in Ch. 2 with a detailed description of measurement procedures and acoustic methods developed for this work. Results of a laboratory evaluation of the new methods are presented and discussed. Chapter 3 highlights the need for a better understanding of the acoustic behavior of bubbly liquids which contain non-ideal gases such as methane at depth in aquatic environments, and a modified form of Wood's model is developed to account for the real-gas behavior of such a medium. An ex-

perimental procedure and results showing notable accuracy of the model are presented. Chapter 4 describes an experiment in which an acoustic resonator in a temperature- and pressure-controlled chamber designed for this work was used to measure the bulk moduli and stability regimes of natural structure I and structure II methane hydrate (defined in Sec. 4.1) samples.

Attempts have been made to use intuitive notation and nomenclature consistent with current literary conventions throughout this thesis. For clarity, a list of symbols and abbreviations is given on page xv. Supplemental materials, including figures, experimental data logs, physical models, and computer codes developed by the author for this work, are provided in the Appendix.

Chapter 2

Passive Acoustic Gas Flux Measurement

2.1 Review of Literature

It is well known that a gas bubble will radiate sound as it is released into a fluid. In 1901, Osborne Reynolds published a study of the sound produced by boiling water, setting off what has become more than a century of research on the acoustics of bubbles [21]. His simple curiosity about the noisy kettle in his kitchen has led to our understanding of many physical phenomena including cavitation and sonoluminescence [22–24]. Despite extensive investigations into these complex phenomena, the simple use of passive acoustics as a method of measuring bubble sizes has still only existed in theory or in preliminary tests. The literature shows that gas quantification using passive acoustic techniques has been explored by a handful of groups who have attempted to introduce the methods for use in their respective fields. In 1948, sonar researchers Knudsen et al. correlated wind speed with underwater ambient noise levels, crediting bubbles created by breaking waves as the primary source of noise in the ocean [25]. In 1981, Betteridge et al. successfully monitored gas production during chemical reactions by analyzing acoustic recordings obtained by a hydrophone placed in various samples [26]. Building on this work, Boyd and Varley used a hydrophone in an industrial agitator to measure bubble size dis-

tributions in a fermentation vessel [27]. In laboratory experiments aimed at developing a bubble sizing system for industrial applications, Manasseh et al. found that for some cases it may be possible to estimate the spatial distribution of void fractions in liquids using passive acoustic techniques [28]. In 2010, Greene and Wilson presented early results from laboratory experiments which found acoustic recording of air bubbles released from an underwater needle to be a highly accurate method of gas flux measurement [29].

To the knowledge of the author, only two in situ measurements of gas ebullition in natural environments using acoustic recordings have been attempted. In a 1987 paper, Leighton and Walton proposed an undergraduate-level physics experiment in which students would use a hydrophone to record the sounds of a babbling brook and analyze the recordings to estimate the sizes of the entrained bubbles [30]. In 2007, Leifer and Tang performed the only known passive acoustic measurement of methane flux from an underwater seep, finding agreement with other gas quantification techniques within 20% [31].

The relatively low number of studies of passive acoustic techniques for measurement of bubble volumes, particularly pertaining to natural gas seeps, begs further research into the methods. Moreover, the potential exists for these techniques to produce highly accurate measurements. After a study of the shapes of gas bubbles which form at underwater nozzle tips, Longuet-Higgins et al. concluded that "the frequency of the acoustical pulse emitted by the bubble, which is simply related to its radius, may be the most accurate indicator of its size, and more convenient than flash photography" [32]. With
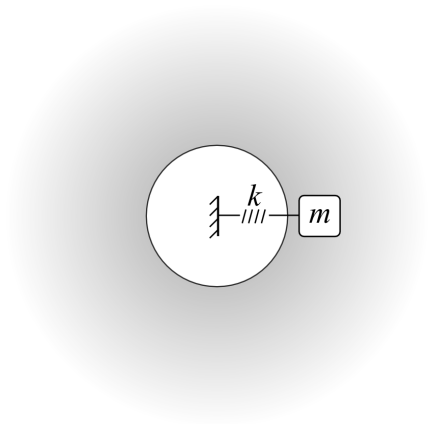
Figure 2.1: Schematic of mechanical analogue to the acoustic resonance of a bubble.

this in mind, a method of measuring underwater gas flux using passive techniques which exploit the acoustic resonance of bubbles was developed and is described here.

2.2 Development of Models

Minnaert described the acoustic resonance frequency, ω_0, of a spherical bubble, which we can derive using an analogy to a mechanical system, as shown in Fig. 2.1 [33]. If we consider the gas inside the bubble to act as a mechanical spring with stiffness, k, and the fluid just outside the bubble to act as a mass, m, we know the resonance frequency of the mechanical spring-mass system to be

$$\omega_{0,\mathrm{m}} = \sqrt{\frac{k_\mathrm{m}}{m_\mathrm{m}}},\tag{2.1}$$

where subscripts m denote mechanical properties. At resonance in our acoustic system, stiffness is governed by the force exerted on the bubble over its surface [34]. Assuming the fluid inside our bubble is an ideal gas, we can use Hooke's law to obtain an expression for its "acoustic stiffness," which we find to be $k_\mathrm{a} = 12\pi\nu r_0 P$, where r_0 is the equilibrium radius of the bubble and ν is the polytropic index of the gas such that

$$PV^\nu = \text{constant.} \tag{2.2}$$

An investigation into the thermodynamic behavior of the fluid inside the bubble reveals that the polytropic index ranges from unity for isothermal processes to the ratio of specific heats (1.4 in the case of air) for adiabatic processes. In our bubble, gas particles adjacent to the bubble wall behave isothermally due to their proximity to the outer fluid which acts as a heat sink, while particles at the center of the bubble transfer a negligible amount of heat energy due to symmetry. The majority of gas particles in the bubble, however, are neither on the surface nor at the very center of the bubble. Thus, we must use Prosperetti's expression to determine an effective polytropic index for the entire bubble. En route to determining the polytropic index, Prosperetti defines an argument, Φ, which will become useful in Ch. 3. The argument is given by

$$\Phi = \frac{3\gamma}{1 - 3(\gamma-1)i\chi[(i/\chi)^{1/2}\coth(i/\chi)^{1/2} - 1]}, \tag{2.3}$$

where γ is the ratio of specific heats,

$$\chi = \frac{D_\mathrm{g}}{\omega r_0^2}, \tag{2.4}$$

7

and D_g is the thermal diffusivity of the gas [35]. Now the effective polytropic index, ν, for the bubble is given by

$$\nu = \frac{1}{3}\Re(\Phi). \tag{2.5}$$

Continuing with the mechanical spring-mass system analogy, we can obtain an expression for effective mass of the liquid outside the bubble. In our acoustic system, we will call this mass m_a. Assuming radiation mass dominates, and assuming the system is in a long-wavelength regime such that $r_0 \ll \lambda$, where λ is the acoustic wavelength, we find that the radiation mass is related to the volume of the spherical bubble as $m_\mathrm{a} = 4\rho_\mathrm{l}\pi r_0^3$, where ρ_l is the density of the fluid surrounding the bubble [34]. Using these expressions with Eq. (2.1), we obtain an expression for the acoustic resonance of a spherical bubble of ideal gas in a liquid host,

$$\omega_0 = \frac{1}{r_0}\sqrt{\frac{3\nu P}{\rho_\mathrm{l}}}. \tag{2.6}$$

Equation (2.6) is a valid approximation for the resonance frequency of a bubble whose surface tension can be neglected. If, however, the bubble is small ($r_0 > 0.1$ mm for air bubbles in water), or the fluid properties are such that surface tension, σ, must be included, the expression for resonance frequency becomes

$$\omega_0 = \sqrt{\frac{1}{3\rho_\mathrm{l}r_0^2}\left[3\left(\nu P + \frac{2\gamma\sigma}{r_0}\right) - \frac{2\sigma}{r_0}\right]} \tag{2.7}$$

[36]. To solve for r_0, this relation warrants numerical methods, and thus, it is generally preferred to neglect surface tension when appropriate, and rearrange

8

Eq. (2.6) to solve for r_0 analytically. In the analysis of the current data, gas volumes are calculated using both Eq. (2.6) and Eq. (2.7) for comparison.

The aim of this work is to exploit the sound produced by newborn bubbles as a method of measuring bubble volumes, and ultimately, to use this method to determine gas flow rates. Physical theory supporting the concept has been known for decades; however, the literature shows only one experiment in which the theoretical model has been applied to real-world gas flux measurement. Leifer and Tang passively recorded the radiated acoustic signal from a natural marine methane seep and measured gas flux with approximately 20% error [31]. Their results support the validity of passive acoustic techniques for measurement of methane ebullition, while warranting laboratory experiments for further development and model calibration for use in natural environments.

When a bubble is released into a fluid, it must break free of forces constraining it. During this process, the bubble is acoustically excited in a manner akin to a guitar string being plucked. This work attempts to passively record the acoustic signals generated by young bubbles, determine resonance frequencies of the bubbles, and use Eq. (2.6) or Eq. (2.7) to relate these frequencies to bubble volumes. It should be noted that Eqs. (2.6) and (2.7) have been derived for spherical bubbles, but bubbles found in nature do not necessarily take this geometry. However, Strasberg showed that the pulsation frequency of a bubble is dominated not by its shape, but by its volume [37]. Therefore, in our tests we will use the acoustic resonance frequency of a bubble to determine the equilibrium radius, r_0, of a spherical bubble having the same resonance

9

frequency. The volume, V_b, of the bubble will be calculated as the volume of a spherical bubble of radius r_0. Accuracy of the bubble volume measurement is maintained despite the assumption that the potentially nonspherical bubble is spherical, because we know that the pulsation frequency of a bubble is primarily a function of bubble volume. A final expression for bubble volume as a function of its resonance frequency, f_0, in Hertz, can be derived by solving Eq. (2.6) for the equilibrium bubble radius, and inserting this expression into the formula for the volume of a sphere. The calculation yields

$$V_b = \frac{1}{6\pi^2 f_0^3} \left[\frac{3\nu P}{\rho_l} \right]^{3/2} . \tag{2.8}$$

If surface tension cannot be neglected, Eq. (2.7) must be solved numerically for equilibrium radius, r_0, then the bubble volume can be calculated using the formula for the volume of a sphere, $V_{sphere} = \frac{4}{3}\pi r_0^3$. Total gas flux may be measured by summing the calculated volumes of individual bubbles over time.

2.3 Experimental Design

For this work, a tabletop apparatus was constructed for generating bubbles and recording their radiated acoustic signals. A 35 cm × 35 cm × 13 cm tank with 6.25 mm thick walls was filled with distilled water. Medical-grade breathing air was directed through copper tubing into a 10 cm long, 26 gauge (0.254 mm inner diameter, 0.457 mm outer diameter), vertically-oriented, stainless steel needle placed at the bottom of the tank. A small

hydrophone (Brüel & Kjær 8103) was placed 26 mm from the needle tip, oriented approximately 30° off-vertical, pointed at the needle tip, as shown in Fig. 2.2. Due to the similar acoustic impedances of the hydrophone cable and the water surrounding it, the cable was housed in a stainless steel sheath in an attempt to decouple it from the acoustic system. The hydrophone signal was conditioned with a low-noise Brüel & Kjær 2692 charge amplifier then bandpass filtered using Krohn-Hite model 34A filters and recorded using a National Instruments USB 6211 data acquisition system (DAQ) connected via USB to a personal computer with a LabVIEW interface.

As a simultaneous, independent measurement of gas flux, a gas trap was created by placing an inverted water-filled graduated cylinder over the area of surfacing bubbles, with its open end approximately 1 cm below the surface of the water. Gas flow was measured by reading the change of water level in the cylinder over the time of acoustic recording.

A third measurement of gas flow was obtained optically. A camera with a shutter speed of 1/1000 s was attached to a stereo microscope placed along the broad side of the tank and video was recorded at 30 frames per second as an avi file without compression, using a LabVIEW interface. A schematic of the complete experimental apparatus is shown in Fig. 2.2.

2.4   Optical Measurements

During each acoustic recording, an avi-formatted video was captured at a rate of 30 frames per second. An example of a still image from one such
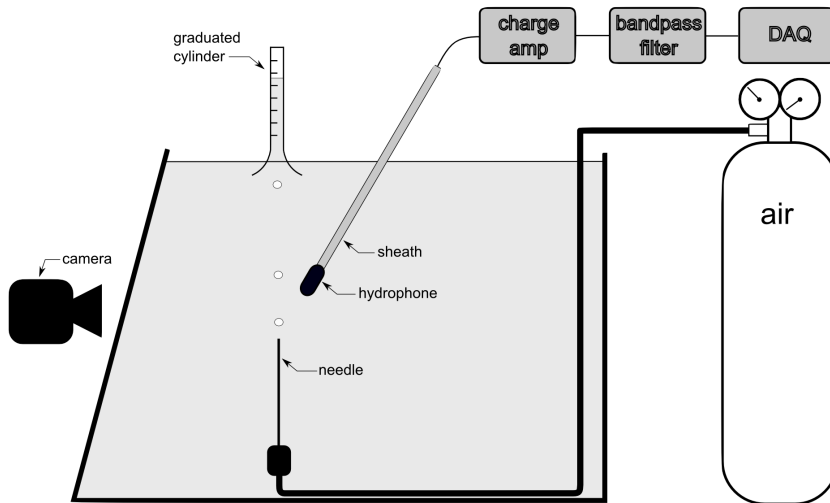
Figure 2.2: Schematic of experimental apparatus for passive acoustic gas flux measurements.

recording is shown in Fig. 2.3. Note that the bubble shell appears blurry—this may be due to the bubble pulsations which have motivated this work. Despite the high speed of the camera, the bubble underwent two to three acoustic cycles during the 1 millisecond the shutter was open to capture this image, thus blurring the edge of the bubble in the still.

For this work, a Matlab script has been developed to import frames of the video singly, determine whether a bubble is present in the image, outline the bubble if it is present, and fit an ellipse to the bubble outline. The script then calculates the volume of the bubble, assuming it is an oblate or prolate spheroid of major and minor radii r_a and r_b, respectively, which are taken as the major and minor radii of the fitted ellipse. The volume of the spheroid is then calculated as $V_{os} = \frac{4}{3}\pi r_a^2 r_b$. The tip of the needle, visible at the bottom
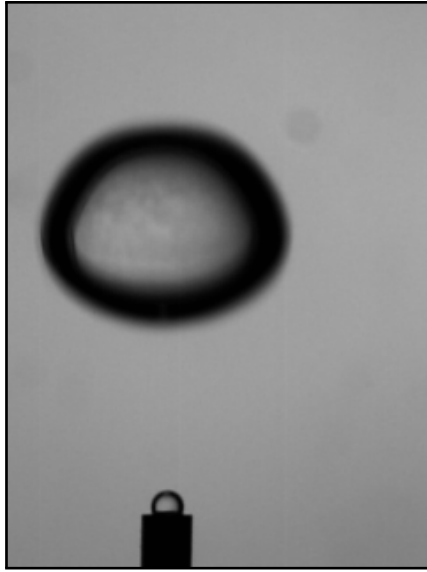
Figure 2.3: Still image of a young bubble during passive acoustic measurement. The needle tip is visible at the bottom of the frame.

of the frame, is used as a size reference to find $F_{\text{px-mm}}$, the factor of conversion from pixels to millimeters. The code written for this calculation is given in Appendix D.1.

Four potential sources of error have been identified for these optical measurements. The first is that the shape of each bubble is approximated as a spheroid with perfect symmetry about a vertical axis. Extensive analysis of bubble images has led the author to conclude that any asymmetry about the centerline is small enough that it may be neglected; however, it was observed that bubbles often took the shape of a superellipsoid whose exact dimensions are difficult to determine by automated image analysis. A least-squares method was employed to estimate the accuracy of fitting ellipses to

13

bubble profiles, showing that the practice of approximating bubble shapes as spheroids may result in as much as 4% volume calculation error for low gas flow rates. In the case of high gas flow rates, where bubbles tend to contort upon breaking free of the needle tip, as much as 12% error in bubble size calculation was found.

Second, the resolution of the camera limits the resolution of bubble size measurement. A major radius of the bubble may be 80 pixels in length, giving rise to the potential for approximately $\pm 1.3\%$ error in axis length measurement if the outline of the bubble is taken as one pixel greater or less than its true extent. This error is squared in the calculation of the volume of a shperoid. A potentially more significant source of resolution error may be the use of the needle tip as a size reference. The needle tip appears in the frame as approximately 20 pixels in diameter, implying that there may be as much as $\pm 10\%$ error in the factor of conversion from pixels to millimeters. Such an error would result in significant inaccuracies of the optical bubble size measurements.

A third possible source of error in the optical measurements relates to the depth of field of the camera. In actuality, $F_{\text{px-mm}}$ does not remain constant in horizontal or vertical space throughout the frame. The conversion factor is measured near the bottom of the frame, while the bubble may appear close to the needle tip, in the center of the frame, or near the top of the frame. Further-more, the size reference is only taken in the horizontal direction—depending on the optics and data acquisition system, it is possible that $F_{\text{px-mm}}$ is not a true measure of the conversion factor in the vertical dimension. Laboratory

calibrations using a fixed scale placed throughout the frame found that objects near the top of the frame may appear as much as 10.2% larger than actual size.

Finally, some bubbles rise out of the frame before they are captured by the camera. To account for this, in each measurement the average volume of the bubbles which fell fully within the video frame was calculated and multiplied by the known total number of bubbles during the measurement period. This "fix" assumes a uniform bubble size distribution, which was confirmed using acoustic methods. Furthermore, the number of bubbles which were not captured on video was small relative to the number which were optically measured. Thus, it can be assumed that the magnitude of this fourth potential source of error is negligible.

In total, the maximum potential error associated with the optical methods of measuring gas flux in this experiment may be found by taking the product of the individual maximum error factors in the series. For the case of a low gas flow rate, optical methods may measure as low as 14.7% below or as high as 27.7% above the actual value. If the flow rate is high, optical measurements may underestimate volumes by as much as 21.8% or overestimate by as much as 37.5%.

2.5   Graduated Cylinder Measurements

A measure of total gas volume exiting the needle over the duration of each experiment was obtained by capturing the gas in a water-filled in-

verted graduated cylinder placed above the source of ebullition. Volume was measured by observing the meniscus level at the beginning and end of each acoustic recording. For measurements where gas flow rates were high, bubbles did not surface in a consistent location due to turbulent flow generated by the bubbles. In these tests, a thin sheet of plastic was cut, rolled, and affixed to the open end of the graduated cylinder to act as a funnel, directing bubbles into the gas trap.

Two known potential sources of error are associated with the graduated cylinder measurement technique. First, bubbles may linger for some time at the air-water interface inside the graduated cylinder, making the meniscus difficult to discern by sight. Readings may have been inaccurate by as much as 0.2 ml at the start and end of each recording, resulting in as much as $\pm 20\%$ error for the low gas flow rate case (where a total of 2 ml of gas was measured) and $\pm 5.6\%$ error for the case of high flow rate (where a total of 7.1 ml of gas was measured).

Second, it was desired to record and analyze a steady-state flow of bubbles, uniform in size and periodically occurring in time. For this, it was necessary to allow the gas flow to fully develop before the start of each recording. As a result, some bubbles were present in the tank at the start of each acoustic recording, and these bubbles were captured and recorded in the gas trap, but were not recorded acoustically. Likewise, some bubbles were present in the tank at the end of each acoustic recording—these bubbles were recorded acoustically, but were not measured in the gas trap. The discrepancy between

16

the number of bubbles captured acoustically and the number captured by the inverted graduated cylinder did not exceed two in any recording. Each of the recordings presented in this thesis contained several hundred bubbles, and thus, this potential source of error is neglected.

2.6   Acoustic Measurements

Due to heat generated by a 500 watt lighting system used for the video recordings, it was observed that water temperature steadily increased throughout the duration of the laboratory experiments. Given the thermal dependence of sound speed, temperature was measured using a resistance temperature detection (RTD) probe with digital readout at the time of each recording.

To account for any thermally-driven changes in tank resonances, an acoustic transfer function measurement was performed before each recording. In these transfer function measurements, the water in the tank was excited by a piston attached to an LDS-V101 shaker driven with a Crown Power Base 3 power amplifier. An HP89410A vector signal analyzer generated a periodic chirp from 100 Hz to 9 kHz and measured the transfer function between the source and the hydrophone. A schematic of this transfer function measurement is provided in the Appendix as Fig. A.1. In all recordings described in this thesis, the resonance frequencies of the bubbles were far from any significant tank resonances. Transfer function measurements confirmed that thermally-driven changes in tank resonances were minor and may be neglected.

Errors associated with acoustic measurements stem from two primary

sources—finite resolution bandwidth of the frequency analysis and the approximation of spherical bubble oscillation. The data acquisition system used in this experiment digitized the hydrophone signal at a sampling rate of 50 kHz. Given this high sampling rate, aliasing or other frequency-related errors were not expected to arise during the acquisition and recording processes. However, in data analysis, the frequency resolution achieved after fast Fourier transform (FFT) is limited by the length of the analyzed time window. Zero-padding is a helpful technique for increasing the frequency resolution of an FFT, however this benefit comes at the expense of amplitude resolution. After zero-padding, resolution bandwidth was 6 Hz for recordings of low gas flow rates, resulting in a volume measurement accuracy within 0.2%. For higher flow rate tests, the shorter time between bubbles yielded a resolution bandwidth of 12 Hz, resulting in gas volume measurement accuracy of within 0.5%.

A marginally more significant source of error in the acoustic measurements presented in this thesis may arise from the approximation that the bubbles are spherical in shape and pulsate omnidirectionally. Image analysis of bubbles generated by the experimental apparatus shows elliptical profiles with an average major-to-minor-radii ratio of 1.15. According to Strasberg, this should result in volume calculations of less than 0.6% below actual values [37].

2.6.1 Low Flow Rate (LFR) Passive Recording

In the first measurement, deemed *LFR*, for *low flow rate passive recording*, pressure to the needle was set low (~ 2 psia) using a dual-stage pressure

regulator to allow for a slow, steady flow rate of approximately one bubble, 2 mm to 3 mm in diameter, per second. The hydrophone signal was filtered with a high-pass filter set to 1.3 kHz and a low-pass filter set to 4.5 kHz before acquisition.

A Matlab script, given in Appendix D.2, has been developed to measure gas flux from acoustic recordings of bubbles breaking off of a needle. Analysis in the code begins by distinguishing between individual bubbles in a recording by amplitude thresholding. For each bubble instance, i, an analysis window begins at time $t_{i,0}$, which corresponds to the time the absolute value of the signal voltage exceeds a certain threshold, V_{thresh}. The window of analysis ends at time $t_{i,\text{end}}$, which is defined as $t_{i,\text{end}} = t_{i,0} + t_b$, where t_{b} is a fixed time, picked as the maximum time between bubbles in the recording such that $f_s(t_{i,\text{end}} - t_{i,0}) + 1$ is an integer power of two, where f_{s} is the sampling rate of the recording. Maximizing the duration of the analysis window allows for the best possible resolution in the frequency domain and constraining the length of the window array to integer powers of two minimizes the time required to compute the FFT.

After the script has detected a bubble instance and assigned a time window corresponding to the signal, an FFT is performed on the window using using the prepackaged `fft.m` algorithm in Matlab. Numerically, the FFT is computed as

$$\text{FFT} = \sum_{w=1}^{N} Y(w) \exp[-j2\pi(f_{\text{s}} - 1)(w - 1)/N], \qquad (2.9)$$
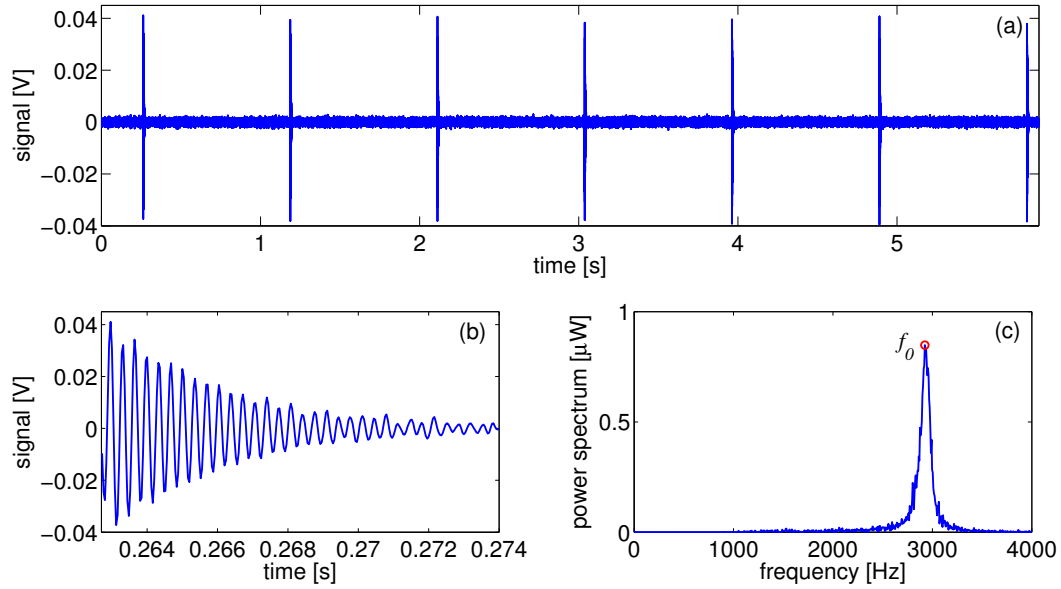
Figure 2.4: Signal and analysis of passive recording LFR. (a) First 6 seconds of recording; (b) zoomed-in plot of first recorded bubble, showing exponential decay; (c) FFT of recorded signal of first bubble.

where Y is the amplitude vector of the recorded hydrophone signal, N is the total number of elements in the array, and w is the index of the element. The power spectral density is then calculated by dividing the FFT by $N/2$ and squaring. Thus, the power spectral density is computed as

$$W(f) = \left| \sum_{w=1}^{N} \frac{Y(w) \exp[-j2\pi(f_s - 1)(w-1)/N]}{N/2} \right|^2 . \qquad (2.10)$$

Figure 2.4b shows the recorded signal of a single bubble, starting at time $t_{1,0}$ and truncated before $t_{1,\mathrm{end}}$ to show the structure of the signal. As we would expect, the signal appears to be sinusoidal, with an exponential decay in amplitude. An FFT is performed on this signal and the power spectrum is

20

plotted in Fig. 2.4c, showing a distinct resonance at approximately 2800 Hz. This resonance frequency is determined by the script using a peak-finding algorithm which was developed for ease of use and compatibility with other codes used in this work. Bubble volume is calculated by defining the peak frequency as f_0 and utilizing Eq. 2.8. It is known that Eq. 2.8 is an appropriate expression for analysis of the present data because surface tension may be neglected for the bubble sizes and fluid properties seen in passive recording LFR. For verification, bubble volumes were also calculated with suface tension included—by solving Eq. 2.7 numerically for r_0 then calculating the bubble volume as the volume of a sphere of radius r_0. It will be shown that effects of surface tension are negligible in this experiment.

In the acoustic measurements, the volume of a bubble is calculated using data obtained when it is radiating sound—when the bubble is just above the needle tip. For comparison to the graduated cylinder data, volumes obtained acoustically must be corrected to account for the volume change resulting from the pressure differential related to the bubbles' change in depth. Assuming the bubble is of an ideal gas whose volume is inversely related to pressure, we know the bubble volume to be $V = (P_\infty/P_{\mathrm{atm}})V_{\mathrm{b}}$, where P_{atm} is atmospheric pressure. At depth, d, the hydrostatic pressure on the bubble is $P = P_{\mathrm{atm}} + \rho_l g d + 2\sigma/r_0$, where g is gravity and r_0 is the nominal radius of the bubble, so the total volume of gas measured during a recording is obtained by

$$V_{\mathrm{tot}} = \sum_{i=1}^{N_{\mathrm{b}}} \left(\frac{P_{\mathrm{atm}} + \rho_l g d + 2\sigma/r_{0,i}}{P_{\mathrm{atm}}} \right) V_{\mathrm{b},i}. \tag{2.11}$$
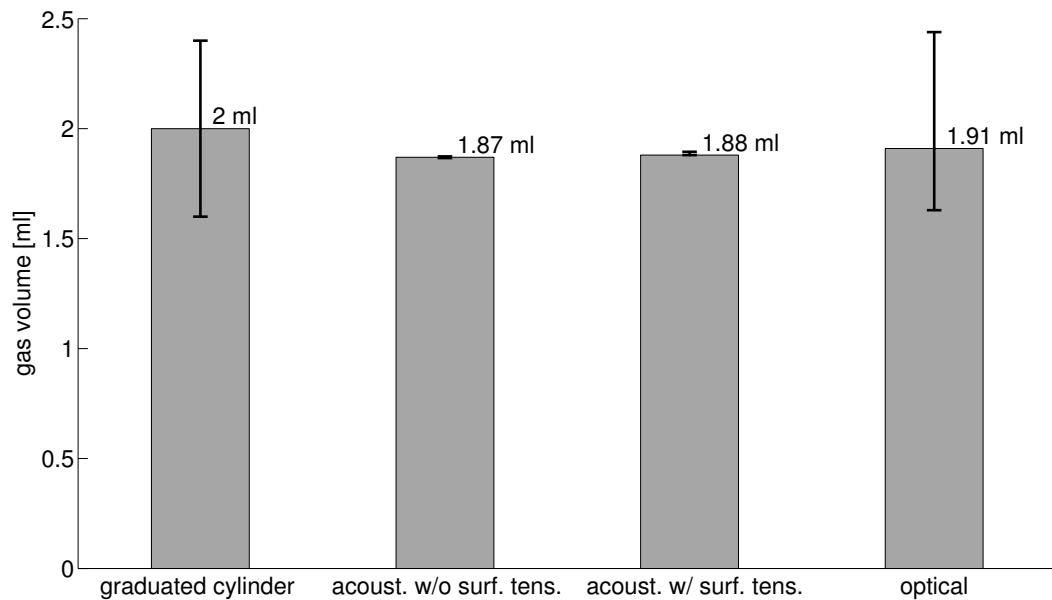
Figure 2.5: Measured and computed data for passive recording LFR: Comparison of gas flux measurements. Error bars show uncertainty associated with each measurement type, as discussed in the text. Error bars for the acoustic measurements are too small to resolve in this figure.

2.6.1.1 LFR Results

Figure 2.5 shows measured gas volumes for an LFR recording. From the acoustic recording, V_{tot} was calculated by Eq. 2.6, with surface tension neglected, and by Eq. 2.7, where surface tension was included. The two calculated values differ by less than 0.2%, confirming that for air bubbles of this size in distilled water, we can indeed neglect surface tension. Volumes obtained using optical data agree with acoustic calculations within 2%. All measured values of total gas volume for the LFR recordings are in agreement within the margins of error associated with each type of measurement. Notably, although

it was the author's original intent to use values obtained by graduated cylinder and by optical analysis as ground-truth measurements, it is evident from Fig 2.5 that the acoustic measurements likely offer the greatest accuracy in this measurement.

2.6.2 High Flow Rate (HFR) Passive Recording

A second experiment, deemed passive recording *HFR*, was performed whereby pressure to the needle was increased at the two-stage regulator, therefore increasing gas flow rate, while maintaining all other parameters of the LFR measurements. It was observed that hydrophone signal levels increased significantly with the increase in gas flow rate. Bubbles formed and broke away from the needle more rapidly than in the LFR passive recordings, but the change in gas flow rate did not appear to cause any noticeable change in bubble size by observation. An excerpt of a recording from an HFR experiment is shown in Fig. 2.6a.

During analysis of these recordings, it was found that the time between bubbles, t_{b}, was too short to obtain adequate frequency resolution in the power spectrum. To account for this, the FFT calculation was performed after padding the amplitude vector of the recorded signal with zeros such that the length of the vector became an integer power of two. It should be noted that this improvement in frequency resolution is gained at the expense of power resolution. Aside from the zero-padding adjustment, methods of analyzing HFR data did not differ from the methods used in LFR.
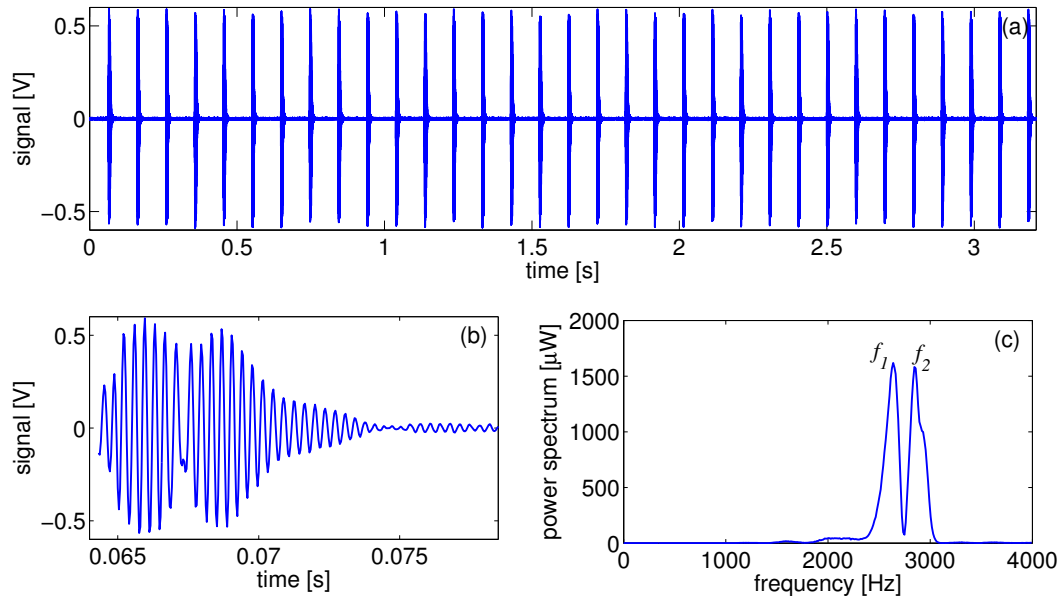
Figure 2.6: Signal and analysis of passive recording HFR. (a) First 3 seconds of recording; (b) zoomed-in plot of first recorded bubble, showing an envelope over the signal; (c) FFT of recorded signal of first bubble, showing two distinct resonances.

It is proposed that for cases where bubbles form in close succession and discerning between their acoustic signals becomes difficult, future work could investigate the possibility of computing a single power spectrum of recordings containing multiple bubble signals. Such a spectrum would contain the frequency content of the signals, which could be used to infer the bubble size distribution. Manasseh et al. argue that "for estimates of bubble size, individual bubble pulses should be stored and analyzed separately, rather than taking overall spectra" [28]. However, in analysis of acoustic recordings of breaking waves, Loewen and Melville developed methods of determining the

24

number of bubbles oscillating at a given frequency based on the known sound power radiated from a single bubble [38]. Using this method, a single acoustic recording of many bubbles would be analyzed to obtain both the frequency content of the entire recording, and the radiated sound pressure level (SPL), which may be related to the total number of bubbles as

$$\mathrm{SPL}_{N_\mathrm{b}} = \mathrm{SPL}_1 + 10 \log N_\mathrm{b}, \tag{2.12}$$

where SPL_1 denotes the sound pressure radiated from a single bubble.

2.6.2.1   HFR Results

Figure 2.6b shows an interesting phenomenon which was observed during analysis of the HFR passive recordings. An envelope appears over the signal of each bubble in these recordings. An FFT of any of these signals reveals two distinct resonances, f_1 and f_2, where f_1 is assigned to the lower frequency resonance and f_2 is assigned to the higher. It is evident that the difference frequency, $f_2 - f_1$, is equivalent to the frequency of the apparent envelope over the recorded acoustic signal. There is evidence that one of the resonances was caused by interaction with the upcoming bubble forming at the needle tip [30, 39]. Another possible explanation is that the higher-frequency resonance is the monopole resonance frequency, f_0, which is of interest in this work, while the lower-frequency resonance, f_1, may be a higher-order quadrupole or octupole mode as described by Longuet-Higgins [40, 41]. Lamb calculated the natural resonance frequencies of higher-order shape modes to

25
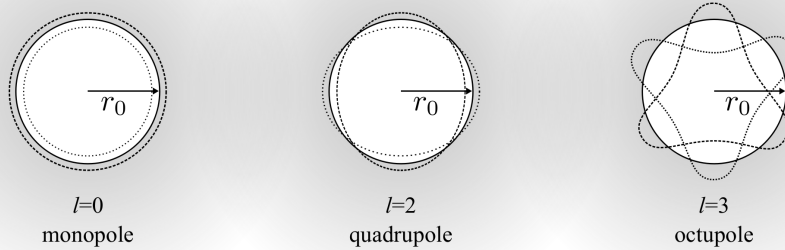
Figure 2.7: Bubble mode shapes. In 3D, bubbles are axisymmetric about their vertical centerline. The $l = 1$ dipole mode is excluded because translation offers no restoring force for oscillation.

be

$$f_l = \frac{1}{2\pi r_0}\sqrt{\frac{(l^2 - 1)(l + 2)\sigma}{\rho_1 r_0}}, \qquad (2.13)$$

where l is the mode of oscillation [42]. A diagram of select bubble shape modes is given in Fig. 2.7.

It may be possible to determine the exact mode of the f_1 resonance by measuring the pressure it radiates as a function of distance from the bubble. It is known that pressure from a monopole source decays as r^{-1}, where r is the distance from the source. However, higher order shape modes are less efficient radiators of sound compared to monopole sources. An expression for the nearfield pressure field from a source with a shape mode of oscillation, l, is given by Stasberg as

$$p_l = (l - 1)(l + 2)(\sigma/r_0)(r_l/r)(r_0/r)^l S_l, \qquad (2.14)$$

26
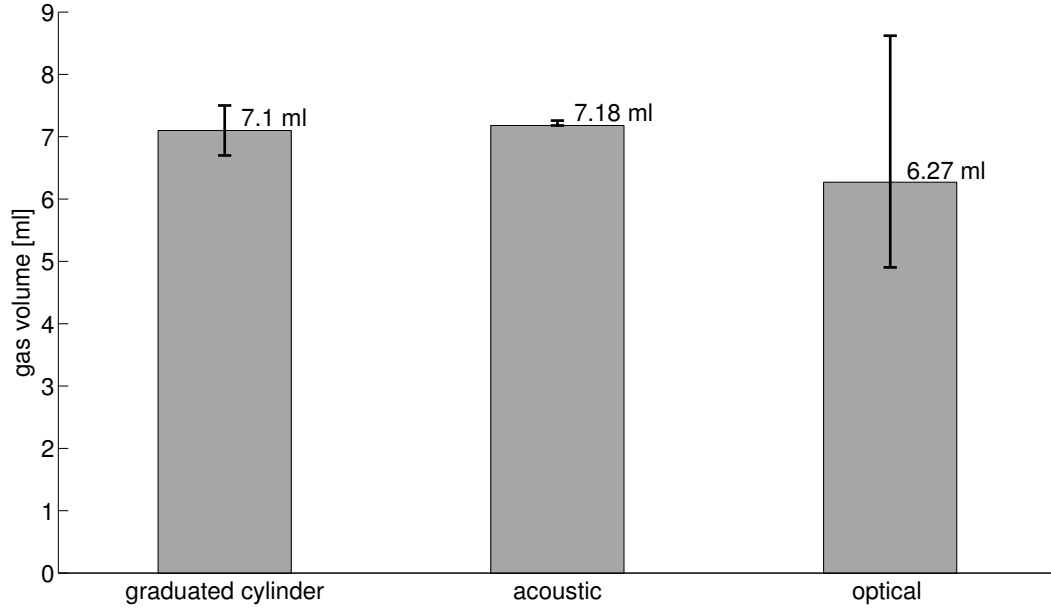
Figure 2.8: Measured and computed data for passive recording HFR: Comparison of gas flux measurements. Error bars show uncertainty associated with each measurement type, as discussed in the text. The acoustic measurement is bounded by a small error bar which extends above, but only slightly below the measured gas volume.

where r_l is the relative amplitude of oscillation and S_l is the spherical harmonic which gives the variation with angle [43].

Despite the unexplained resonance f_1, letting $f_2 = f_0$ for calculation of gas volumes using Eq. 2.8 and Eq. 2.11 yields accurate measurements of gas flux. Figure 2.8 shows gas volumes measured during an HFR recording. We see that acoustic measurements are in close agreement with measurements obtained using the graduated cylinder. Optical analysis appears to be a poor method of measuring gas flux, likely due to one or more of the potential sources

of error listed in Sec. 2.4.

2.6.3   Simulated Natural Bottom (SNB) Passive Recordings

After the successes of the acoustic gas flux measurements obtained in the LFR and HFR recordings, the laboratory experimental setup was modified to more closely mimic a natural aquatic environment. To achieve this, sand was poured into the bottom of the tank to simulate the sea floor. In the first simulated natural bottom recording (SNB1), the sand was made level with the needle tip—bubbles were released from the needle at the level of the sand surface, but did not directly interact with the sand as they broke free from the needle tip and rose. It is suspected that the process of pouring sand into the tank entrained a sufficient quantity of air to significantly damp acoustic energy in the system, leaving signal-to-noise ratios too low for analysis using the techniques described in Secs. 2.6.1 and 2.6.2.

For a second passive recording in a simulated natural bottom (SNB2), the level of the sand was raised above the needle tip, forcing the gas to find its own path through the sand before being released into the water. It was observed that bubble size and acoustic signal amplitude distributions were significantly varied in this case. As a result, algorithms developed for passive recordings LFR and HFR could not effectively discern between bubbles or measure gas flux. Furthermore, gas entrained in the sand may have affected the recorded acoustic signal. A time signal and power spectrum of an example SNB2 measurement are provided in the Appendix as Fig. A.2. It is suspected

that if the technique is refined, a single power spectrum of the entire recording, as described in Sec. 2.6.2, may yield an accurate measurement of gas ebullition for SNB1 and SNB2.

2.7 Discussion of Passive Recording Measurements

Although it was the author's original intent to test the accuracy of acoustic gas flux measurements by comparing them measurements obtained by graduated cylinder and optical analysis, results of the LFR and HFR passive recordings suggest that acoustic measurements are the most accurate of the three techniques. Video recordings provide interesting qualitative insight into bubble shapes and behavior; however, the many potential sources of error associated with optical sizing make the video unreliable for gas flux measurement. Alteration of the experimental design could potentially reduce the error associated with the graduated cylinder measurements; however, for the purpose of validating acoustics as a viable tool for measuring gas flux, the graduated cylinder measurements were sufficient. The data shows that of the three techniques used in the LFR and HFR recordings, acoustic methods yield the most accurate measurements.

The inability to obtain gas flux measurements from recordings taken in the presence of a simulated natural bottom could imply that acoustic gas flux measurements are not feasible in real-world environments. However, Leifer and Tang's success at acoustically measuring ebullition from a natural methane seep gives evidence that these measurements are possible. Furthermore, the

notable accuracy of the LFR and HFR measurements in the present work implies that there is room to improve upon the work of Leifer and Tang, who reported a measurement error of approximately 20% [31].

It is possible that the simulated natural bottom described in Sec. 2.6.3 is a poor representation of the environment surrounding a true gas seep. If a presence of entrained air in the sand is the cause of the reduced signal-to-noise ratios seen in the SNB1 and SNB2 recordings, it is reasonable to expect acoustic measurements to have higher signal levels in natural environments, where increased hydrostatic pressures tend to force gas into solution. The use of sand as the simulated natural bottom may also be poor choice of sediment, as methane deposits are often found in muds and clays [44–47]. The author intends to continue development and refinement of the acoustic gas measurement techniques presented in this thesis, and ultimately use them in a deployable multimodal remote methane sensing system.

Chapter 3

Low-Frequency Acoustics of Bubbly Liquids in a Pressure Chamber

The single-bubble resonance method of quantifying underwater methane ebullition, as described in Ch. 2, may be a useful technique for measuring low levels of gas flux. However, in higher flow rate regimes, acoustic signals radiated from individual bubbles may become difficult to distinguish. In such cases, an understanding of the acoustic properties of a lumped medium of bubbly liquid becomes essential for location and quantification of methane ebullition using active or passive techniques. This chapter details an investigation into the acoustic characteristics of water hosting bubbles which behave either as ideal or real gases. Tests were performed in a pressure vessel to simulate natural hydrostatic conditions.

3.1   Review of Literature

A century ago, Arnulph Mallock investigated the curious effect of bubbles damping the ring of a struck water-filled wine glass, concluding that even a small presence of gas can significantly affect the acoustic properties of a liquid [48]. In the decades to come it would be shown that just a few bub-

bles in a liquid can be a dominating factor in governing the acoustic velocity, attenuation, and scattering strength of such an effective medium [49–54]. A key publication by A.B. Wood presented a model of the acoustic velocity in a bubbly liquid mixture as a function of the relative volumes, the density, and the compressibility of the constituents of the mixture [55]. This model, now commonly referred to as "Wood's model" or "Wood's equation," gave a physical explanation of some of the interesting acoustic characteristics of bubbly liquids.

The acoustic contrast exhibited by a cloud of bubbly liquid relative to its surrounding non-bubbly liquid makes active acoustic techniques, such as echosounding or multibeam sonar, prime tools for the study of bubbles in bodies of water. In an attempt to use the scattering strength of bubble clouds to gain a better knowledge of bubble populations and their distributions, Medwin argued that "acoustic techniques have advantages over the tedious and difficult task of bubble-catching or photography" [56]. Specifically, he went on to state that acoustics can yield real-time information regarding the content of underwater bubble clouds with great measurement sensitivity. In another study, Vagle and Farmer found that acoustic methods avoid a common problem plaguing conventional optical means of detecting gas bubbles and estimating their sizes [57]. That is, in optical measurements, floating particles often pass through the frame and are inadvertently included in the gas measurement. Although an analogous inherent weakness exists in acoustic techniques, whereby organisms with swim bladders sometimes resemble gas bubbles, this source of

error is typically small relative to errors caused by waterborne particles being detected and counted optically. Interestingly, it is the simplicity of detecting sea life acoustically which has made possible a great deal of the methane ebullition research to date.

Due in part to the ubiquity of fish-finding echosounders, a number of studies have investigated the use of active acoustics as a tool for locating and quantifying methane ebullition in underwater environments [58–66]. Further, sounds *generated* by bubble plumes and clouds created by gas seeps and breaking waves, have been researched to better understand ocean mixing mechanisms, atmospheric weather conditions, and underwater noise sources [67–71]. However, the scope of these studies has been somewhat limited—the in situ tests have most often been capable of detecting the presence of gas bubbles in the water column, but incapable of determining gas volumes with adequate accuracy.

Kieffer took a theoretical approach to describe the speed of sound in liquid-gas mixtures as it relates to seismology [72]. It has been observed that seismic P-wave velocities may change as a result of gas production preceding geologic events such as earthquakes, volcanoes, and geysers [73]. To better predict such events, it is essential to understand the acoustic properties of the underground bubbly liquids of interest. However, when deriving models which should be accurate under the high pressures found deep in the Earth's crust, Kieffer assumed the gas contained in the fluid behaves as an ideal gas. It is known, however, that at pressure, we cannot expect the ideal gas law to be

valid [74]. In particular, as methane gas under ocean pressure is of interest in the current study, we must assume it behaves as a real gas [75–77]. To the knowledge of the author, the work presented here is the first to investigate the use of real gases with Wood's model. Results of this experiment were presented by Greene and Wilson in 2009, but are described in detail for the first time in the present chapter of this thesis [78].

3.2 Development of Models

The experiment and analysis described in this chapter warrants a detailed look into five relevant models: Wood's model of low-frequency sound propagation in a bubbly liquid, Commander and Prosperetti's model of frequency-dependent propagation through bubbly liquids, Van der Waals' equation of state, a one-dimensional acoustic waveguide resonator model, and Lafleur and Shields' model of an elastic waveguide. This section develops and explains these five models for practical use in performing high-pressure sound speed measurements on bubbly liquids.

3.2.1 Wood's Model

Consider a liquid which hosts a population of gas bubbles. Let us assume that the gas bubbles are spherical and uniformly distributed throughout the liquid. We can approximate the mixture as a homogeneous solution if we assume that the bubbles are sized and populated such that several bubbles lie within each acoustic wavelength. When insonified, the bubbly liquid

experiences small fluctuations in pressure amplitude and we assume that the excitation frequency, f, is low enough to keep the system within the long-wavelength limit. We also assume that the bubble centers are approximately stationary over the f^{-1} timescale, a valid approximation for naturally-rising bubbles in the frequency range of interest [79]. A convenient nomenclature to describe the relative gas content of the mixture is given by the void fraction, β_g, which we define as

$$\beta_g = \frac{V_g}{V_m}, \tag{3.1}$$

where V_g and V_m are the volume of gas in the mixture, and the total volume of the mixture, respectively. Letting $V_m = V_g + V_l$, where V_l is the volume of liquid in the mixture, we get

$$\beta_g = \frac{V_g}{V_g + V_l}. \tag{3.2}$$

Using these expressions, we can determine the density of our mixture, ρ_m, to be

$$\rho_m = \beta_g \rho_g + (1 - \beta_g)\rho_l, \tag{3.3}$$

where ρ_g and ρ_l are the densities of the gas and liquid, respectively. The effective compressibility, κ_m, of the bubbly mixture can be found as a linear combination of the compressibilities of its constituents relative to their volumes. Defining κ_g and κ_l as the compressibilities of the gas and liquid, respectively, we get

$$\kappa_m = \beta_g \kappa_g + (1 - \beta_g)\kappa_l. \tag{3.4}$$

35

Armed with expressions for the effective density and compressibility of our lumped medium, we can now find an expression for the low-frequency sound speed of the mixture. The sound speed of a fluid is given by

$$c = \sqrt{\frac{1}{\kappa\rho}}. \tag{3.5}$$

Substituting our expressions for the density and compressibility of the bubbly liquid, given by Eqs. 3.3 and 3.4, we obtain an expression for the sound speed of the effective medium of our mixture as a function of the material properties of the liquid and gas, and of the void fraction,

$$c_{\mathrm{m}} = [\kappa_{\mathrm{m}}\rho_{\mathrm{m}}]^{-\frac{1}{2}} = [(\beta_{\mathrm{g}}\kappa_{\mathrm{g}} + (1-\beta_{\mathrm{g}})\kappa_{\mathrm{l}})(\beta_{\mathrm{g}}\rho_{\mathrm{g}} + (1-\beta_{\mathrm{g}})\rho_{\mathrm{l}})]^{-\frac{1}{2}}. \tag{3.6}$$

This expression is equivalent to Wood's model for the low-frequency sound speed of a bubbly liquid [55]. It should be noted that the use of this expression assumes an excitation frequency well below the resonance frequency, given by Eq. 2.6, of any bubble in the mixture.

3.2.2   Sound Propagation Models

Wood's model has been proven accurate as a predictor of low-frequency phase speeds of bubbly liquids; however, some of the very assumptions which make it a simple, easy-to-use model, also limit its validity in many applications. For example, Wood's assumption that bubbles oscillate isothermally in essence neglects attenuation effects, which become highly relevant at frequencies near bubble resonance. Furthermore, the model does not account for higher-order effects such as internal acoustic scattering. A deeper investigation into the

acoustic behavior of bubbly liquids was performed by Commander and Prosperetti, who accounted for bubble dynamics and attenuation in their model of phase speed [80]. Using these methods, the complex sound speed of a bubbly mixture can be obtained as

$$c_{\mathrm{m}} = c_{\mathrm{l}} \left[1 + 4\pi c_{\mathrm{l}}^2 \int_0^\infty \frac{r_0 \wp(r_0)}{\omega_0^2 - \omega^2 + j2\zeta\omega} dr_0 \right]^{-\frac{1}{2}}, \qquad (3.7)$$

where c_{l} is the sound speed of the liquid, $\wp(r_0)$ is the number of bubbles of equilibrium radius from r_0 to $r_0 + dr_0$ per unit volume, and ζ is a damping coefficient given by

$$\zeta = \frac{2\sigma}{\rho_{\mathrm{l}} r_0^2} + \frac{P_\infty + 2\mu_{\mathrm{l}}/r_0}{2\rho_{\mathrm{l}} r_0^2 \omega} \Im(\Phi) + \frac{\omega^2 r_0}{2c_{\mathrm{l}}}. \qquad (3.8)$$

Here, μ_{l} is the viscosity of the liquid and the argument Φ is given in Eq. 2.3. If we assume the bubble size distribution is very narrow we can evaluate the integral in Eq. 3.7 letting the distribution be the delta function of N_{b} bubbles per unit volume,

$$\wp(r_0) = N_{\mathrm{b}} \delta(r_0 - \bar{r}_0), \qquad (3.9)$$

where $\bar{r}_0$ is the mean bubble radius in the distribution. Commander and Prosperetti's expression for phase speed then becomes

$$c_{\mathrm{m}} = \left[\frac{1}{c_{\mathrm{l}}^2} + \frac{4\pi r_0 N_{\mathrm{b}}}{\omega_0^2 - \omega^2 + j2\zeta\omega} \right]^{-\frac{1}{2}}. \qquad (3.10)$$

In Fig. 3.1, this expression is plotted as a function of frequency using arbitrary values for material properties and bubble radius. Here we see that the frequency-independent value of phase speed obtained with Wood's model is evident in the low-frequency regime below resonance.

37
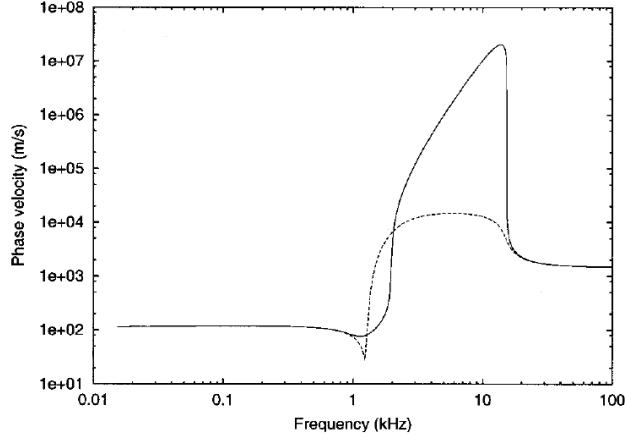
Figure 3.1: Models of phase velocity of a bubbly liquid. The dashed line represents Commander and Prosperetti's model, given by Eq. 3.10; the solid line shows Kargl's model, given by Eq. 3.11. Wood's regime is evident in the flat part of the curve below resonance. Graphic reprinted from Ref. [81].

Recently, Commander and Prosperetti's model has been modified to account for higher orders of multiple scattering. Kargl presented

$$
c_{\mathrm{m}} \approx \left[\frac{1}{c_1^2} + \frac{4\pi \bar{r}_0 N_{\mathrm{b}}}{\omega_0^2 - \omega^2 + j \left(\dfrac{4\mu_{\mathrm{l}}\omega + P_\infty \Im(\Phi)}{\rho_{\mathrm{l}} r_0^2} + \dfrac{\omega^3 r_0}{c_{\mathrm{m}}} \right)} \right]^{-\frac{1}{2}}
\tag{3.11}
$$

as a more accurate physical model [81]. By inspection, we see that phase speeds predicted by Eq. 3.11 will differ significantly from those predicted by Commander and Prosperetti's model in the frequency range near and just above resonance. Using Kargl's model, no sharp dip in phase speed is observed at resonance, yet we see a dramatic increase in phase speed at frequencies just above ω_0. Well below and well above resonance, however, Kargl's phase speed predictions are in close agreement with Commander and Prosperetti's. Unfor-

38

tunately, the recursive nature of Kargl's relation requires numerical methods to obtain the phase speed of a bubbly mixture. In the present work, however, excitation frequencies are well below ω_0, and thus, scattering can be neglected and Wood's model, given by Eq. 3.6, will be used to calculate phase speeds.

3.2.3 Equations of State

Although the form of Wood's equation presented in Eq. 3.6 does not explicitly limit its application to bubbly liquids containing ideal gases, the model has historically been applied with this assumption in mind. Given that our interest is in bubbly liquids containing methane at hydrostatic pressures exceeding 25 atmospheres, we must have an understanding of the thermodynamic properties of the gas under these conditions. The Nobel Prize-winning work by van der Waals, which accounted for intermolecular attraction in describing the behavior of non-ideal, or *real* gases, is a convenient starting point for the development of the model we will use in describing the properties of methane at pressure [82]. Let us begin with the ideal gas law,

$$\rho_{\mathrm{g}} = \frac{PM}{RT}, \tag{3.12}$$

where P is pressure, M is molecular mass, R is the universal gas constant, and T is temperature in units kelvin [83]. This expression describes a gas which behaves as a spring following Hooke's law, whose density is linearly related to the force exerted upon it. The current work involves gases which do not necessarily exhibit this behavior, so for convenience we define the compressibility factor, Z, as a measure of a gas' deviation from Eq. 3.12. Let Z equal the

39

density predicted by the ideal gas law divided the actual density of the gas,

$$Z = \frac{PM/(RT)}{\rho_\mathrm{g}}. \tag{3.13}$$

In the present experiment, the test gas is known and temperature and pressure can be measured easily. However, we will exploit the compressibility factor as a means of determining density, so we rearrange Eq. 3.13 to get

$$\rho_\mathrm{g} = \frac{PM}{ZRT}. \tag{3.14}$$

Van der Waals noted that on the molecular level, there is a certain unavailable volume, a "sphere of exclusion," around the molecules of real gases, where motion cannot occur. Taking this into account, he developed what would be deemed the van der Waals equation of state, given by

$$\left(P + \frac{a}{(M/\rho_\mathrm{g})^2}\right)\left(\frac{M}{\rho_\mathrm{g}} - b\right) = RT, \tag{3.15}$$

where a and b are constants corresponding to the gas of interest [84]. These constants may be found experimentally, or they may be approximated by considering the critical point, where temperature, pressure, and density are taken as their critical values, T_c, P_c, and $\rho_\mathrm{g,c}$, respectively [85]. At the point of inflection of the critical isotherm,

$$\left(\frac{\partial P}{\partial(M/\rho_\mathrm{g})}\right)_{T_\mathrm{c}} = \frac{-RT_\mathrm{c}}{(M/\rho_\mathrm{g,c} - b)^2} + \frac{2a}{(M/\rho_\mathrm{g,c})^3} = 0 \tag{3.16}$$

and

$$\left(\frac{\partial^2 P}{\partial(M/\rho_\mathrm{g})^2}\right)_{T_\mathrm{c}} = \frac{2RT_\mathrm{c}}{(M/\rho_\mathrm{g,c} - b)^3} + \frac{6a}{(M/\rho_\mathrm{g,c})^4} = 0. \tag{3.17}$$

40

Setting temperature, pressure, and density equal to their critical values in Eq. 3.15, we have

$$\left(P_c + \frac{a}{(M/\rho_{g,c})^2}\right)\left(\frac{M}{\rho_{g,c}} - b\right) = RT_c. \tag{3.18}$$

Solving Eq. 3.18 simultaneously with Eqs. 3.16 and 3.17, we find that

$$a = \frac{27R^2T_c^2}{64P_c} \quad \text{and} \quad b = \frac{RT_c}{8P_c}. \tag{3.19}$$

Rearranging Eq. 3.14, we have

$$\frac{M}{\rho_g} = \frac{ZRT}{P}, \tag{3.20}$$

which, along with constants a and b from Eq. 3.19, can be substituted into Eq. 3.18 to yield

$$\left(Z + \frac{27PT_c^2}{64ZP_cT^2}\right)\left(1 - \frac{PT_c}{8ZP_cT}\right) = 1. \tag{3.21}$$

This equation may be generalized by defining

$$P_r = \frac{P}{P_c} \quad \text{and} \quad T_r = \frac{T}{T_c} \tag{3.22}$$

as the reduced pressure and reduced temperature, respectively. A final substitution of these expressions into Eq. 3.21 gives the relation we will use to determine the compressibility factor,

$$\left(Z + \frac{27P_r}{64ZT_r^2}\right)\left(1 - \frac{P_r}{8ZT_r}\right) = 1. \tag{3.23}$$

Now, for a given gas of critical constants P_c and T_c, at temperature T and hydrostatic pressure P, the compressibility factor Z can be determined

41
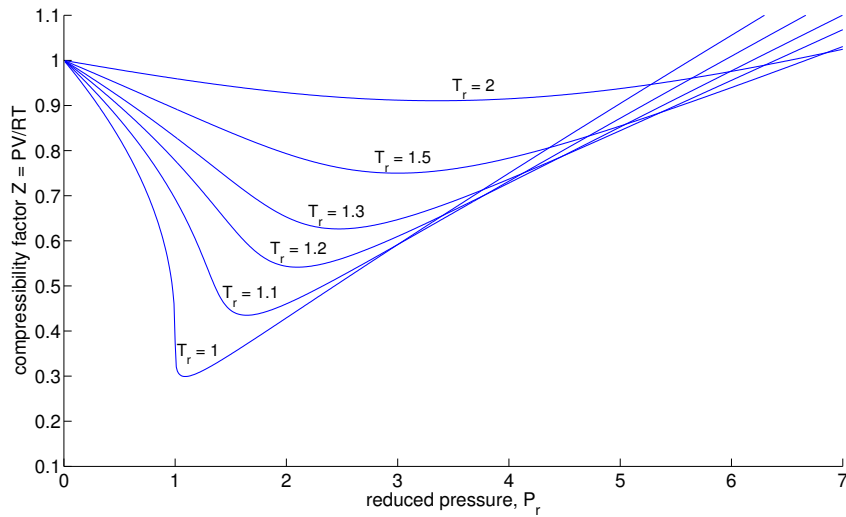
Figure 3.2: Generalized compressibility factors obtained numerically by Eq. 3.23.

numerically using Eq. 3.23, as presented in Appendix D.3. Predicted values of the generalized compressibility factor are shown in Fig. 3.2 as a function reduced pressure along example isotherms. The Matlab code developed to create this plot is provided in Appendix D.4.

To make practical use of the compressibility factor, we compute its value, Z_0, at atmospheric pressure, P_0, and temperature, T_0, where the density of the gas, $\rho_{g,0}$, is well established. Dividing Eq. 3.14 by ρ_g sets the right-hand side of the expression equal to unity, allowing us to equate it to the same expression letting the variables be their values which have been established for standard temperature and pressure conditions,

$$\frac{PM}{\rho_g Z R T} = \frac{P_0 M}{\rho_{g,0} Z_0 R T_0}. \tag{3.24}$$

42

Assuming the gas remains at standard temperature during the experiment, Eq. 3.24 may be rearranged to obtain a practical expression for density,

$$\rho_g = \frac{P}{P_0}\frac{Z_0}{Z}\rho_{g,0}.$$

(3.25)

When determining the compressibility, κ_g, of a real gas, such as in Eq. 3.6, Z must be considered. Compressibility of a gas is defined by

$$\kappa_g = \frac{\left(\frac{\text{increase in density}}{\text{original density}}\right)}{\text{increase in pressure}} = \frac{\frac{-\partial\rho_g}{\rho_g}}{\partial P} = -\frac{1}{\rho_g}\frac{\partial\rho_g}{\partial P},$$

(3.26)

or, the inverse of bulk modulus [86]. In the above relation, we recognize the inverse square of the definition of sound speed,

$$c = \sqrt{\frac{\partial P}{\partial\rho}},$$

(3.27)

which can be substituted into Eq. 3.26 for a more convenient form [87, 88]. Now we have

$$\kappa_g = -\frac{1}{\rho_g c^2}.$$

(3.28)

Combining Eqs. 3.14, 3.27, and 2.2, we can obtain an expression for the speed of sound in a real gas,

$$c_g = \sqrt{\frac{Z\gamma P}{\rho_g}}.$$

(3.29)

For the present case, where the acoustic velocity, $c_{g,0}$, of the gas is known for standard conditions, it becomes useful to substitute this relation into Eq. 3.28 to obtain a form of the expression for gas compressibility which can easily be used in laboratory applications,

$$\kappa_g = -\frac{1}{Z\rho_g c_{g,0}^2}.$$

(3.30)

43

Now, Eq. 3.25 and Eq. 3.30 may be used in Eq. 3.6 as a practical model of sound speed in bubbly liquids containing real gases. In the analysis of the present experiment, the value of $c_{\text{g},0}$ for air was determined by

$$c_{\text{g},0} = \sqrt{\frac{\nu P_0}{\rho_{\text{g},0}}}, \qquad (3.31)$$

where $\rho_{\text{g},0}$ is the STP density of the gas. The value of the polytropic index depends upon bubble size and excitation frequency, and thus, will be unique for each bubble in the mixture; however, to the degree of accuracy appropriate for this work, the polytropic index is taken as a constant $\nu = 1.18$, as given by Wilson in Ref. [89]. Gas properties used in this work are provided in Table B.1 in the Appendix.

3.2.4   1D Acoustic Resonator

A useful tool for measuring the acoustic velocity of a fluid employs a 1D cylindrical acoustic waveguide as a resonator. This section outlines two models which can be used to calculate sound speeds using such a device.

3.2.4.1   Modal Sound Speeds

Consider a fluid-filled, rigid-walled tube with boundary conditions such that acoustic pressure is approximately zero at its ends. If the fluid in the tube is excited longitudinally, fundamental resonance frequencies, f_n, can be found to have integer-multiples of half-wavelengths corresponding to the length of

the tube. Kinsler et al. predict resonances as

$$f_n = \frac{n}{2L} c_n \quad n = 1, 2, 3, ... \tag{3.32}$$

where n indicates the mode number and L is the length of the tube resonator [90]. Rearranging, we can obtain an expression for the sound speed of the fluid sample at each resonance frequency,

$$c_n = \frac{2L}{n} f_n. \tag{3.33}$$

Using a signal analyzer to perform a transfer function between an acoustic source and receiver placed in the sample fluid, as described by Wilson and Dunton, it is possible to obtain a spectrum of resonances in the frequency range over which the system is excited [91]. An example spectrum is shown in Fig. 3.3a. With this plot, resonance frequencies can easily be determined by inspection and sound speeds can be calculated for each mode using Eq. 3.33.

3.2.4.2 Slope Method of Calculating Sound Speed

In developing Eq. 3.33, the assumption has been made that acoustic pressure is approximately zero at both ends of the tube resonator. This assumption is most often valid due to the high contrast in acoustic impedance at the air-liquid interfaces at each end of the model tube [92]. However, in this work, the tube is oriented vertically, with an air-liquid interface its top, and what will prove to act as a rigid interface at its lower terminus. Thus, we seek a more general expression for $c(f_n)$ which allows for either of the possible boundary conditions. If we assume the sound speed of the sample is constant

45
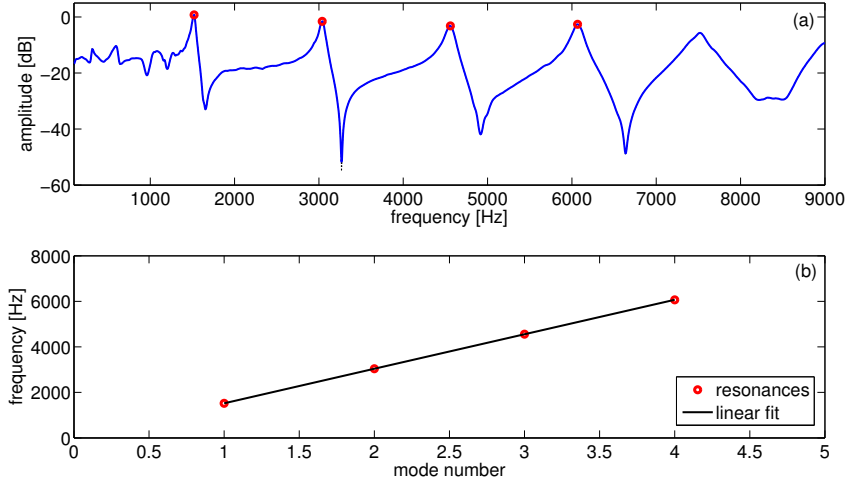
Figure 3.3: (a) Example resonance spectrum and (b) resonance frequencies plotted as a function of mode number, with a line fitted to data points for calculation of sound speed using Eq. 3.34.

over the frequency range of interest, we may then use an expression for the frequency-independent sound speed,

$$c = 2L\frac{\Delta f}{\Delta n}, \tag{3.34}$$

where $\frac{\Delta f}{\Delta n}$ is the slope of the linear fit of resonance frequencies plotted as a function of their corresponding mode numbers, as shown in Fig. 3.3b [93].

Interestingly, in the current study, an independent, powered sound source will prove to be unnecessary. Instead, as Nicholas et al. found, the "birthing wails" produced by bubbles will be sufficient to excite the normal modes of the water column [70]. With this method, $N = 50$ recordings of the hydrophone signal are transformed to the frequency domain and averaged with
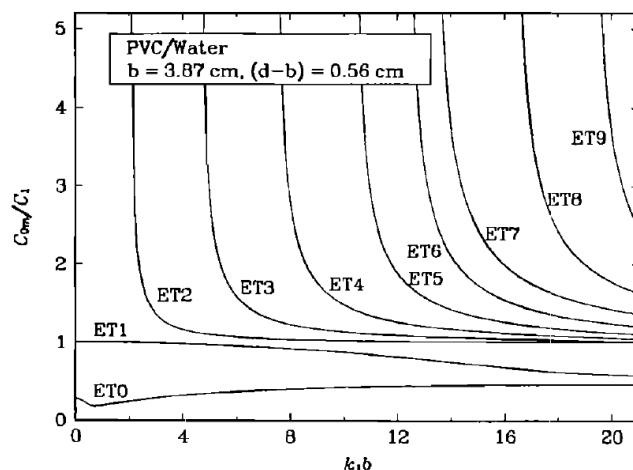
Figure 3.4: Example dispersion curve for sound propagation of water through a PVC waveguide, reprinted from Lafleur and Shields [96]. Vertical axis shows phase speed relative to its freefield value and horizontal axis is a nondimensional frequency obtained by multiplying wavenumber k_1 by inner diameter of the tube, which the authors define as b.

the vector signal analyzer using root-mean-square averaging. The averaging process reduces noise in the FFT plot and clarifies resonances as distinct peaks in the spectrum.

3.2.5 Elastic Waveguide Effect

When a cylindrical tube is used as a resonating waveguide, the compliance of the tube walls must be considered. It is known that when a fluid is confined in a tube made of a real material, sound propagating through the fluid will be dispersive and slower than the freefield acoustic velocity of the fluid [55, 94, 95]. A clear and somewhat extreme example of this is shown in Fig. 3.4, where we see that in a water sample, the "ET0" mode of interest

47

propagates through a PVC waveguide at as little as 20% of its freefield acoustic velocity. This elastic waveguide effect has been quantitatively described by Del Grosso, who built on the work of Lin and Morgan to develop a model of axisymmetric sound propagation through a cylindrical tube [97–99]. Lafleur and Shields later modified Del Grosso's notation to make it more user-friendly, evaluated several cases of the model, and verified its accuracy by comparing predictions with experimental results [96]. Despite the simplifications made by Lafleur and Shields, their derivation remains rather involved and the generalized system of equations required to produce dispersion curves is lengthy and complex. For brevity, a derivation of this model is not presented here; however, a Matlab script developed to calculate the elastic effect of a given waveguide is provided in Appendix D.5.

Del Grosso showed that the speed of sound propagating through a fluid in a tube will be reduced relative to the freefield acoustic velocity of the fluid, and the magnitude of this reduction is highly dependent on the contrast in acoustic properties between the fluid and the tube. As an example, for the case of water in a PVC tube, where material densities and acoustic velocities are relatively close, the sound speed measured in the confined water will be far below the freefield acoustic velocity of the water. In the present work, it was determined that the range of void fractions used in the experiment yielded very low fluid sound speeds. The low sound speed and high compliance of the bubbly liquids, combined with the dense, rigid nature of the borosilicate tube gave sufficient contrast in acoustic properties between the two materials,

allowing the elastic waveguide effect to be neglected in the analysis of the present data.

3.3   Experimental Design

In this work, a borosilicate tube was oriented vertically and its lower end was fitted with a bubble injection manifold, consisting of 12 vertical 22-gauge needles embedded in an epoxy-filled PVC fitting. The tube measured 454 mm in length, with an inner diameter of $d_i = 54$ mm and an outer diameter of $d_o = 64$ mm. The resonator was filled with distilled water. A cylinder of test gas (medical-grade air or sulfur hexafluoride) was connected to the bubble injection manifold with a two-stage pressure regulator and volume flowmeter in line. A Brüel & Kjær 8103 hydrophone, with its cable encased in a stainless steel sheath, was placed in the water column and the signal from the transducer was amplified with a voltage preamp before being captured by a Hewlett Packard 89410A vector signal analyzer (VSA). The resonator was placed in a cylindrical 316 stainless steel pressure vessel of inner diameter 14.6 cm and length 105 cm. The chamber was pressurized using medical-grade breathing air and pressure was monitored throughout the duration of the experiment. The water column height, h, was monitored using a 600-line low-lux grayscale video camera, whose power source also supplied energy to an LED lighting system. A complete schematic of the experimental setup is shown in Fig. 3.5.

In Wood's model (Eq. 3.6), we see that especially for low void fractions, sound speed is a strong function of β_g. In this experiment, void fraction was
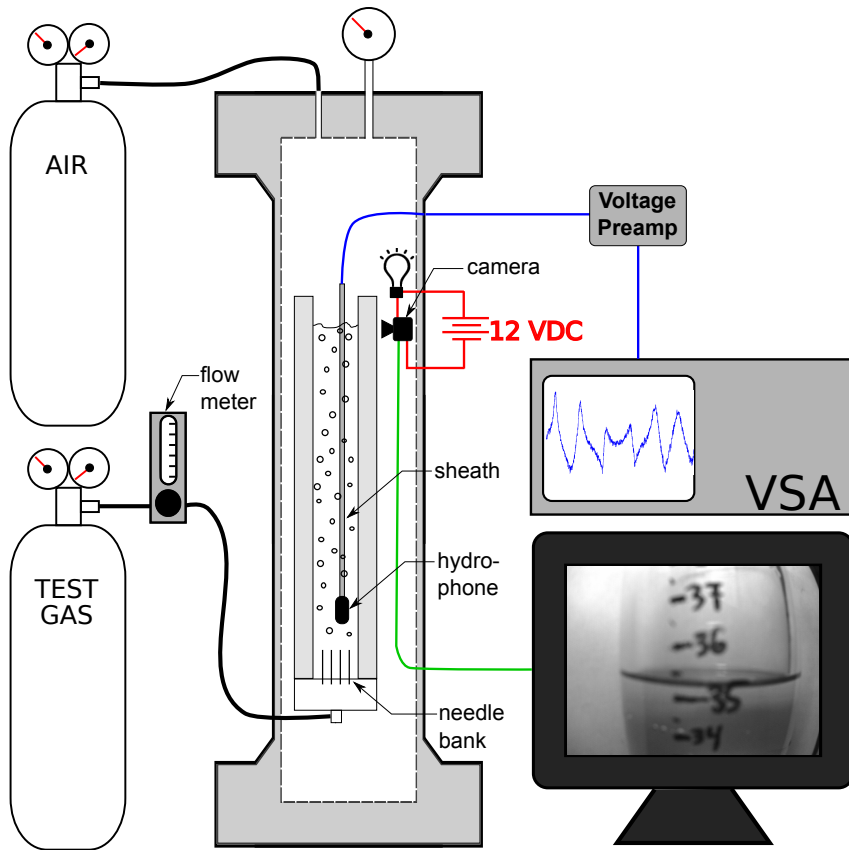
Figure 3.5: Schematic of pressurized bubbly liquids experiment.

measured to a high degree of accuracy using a video monitor, which showed the top few centimeters of the borosilicate resonator from the side. The resonator was marked in millimeter increments, with zero defined at the level of the needle tips and marks ascending upward along the length of the tube. A measure corresponding to the volume of liquid in the tube could be obtained by stopping the flow of test gas into the resonator and recording the height of the water column, h_0. Then, allowing the test gas to flow into the resonator

and letting the system to reach a steady state, a measure corresponding to the total volume of bubbly liquid in the resonator could be obtained by recording the height, h_1 of the column. From Eq. 3.2 we see that void fraction can be taken as

$$\beta_{\mathrm{g}} = \frac{h_1 - h_0}{h_1}. \tag{3.35}$$

For the experiment, a void fraction was chosen and delivery pressure of the test gas was regulated to maintain that void fraction. An acoustic spectrum was recorded at incrementing hydrostatic pressures, which were attained by venting or adding medical-grade air to the pressurized chamber. Spectra were measured and recorded over a range of hydrostatic pressures, then the process was repeated for other void fractions and other test gases. Thus, spectra were recorded to measure sound speeds while varying each of the three independent variables—hydrostatic pressure, void fraction, and test gas—individually, while holding the other two constant.

For each spectrum, sound speed was calculated using the slope method described in Sec. 3.2.4.2, taking only the two lowest-frequency resonance peaks. At high hydrostatic pressures, several resonance peaks were distinct and a linear fit of their frequencies versus mode number showed a low coefficient of determination. However, at low hydrostatic pressures, higher-mode resonances faded and became indistinguishable. Thus, for consistency, only the lowest two resonance frequencies were used for all spectra.
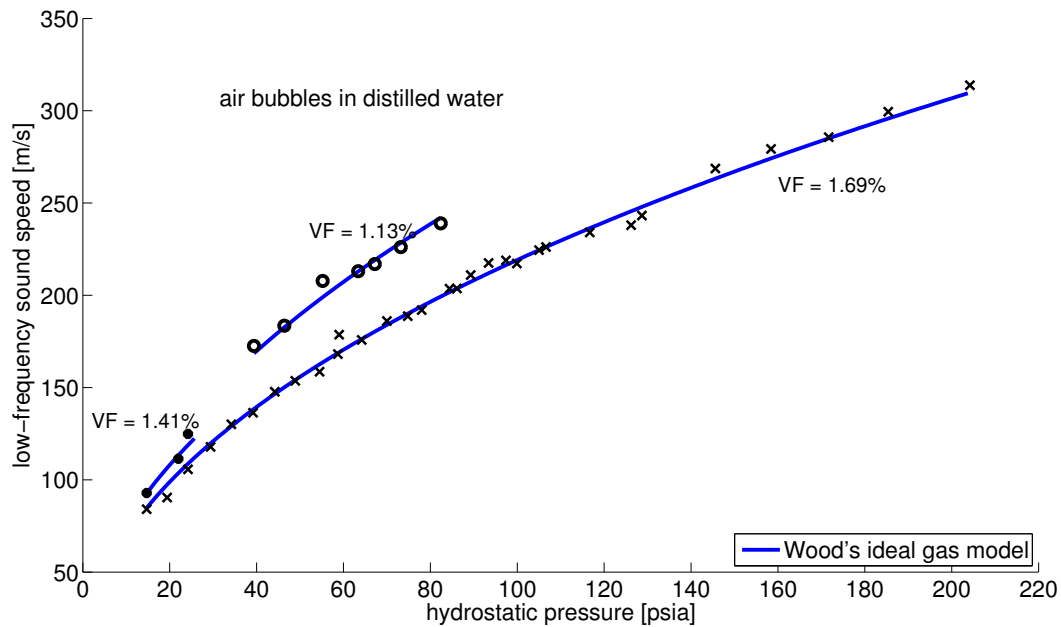
Figure 3.6: Results of pressurized air bubbles in water with Wood's prediction for a bubbly liquid containing ideal gas plotted in blue. "VF" represents void fraction.

3.4   Results

Figure 3.6 shows all data points measured for three void fractions of air bubbles in water, over a range of pressures from 1 atm to 14 atm. Sound speeds predicted by Wood's model for a bubbly liquid containing ideal gas (Eq. 3.6 with Eq. 3.25 and Eq. 3.30 letting $Z = 1$) are plotted, showing notable agreement between the model and experimental results.

Perhaps a more interesting set of results are those obtained for sulfur hexafluoride bubbles in distilled water over the pressure range of 1 atm to 9 atm. Shown in Fig. 3.7, we see that Wood's model of a bubbly liquid
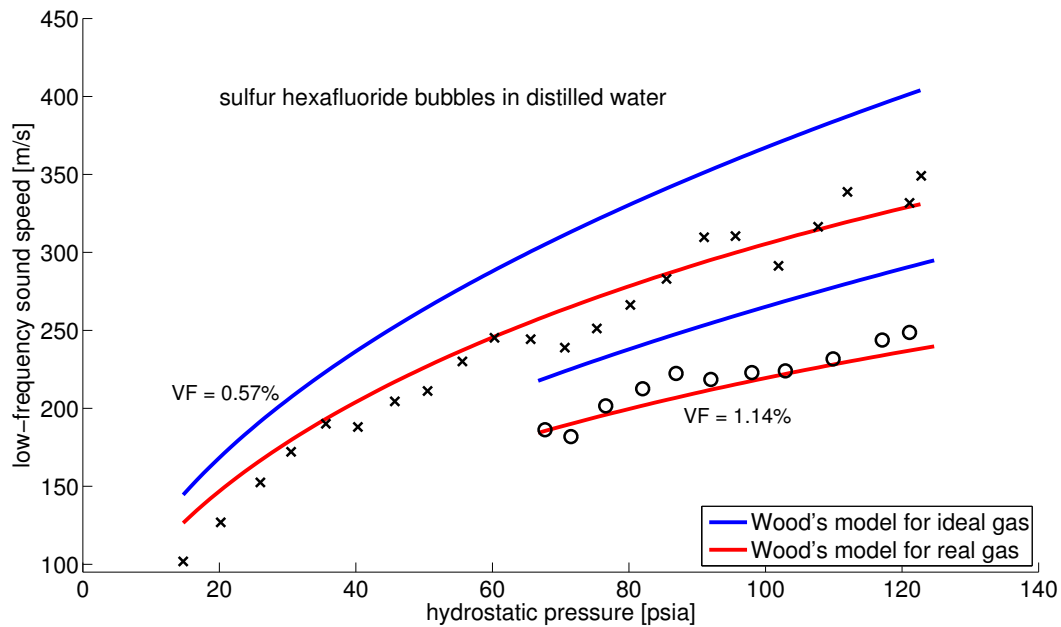
Figure 3.7: Results of pressurized sulfur hexafluoride bubbles in water with Wood's prediction for a bubbly liquid containing ideal gas plotted in blue and predictions obtained assuming a real gas plotted in red. "VF" represents void fraction. Sulfur hexafluoride properties used in the calculation of the red curve were taken from Ref. [100].

containing ideal gas does not accurately predict the phase speeds of the mixture, even at atmospheric pressure. However, if we use a model which assumes real gas behavior, where values of Z are calculated using the code provided in Appendix D.3, predictions are much more accurate.

3.5 Discussion of Bubbly Liquids Experiment

If we consider the compressibility factor of the test gas, it is not surprising that in our experiments, the acoustic velocity of bubbly liquids containing
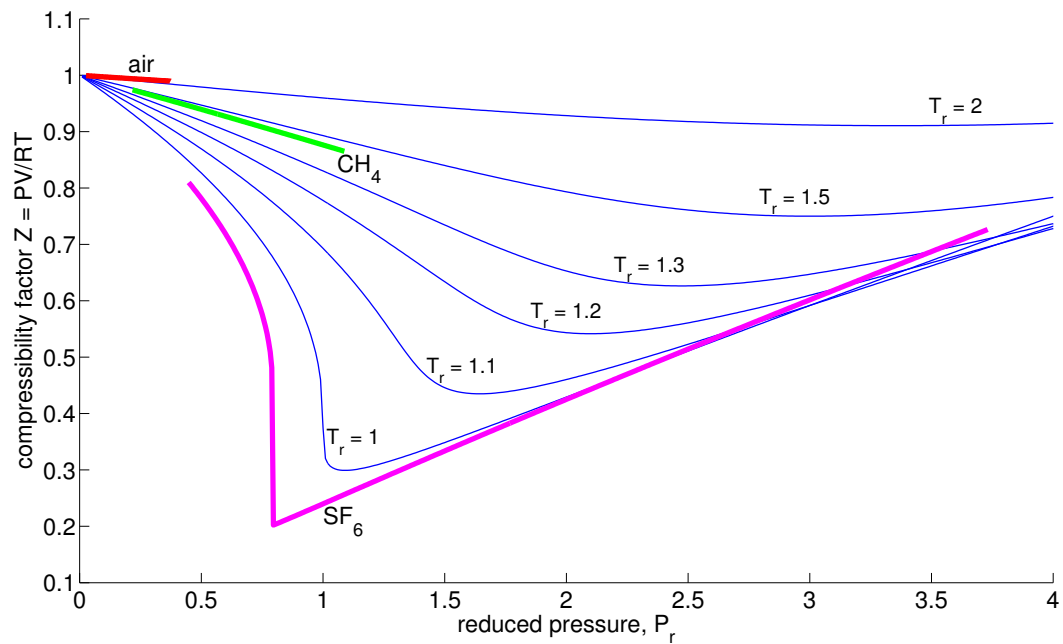
Figure 3.8: Generalized compressibility chart showing values for air (red) and sulfur hexafluoride (fuchsia) corresponding to the pressure ranges used for the gases. Shown in green is the compressibility factor of methane at pressures equivalent to water depths of interest.

air bubbles can be accurately predicted up to 14 atm using the traditional form of Wood's model which assumes ideal gas behavior. It is also not surprising that sulfur hexafluoride, even at atmospheric pressure, cannot be approximated as a real gas. Figure 3.8 shows compressibility factors, calculated using van der Waals equation of state, of air and sulfur hexafluoride, corresponding to the pressure ranges used for each gas in the experiment. Here, we see that for air, $0.99 \leq Z \leq 1.00$ from atmospheric pressure up to 14 atm. A common rule of thumb recommends that if the compressibility factor is within one per-

cent of unity, a gas may be assumed to behave ideally, and indeed, we did observe ideal gas behavior for the bubbly liquid containing air, over the entire range of pressures used in the experiment. Conversely, sulfur hexafluoride did not behave as an ideal gas, even at atmospheric pressure, and we see that its compressibility factor did not exceed 0.82 at any point in the test. Thus, real gas behavior was observed as expected.

Bubbly liquids containing methane gas have motivated this research, however, this study did not employ methane as the test gas due to safety requirements which could not easily be met. Although the author did not perform measurements on liquids containing methane bubbles, the argument posed is that armed with a knowledge of a gas' compressibility factor, which can be determined for any given gas in known pressure and temperature conditions, the sound speed of the bubbly liquid can be predicted accurately. This has been proven for air bubbles, which behave as an ideal gas; it has been proven for sulfur hexafluoride bubbles, which behave very much as a real gas; and the theory supports the claim that the model will accurately predict sound speeds of bubbly mixtures containing methane, whose compressibility factor at water depths of interest lies between that of the air and sulfur hexafluoride tested in this experiment.

Chapter 4

Low-Frequency Acoustics of Methane Hydrates in a Pressure Chamber

Natural gas hydrates are most often formed and found in ocean sediments; however, the compounds have been seen in a variety of media, including, in rare cases, as populations of marble-sized solids suspended in the water column, hundreds of meters above the sediment [64]. It is important to gain an understanding of the acoustic behavior of hydrates in the many media in which they are found naturally. Of particular import is low-frequency acoustic behavior of hydrates, which has yet to see extensive investigation. As a step toward understanding the behavior of hydrates in complex media, such as in water-saturated sediments, this chapter will focus on the low-frequency acoustic behavior of structure I and structure II methane hydrates in liquids and in bubbly liquids.

4.1 Definition of Methane Hydrates

Gas hydrates, often referred to as *clathrate hydrates*, *gas clathrates*, or simply, *hydrates*, are crystalline molecular host structures which entrap guest molecules without chemical bonds. This ice-like substance forms in
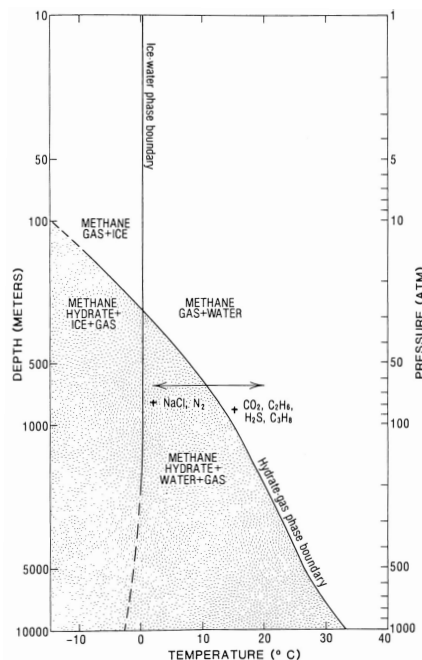
Figure 4.1: Example methane hydrate phase diagram. The vertical axis shows ocean depth on the left with equivalent pressure shown to the right, increasing downward, and the horizontal axis is temperature. Here, it is evident that methane hydrates are stable in high-pressure, low-temperature conditions. Graphic reprinted from Ref. [101].

high-pressure, low-temperature environments, and requires such conditions to remain stable, as shown in Fig. 4.1. The multiple names for the compound are often used interchangeably; however, each term describes specific traits of the structure. Powell defined *clathrate*, from the Latin, *clathratus*, meaning, "to encage," as a general term for any such cage-like molecular structure [102]. A *clathrate hydrate* is then a compound in which water forms the rigid lattice, and *gas clathrate hydrate* specifies that the guest molecule in the structure is a gas. In this thesis, the term *clathrate* will be dropped and the compounds

57

will be referred to as *hydrates*, *gas hydrates*, or *methane hydrates*, dependent upon the appropriate level of generality or specificity.

Three molecular structures of gas hydrates are known to exist. Structure I is a body-centered-cubic orientation which forms naturally in deep oceans from biogenic gases. It is worth noting that this molecular geometry can trap great quantities of gas in a small volume, concentrating methane by a factor of 164 relative to its volume at STP [103]. Structure II is a diamond lattice within a cubic framework, formed from thermogenic gases, often in oil-rich areas [9]. Structure H is a rare hexagonal form, which has only recently been shown to exist in nature [104]. A schematic overview of the unit crystals of each structure is provided for reference in the Appendix, Fig. A.4. The focus of this work is on structure I and structure II hydrates hosting molecules of methane gas.

4.2 Review of Literature

The discovery of gas hydrates is most often attributed to Sir Humphrey Davy for his 1810 laboratory experiments on compounds containing chlorine and water at near-freezing temperatures [105]. However, it is possible that Joseph Priestley's poorly-documented experiment on sulfur dioxide and water may have resulted in the formation of a gas hydrate more than thirty years prior [106]. For more than a century, hydrates were considered a mere laboratory curiosity, but in recent years, interest in the compounds has been piqued among the scientific community. Due to their high energy content and global

abundance, hydrates are now commonly discussed as a potential fuel source, and due to methane's potency as a greenhouse gas, climate researchers are eager to learn more about the mechanisms of their formation and the impacts of their dissociation [107–111]. Hydrates are also a concern in gas transmission and oil drilling operations, most recently gaining notoriety when the compounds foiled BP's attempt to stop the Deepwater Horizon oil spill by forming inside the "top hat" containment cap [112–115]. For these reasons, gas hydrates have become a relevant and hot topic among the scientific community. Researchers from a variety of fields wish to learn more about hydrates, but improved methods of locating the compounds are necessary to further their work. Thus, acousticians, geochemists, and geophysicists are seeking to develop techniques of finding, mapping, and estimating the sizes of the many hydrate deposits which are hidden away in the sediments below the Earth's oceans and lakes.

The use of active acoustic techniques for surveying water columns, mapping bottom profiles, and investigating features below the sediment surface is common within the methane hydrate research community. It has been observed that subsurface deposits of gas hydrates sometimes trap free dissociated gas below the hydrate layer, resulting in strong seismic reflections called *bottom-simulating reflectors*, or *BSR*s [116–119]. Despite the acoustically distinct nature of BSRs, a simple knowledge of their existence in a given location is insufficient to determine the quantity of hydrate in a deposit whose presence is detected. A better understanding of the link between compressional

acoustic velocities of gas hydrates and observed acoustic reflectivity may help improve quantitative detection of methane hydrate deposits [120].

In 2002, seeking new methods of hydrate detection which did not rely on the indirect and equivocal methods which plague conventional seismic techniques, Hornbach et al. used multichannel seismic reflection data to find direct indicators of methane hydrates in Blake Ridge [121]. Velocity profiles revealed an interesting feature—bright spots were seen within the gas hydrate stability zone (GHSZ), indicating "discrete layers of concentrated hydrate formed by upward migration of gas." Hornbach et al. analyzed these bright spots and despite impressive precision of their hydrate volume measurements, concluded that the measurement technique would benefit from a better understanding of the acoustic properties of the hydrate deposits.

One shortcoming of conventional practices may be contributing to our poor understanding of the acoustic behavior of gas hydrates: Despite the low-frequency nature of seismic sources and the prevalence of seismic techniques in locating hydrates, much of the literature relies upon established properties of methane hydrates which have been measured at frequencies exceeding 200 kHz. As an example to illustrate this discrepancy, Hornbach et al. searched for hydrates using generator-injector guns which had a dominant frequency of 0.15 kHz, while Weber et al. and Gunn and Best prescribe sediment core logging techniques which measure acoustic velocity using a 500 kHz transducer [122, 123]. It has been shown that gassy sediments have acoustic properties which are highly-dependent on frequency, and thus, further investigation

of the low-frequency acoustic behavior of methane hydrates is warranted for improved accuracy of acoustic and seismic surveys [124, 125].

Active acoustic surveys of methane-rich regions have uncovered an interesting phenomenon whereby methane bubbles in the GHSZ may form a "hydrate skin" along their gas-liquid interface as they rise [64, 126, 127]. As a result, the hydrate skin may retard bubble dissolution and enhance methane transport toward the surface and into the atmosphere [128]. For climate researchers who wish to acoustically locate three-phase media of waters containing methane gas bubbles and solid methane hydrates, an understanding of the low-frequency acoustic behavior of such a medium is essential. In Ch. 3 of the present thesis, a model was developed to describe the acoustic behavior of methane bubbles in liquid at pressures found naturally in the GHSZ. The experiment described in the present chapter was aimed at developing a better understanding of the low-frequency acoustic behavior of solid methane hydrates in simulated GHSZ pressures and temperatures.

4.3 Development of Models

Much of the physical bases which govern the present experiment on samples of methane hydrates in a brine-filled[1] resonator inside a pressure chamber parallel the models of gas bubbles in a water-filled resonator inside a pressure chamber, which were described in Ch. 3. Both experiments exploit

---

[1]In the present experiment, the resonator was filled with a high salinity ($S \approx 131‰$) brine to allow for a liquid state at temperatures below 0°C.

a cylindrical tube resonator with which sound speeds are calculated using the slope method detailed in Sec. 3.2.4.2, and corrections for the elastic waveguide effect, described in Sec. 3.2.5, are taken into account as necessary. The present analysis is focused on the two-phase case of solid hydrates in liquid, and thus, does not warrant the use of van der Waals' equation of state. For investigation of the three-phase case, where methane gas is included in the mixture, the compressibility factor of the gas must be considered, as any dissociation of methane hydrates in a pressure chamber inherently involves the release of non-ideal gas. To gain an understanding of the behavior of methane gas as it is released from the hydrates (analysis which is beyond the scope of the present work), see Sec. 3.2.3, which provides calculation methods for the compressibility factor of real gases. Wood's model, detailed in Sec. 3.2.1, plays a significant role in analysis of the current data; however, the form of the model previously presented requires some adaptation for the experiment on methane hydrates.

4.3.1 Wood's Model for a Two-Phase Mixture

In its most general form, $c_\mathrm{m} = [\kappa_\mathrm{m}\rho_\mathrm{m}]^{-\frac{1}{2}}$, Wood's model describes the phase speed of a mixture as a simple function of the mixture's density and compressibility. Therefore, we need not limit the model's use to liquids containing gas bubbles—the expression may also be applied to homogeneous mixtures of liquids containing "bubbles" of liquids, or even solids. Here, the term *homogeneous* may need clarification. To maintain the validity of Wood's model, a

mixture must appear homogeneous not by sight, but by sound. Surprisingly, the even distribution of just four to six samples in a half-wavelength resonator is sufficient to achieve acoustic homogeneity [129]. For such homogeneous mixtures containing samples of methane hydrate, a change of nomenclature is appropriate. When discussing mixtures of gas bubbles in liquid, it is intuitive to describe the volume occupied by the gas as a *void* fraction. However, as we apply Wood's model to a mixture of solid hydrate samples in liquid, it is more befitting to describe the *volume* fraction, β_h, of the hydrate in the mixture. An expression analogous to Eq. 3.2 can be found as

$$\beta_h = \frac{V_h}{V_h + V_l},$$

(4.1)

where V_h is the total volume occupied by the hydrate samples in the resonator. Continuing the analogue to the model developed in Sec. 3.2.1, we can obtain expressions for the respective density and compressibility of our liquid-hydrate mixture as

$$\rho_m = \beta_h \rho_h + (1 - \beta_h)\rho_l$$

(4.2)

and

$$\kappa_m = \beta_h \kappa_h + (1 - \beta_h)\kappa_l,$$

(4.3)

where ρ_h and κ_h are the density and compressibility of the hydrate, respectively. These expressions can now be substituted into Wood's model to obtain an expression for sound speed of the two-phase mixture,

$$c_m = [(\beta_h \kappa_h + (1 - \beta_h)\kappa_l)(\beta_h \rho_h + (1 - \beta_h)\rho_l)]^{-\frac{1}{2}}.$$

(4.4)

4.3.2 Wood's Model for a Three-Phase Mixture

We may extend Wood's two-phase mixture model to apply to a three-phase homogeneous mixture. Equation 4.4 is useful for mixtures containing methane hydrate samples in liquid; however, if temperature and pressure conditions are such that the hydrates undergo dissociation, methane gas is released and the mixture is then a three-phase mixture of liquid, solid, and gas. Given that the lumped three-phase mixture will have an effective density and compressibility, Wood's model is also valid for this case. From Eq. 3.1, we see that the volume fractions of gas and hydrate are given by the ratios of their respective volumes over total volume of the mixture,

$$\beta_g = \frac{V_g}{V_g + V_h + V_l} \quad \text{and} \quad \beta_h = \frac{V_h}{V_g + V_h + V_l}, \tag{4.5}$$

Density and compressibility are then found as

$$\rho_m = \beta_g \rho_g + \beta_h \rho_h + (1 - \beta_g - \beta_h)\rho_l \tag{4.6}$$

and

$$\kappa_m = \beta_g \kappa_g + \beta_h \kappa_h + (1 - \beta_g - \beta_h)\kappa_l. \tag{4.7}$$

The expressions given by Eqs. 4.6 and 4.7 may now be used in Wood's equation to obtain an expression for the sound speed of a three-phase mixture,

$$c_m = \sqrt{\frac{(\beta_g \kappa_g + \beta_h \kappa_h + (1 - \beta_g - \beta_h)\kappa_l)^{-1}}{\beta_g \rho_g + \beta_h \rho_h + (1 - \beta_g - \beta_h)\rho_l}}. \tag{4.8}$$

4.3.3 Hydrate Stability Models

In 1972, Parrish and Prausnitz (Ref. [130]) used experimental data to fit constants to a model based on the work of Van der Waals and Platteeuw [131]. Parrish and Prausnitz stated that their model should only apply to structure I methane hydrates, and the model was validated for a temperature range of 0°C to 27°C. Two decades later, Dickens and Quinby-Hunt developed an empirical equation based on data from their own experiments on methane hydrates in seawater of salinity $S = 33.5‰$ [132]. Sloan later gave a detailed explanation of the thermodynamic and kinetic properties of each of the three known structures of methane hydrates. In that paper he gives an expression for the temperature-dependent dissociation pressure of methane hydrate, but neglects to discuss how the relation was developed or even which hydrate structure it describes [9]. Soon after, Peltzer and Brewer fit the data presented in Sloan's paper to a simple second-order polynomial to build an expression which was modeled after Dickens and Quinby-Hunt's relation [133]. The models are provided for reference in Appendix C.

The four models discussed in this thesis take various forms, but they all describe an inverse relationship between the pressure and temperature of hydrate dissociation. Of these models, only the Parrish and Prausnitz model is structure-specific. Although a few of the aforementioned authors acknowledged that the dissociation temperature-pressure relation is affected when the hydrate is surrounded by seawater, only Dickens and Quinby-Hunt explicitly stated the salinity of the host liquid considered in the development of their

models.

4.4 Experimental Design

In this work, the experimental apparatus described in Sec. 3.3 was adapted to investigate the effects of hydrostatic pressure on the acoustic properties of brines containing samples of methane hydrates. For this, the test gas delivery system and needle bank which had been used in the bubbly liquids experiment was removed. A 459 mm long borosilicate resonator with an inner diameter of 52 mm and outer diameter of 70 mm was wrapped in coiled copper tubing through which chilled ethylene glycol at a temperature of -20°C circulated. Any exposed copper tubing was then covered with fiberglass insulation. The bottom of the resonator was sealed with a nitrile rubber membrane and the resonator rested atop a closed-cell foam block, creating an approximate pressure-release boundary condition at the lower terminus. An audio amplifier powered an electromagnetic shaker, to which an aluminum piston was attached. The piston was placed in the brine near the top of the resonator to excite the system while a Reson type 4013 hydrophone, with its cable encased in a water-filled stainless steel sheath, sensed the acoustic response of the system. The hydrophone signal was amplified and bandpass filtered with a Reson VP2000 voltage preamp. A Hewlett Packard 89410A vector signal analyzer recorded the average of 30 transfer functions for each measurement. The apparatus and procedures used in the present work closely mimics the experimental design described by Wilson et al. in Ref. [134]. A schematic of
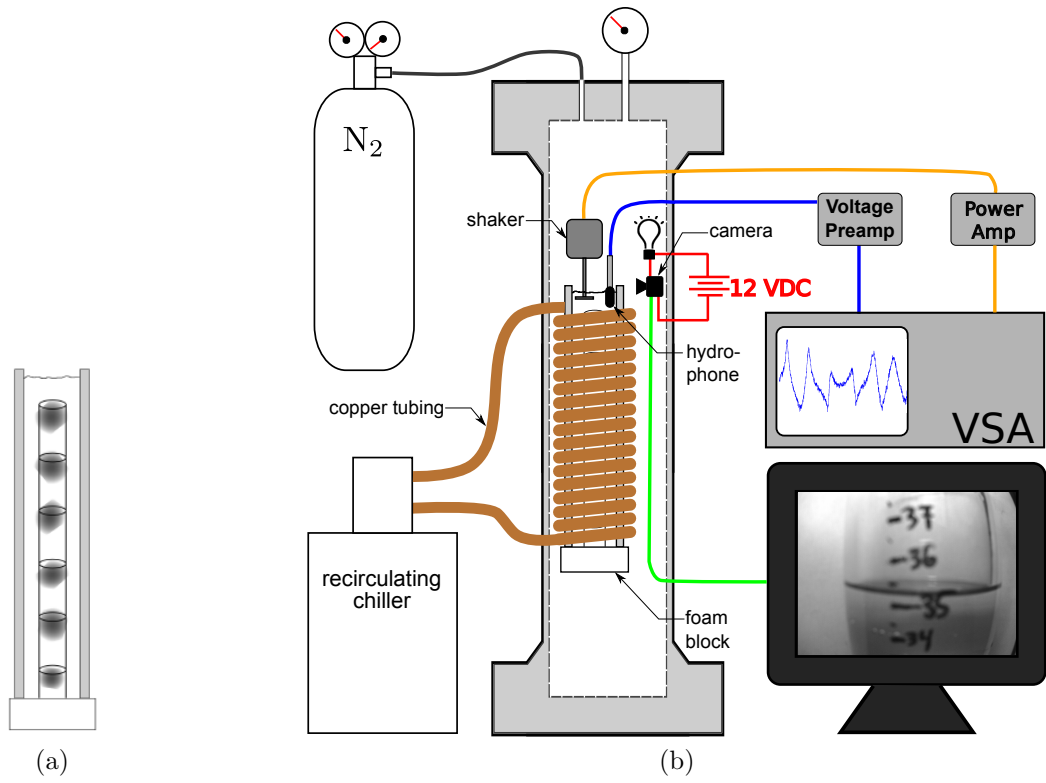
Figure 4.2: Methane hydrate resonator schematic showing (a) the borosilicate tube with pressure-release bottom and copper wire cage structure holding hydrate samples, and (b) the resonator in pressure vessel with chilling system.

the apparatus is given in Fig. 4.2.

A copper wire cage, shown in Fig. 4.2a, was constructed to suspend six approximately equally-spaced pieces of methane hydrate in the resonator. To prohibit the samples from escaping the wire cage and floating to the top of the brine, the cage was wrapped in copper wire mesh. To prevent bubbles from attaching to the copper cage, the cage was coated with a hydroxy-terminated polydimethylsiloxane solution and allowed to dry before it was placed in the

sample	structure	origin
CMsI	I	Cascadia Margin
CMsII	II	Cascadia Margin
HMsI	I	Håkon Mosby
GMsII	II	Gulf of Mexico

Table 4.1: Structures and origins of methane hydrate samples. Samples were provided by the United States Naval Research Laboratory.

resonator.

Natural samples of methane hydrates were provided by the United States Naval Research Laboratory. The samples were collected through coring operations in 1998 and stored in liquid nitrogen at atmospheric pressure until January 2010. At that time, the hydrates were packed in a dewar with liquid nitrogen and shipped from the storage facility in Washington D.C. to Applied Research Laboratories in Austin, Texas. Geographical origins and molecular structures of the samples are listed in Table 4.1.

For each test, a hydrate sample was broken into six pieces, approximately 2 cm in diameter, which were placed in the copper cage. The cage was lowered into the pre-chilled resonator which was filled with a brine of salinity $S \approx 131\text{\textperthousand}$. With the resonator in place inside the pressure vessel, the piston of the shaker and hydrophone were positioned near the top of the brine, and the vessel was quickly sealed and pressurized with nitrogen to approximately 25 atm. The height of the sample column, h, was determined by viewing a video monitor which was connected to a camera placed inside

the pressure vessel and aimed at the top of the resonator. The vector signal analyzer recorded an acoustic spectrum given by the linear frequency-domain average of 30 transfer functions over a frequency range which was determined based upon the resonance frequencies observed for each sample and hydrostatic pressure. After recording each spectrum, a small amount of gas was vented from the chamber to slightly reduce hydrostatic pressure in the vessel. Measurements were repeated at decrementing pressures until the acoustic signal was no longer discernible. Shifts in resonance frequencies were often observed during pressure reduction; however, no spectral changes were seen more than 10 seconds after pressure reduction. To ensure stability of the system, measurements were performed 120 seconds after each pressure reduction.

For each recorded spectrum, sound speed was calculated by the slope method described in Sec. 3.2.4.2, taking only the two lowest-frequency resonance peaks. At high hydrostatic pressures, several resonance peaks were distinct over the frequency range and a linear fit of the resonance frequencies versus mode number showed a low coefficient of determination. However, at low hydrostatic pressures, higher-mode resonances faded and became indistinguishable. Thus, for consistency, only the two lowest resonance frequencies were used for all spectra.

The experimental design was tested by measuring the sound speed of degassed distilled water. Without the copper wire sample holder in the resonator, in-resonator sound speed was found to be 1304 m/s. After accounting for the elastic waveguide effect of the borosilicate tube using the Matlab script

provided in Appendix D.5, the freefield acoustic velocity of the distilled water was determined to be 1466 m/s, approximately 1.6% lower than the predicted value. Next, the empty copper cage was placed in the resonator with the distilled water and the measurement was repeated. The presence of the cage in the resonator had minimal effects on the overall structure of the acoustic spectrum of the water column, and the addition of the cage to the resonator resulted in a 1.2% increase in sound speed measurement. Data from this test are provided in Appendix B.2.

4.5 Results

During the experiments on methane hydrate samples it was observed that the acoustic spectra captured at hydrostatic pressures above 5 atm to 10 atm showed impressive signal-to-noise ratios with distinct peaks at resonance frequencies and deep valleys at antiresonances. Figure 4.3 gives color-scaled plots of the acoustic spectra obtained for each of the four samples. Hydrate behavior is exemplified most clearly in the spectra obtained for the GMsII sample. In Fig. 4.3d, above 10 atm we see several dark red resonance peaks spaced approximately 1.5 kHz apart. The regularity of the intervals between resonances indicates a frequency-independent sound speed below 9 kHz, and the >50 dB difference between peak and valley receiver voltages implies a low-noise system with little acoustic loss. For the sample shown in Fig. 4.3d, hydrate dissociation is evident below 10 atm, where we see higher-frequency resonance peaks begin to flatten and all resonances shift lower in frequency.
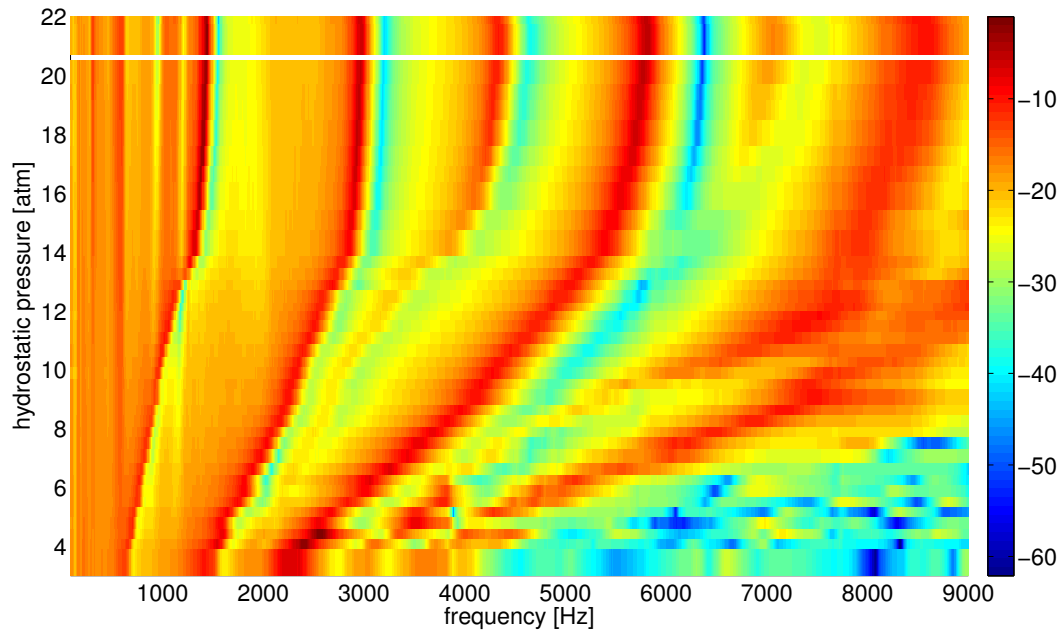
(a) sample CMsI
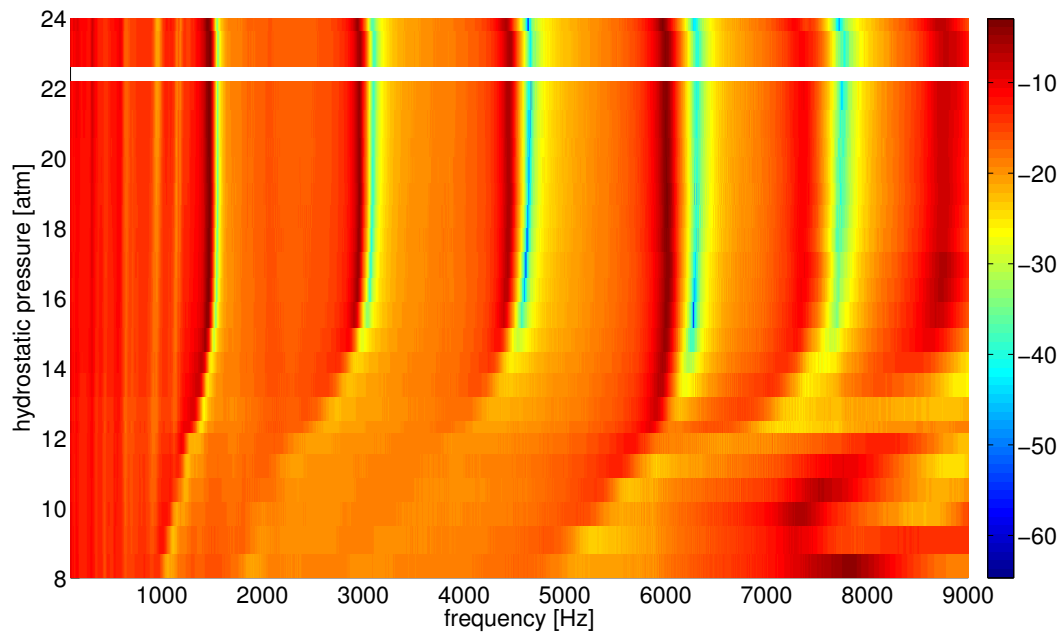
(b) sample CMsII

Figure 4.3: Acoustic spectra of hydrates mixtures, with color scales given in arbitrary decibels. Horizontal white bands appear at pressures where spectra were not recorded due to lack of observed acoustic activity.
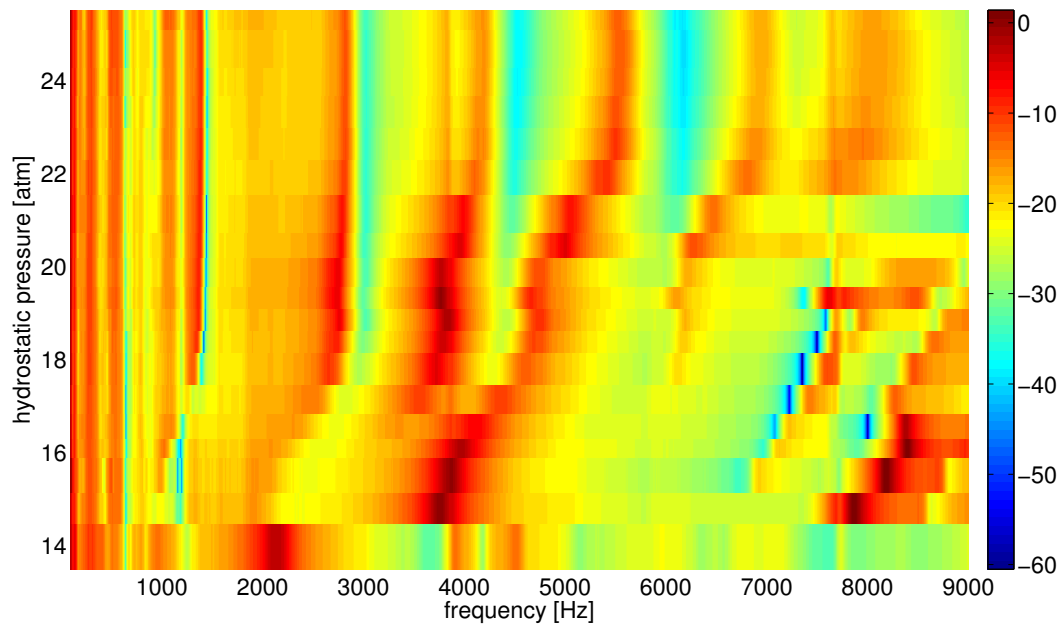
(c) sample HMsI
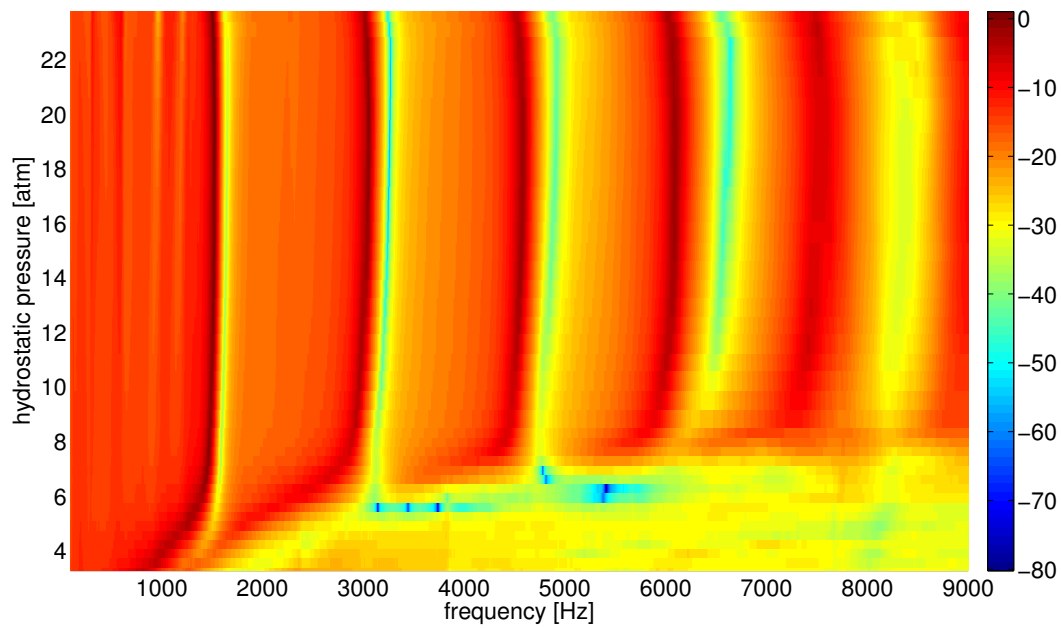
(d) sample GMsII

Figure 4.3: Acoustic spectra of hydrates mixtures over a range of hydrostatic pressures from 3 atm to 25 atm. Color scales are given in arbitrary decibels.

As the hydrate dissociates, bubbles form on and are released from the samples. The introduction of bubbles then lowers the effective sound speed of the bulk medium in the resonator, thus, shifting resonances lower in frequency. The rising bubbles in the column reduce signal-to-noise ratios, due in part to flow-generated noise, and due in part to the conversion of acoustic energy into heat during oscillation of the excited bubbles. Mass, volume, density, brine salinity, and sound speed measurements of the stable hydrate samples are provided in Appendix B.3.

4.5.1 Acoustic Measurements of Bulk Moduli

A primary goal of the experiment on gas hydrate samples was to determine material properties of the hydrates using low-frequency acoustic techniques. The bulk modulus is a key material descriptor, and is easily calculated with the data obtained from the present experiment. Before obtaining measurements of the gas hydrate bulk moduli, the procedure was performed on samples of gum rubber to serve as a proof-of-concept of the experimental design.

Six natural gum rubber balls were placed in the sample cage, the column was filled with distilled water, and sound speeds of the mixture were calculated over a range of pressures from 9 atm to 1 atm. Data obtained in this test are provided in Fig. A.3 of the Appendix. The freefield acoustic velocity of the bulk medium was calculated by accounting for the elastic waveguide effect of the borosilicate tube using the code provided in Appendix D.5. Let-

ting c_{m} be the freefield acoustic velocity, Eq. 4.4 was used to determine for the bulk modulus, B, of the rubber balls, calculated as $B = \kappa^{-1}$. This calculation, which parallels the method of bulk modulus measurement presented by Richardson et al. [135], yields a value of approximately 1.81 GPa. The exact makeup of the gum rubber balls and the process through which they may have been vulcanized is not known; however, the value measured in this test is bracketed by established values of natural rubber bulk moduli, which have been measured at 1.69 GPa (Ref. [136]) to 1.95 GPa (Ref. [137]). This notably accurate calculation of a key material property of gum rubber samples gave confidence that the experimental procedure may be an effective means of measuring the acoustic properties of methane hydrates.

Figure 4.4 shows the measured effective sound speeds, c_{m}, of the bulk media of four separate methane hydrate samples in brine, plotted as a function of hydrostatic pressure over a range of 27 atm to 3 atm. To create this plot, sound speeds were calculated by the slope method (described in Sec. 3.2.4.2), using only the two lowest-frequency resonances from the spectrum recorded at each pressure. From this data, bulk moduli of the stable hydrate samples were calculated in a method similar to the bulk modulus measurements of the gum rubber balls.

At high pressures, where the hydrates appeared to be stable, the resonator column was assumed to be filled with a two-phase acoustically-homogeneous solution which could be described by Wood's model. Stability of the hydrates was confirmed by an absence of bubbles observed in the video monitor. Af-
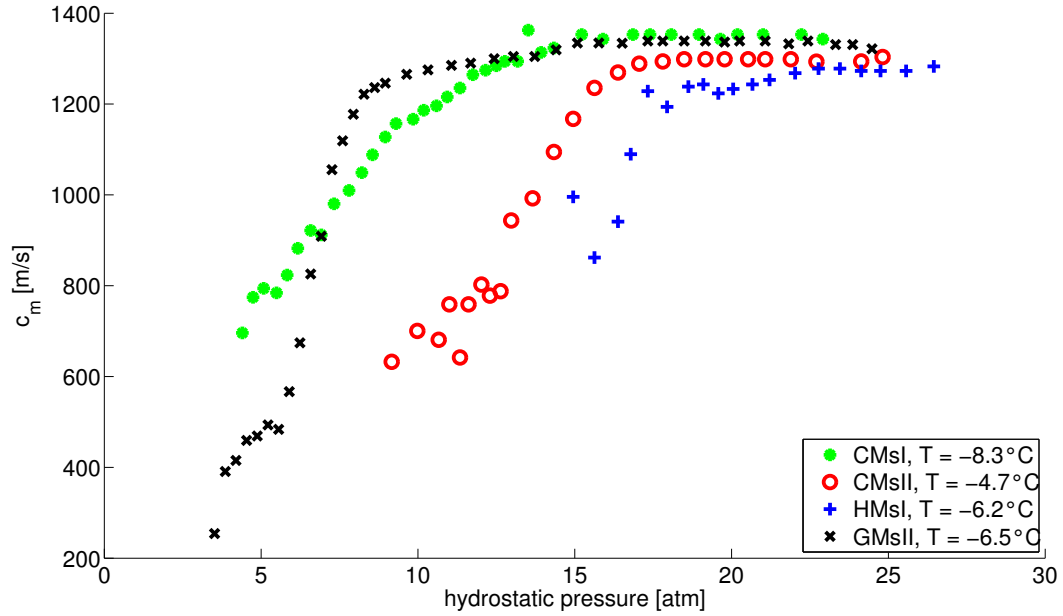
Figure 4.4: Measured sound speeds of hydrate mixtures.

ter accounting for the elastic waveguide effect of the borosilicate resonator (described in Sec. 3.2.5), the bulk modulus of each hydrate sample was determined by Eq. 4.4. Sample densities were evaluated as $\rho_h = m_h/V_h$, where the sample masses were measured with a digital decigram balance. Hydrate sample volumes were determined by observing the change in liquid level inside the resonator, ΔL, as the samples were added. The expression for the volume of fluid displaced by the hydrates in the cylindrical resonator, $V_h = \Delta L \pi d_i^2/4$, gave the volume of the hydrate samples. The volume of brine in the resonator and the volume of the hydrate were used to calculate the volume fraction, as in Eq. 4.1. Measured densities and bulk moduli are presented in Table 4.2 alongside properties of hydrates which have been taken from the literature.

sample	f_meas [kHz]	ρ_h [kg/m^3]	B_h [GPa]
CMsI	0.1 to 3.5	1029	2.8
CMsII	0.1 to 3.5	2050	0.4
HMsI	0.1 to 3.5	1497	0.3
GMsII	0.1 to 3.5	1326	1.7
Lee et al.	500 to 800	920	6.4
Helgerud et al.	not given	900	7.9
Waite et al.	1000	900	7.7 ± 0.5
Pandit and King	820	750 to 850	5.7 ± 0.1

Table 4.2: Properties of methane hydrate samples of the present experiment compared to values determined by Lee et al. (Ref [138]), Helgerud et al. (Ref. [139]), Waite et al. (Ref. [140]), and Pandit and King (Ref. [141]). Frequency range used in measurement is indicated by f_meas.

Values used to calculate bulk moduli are provided in Table B.3 of the Appendix.

In Table 4.2, we see that the bulk moduli measured in the present experiment are lower than previously measured values. Three possible explanations are presented to account for this discrepancy. First, during the experiment the video monitor used to measure brine column height became clouded with an oily film which was released from the hydrate samples. This may have resulted in inaccurate measurements of hydrate sample density and volume fraction—two key terms in the expression used to calculate the bulk modulus. For the four samples of the present experiment, an estimate of the length uncertainty is ± 2 mm in liquid level, which results in 12% to 28% error in bulk modulus measurement.

The oily substance released from the hydrate samples is an indicator

of a second potential source of error—impurity. A pure gas hydrate would contain only H_2O-ice and gas molecules, and should have an appearance similar to ordinary water ice, yet the samples in the present work visibly contained a significant mud and clay content (see Fig. A.5 in the Appendix). This could explain the high density measurements of the samples. However, the literature shows that values of sediment bulk moduli are typically similar to or greater than the established values we have seen for gas hydrates [135, 142, 143]. Wood's model defines the effective bulk modulus of a medium as a linear combination of the bulk moduli of the constituents of the medium. Therefore, any presence of high-bulk-modulus sediment in a sample should result in a measurement of the effective bulk modulus of the sample which is equal to or greater than the bulk modulus of the hydrate in the sample. Thus, we can assume that the low measured values of bulk moduli were not a result of the presence of sediment in the samples.

The most plausible explanation for the differences we see between bulk moduli measured in the present experiment and values from the literature stems from the very motivation of this work: It is known that gassy sediments and composites can exhibit highly frequency-dependent behavior, such that the acoustic velocity of a gassy sediment at high frequencies may be more than an order of magnitude greater than its acoustic velocity below the resonance frequency of the gas bubbles in the sediment [124, 125]. From the expression

for the speed of compressional sound propagation through a solid,

$$c(\omega) = \sqrt{\frac{B(\omega) + \frac{4}{3}G(\omega)}{\rho}},$$
(4.9)

where G is the shear modulus of the solid, we see that a frequency-dependent sound speed implies highly frequency-dependent elastic moduli. For example, the tenfold difference between low- and high-frequency sound speeds which has been observed in gassy sediments relates to a hundredfold difference in elastic moduli. Given the vast difference between the frequencies used in the present experiment and the measurement frequencies found in the literature, it is quite possible that all of the bulk moduli listed in Table 4.2—the established high-frequency values, as well as the low-frequency values of the present experiment—are correct. It is likely that the frequency-dependent behavior of the elastic moduli of methane hydrates is the the primary cause of the differences between bulk moduli which have been measured at ultrasonic frequencies and the values measured in this work.

4.5.2 Acoustic Measurements of Dissociation Pressures

In addition to bulk modulus measurements, the acoustic tests of the present experiment clearly show stability regimes of the hydrate samples in their given pressure-temperature conditions. Inspection of Fig. 4.4 shows relatively constant sound speeds of the mixtures at high hydrostatic pressures. As pressure in the chamber decreased, the hydrates began dissociation and sound speeds decreased significantly. As part of the analysis of the data presented in Fig. 4.4, dissociation pressures were determined by interpolating the pressure
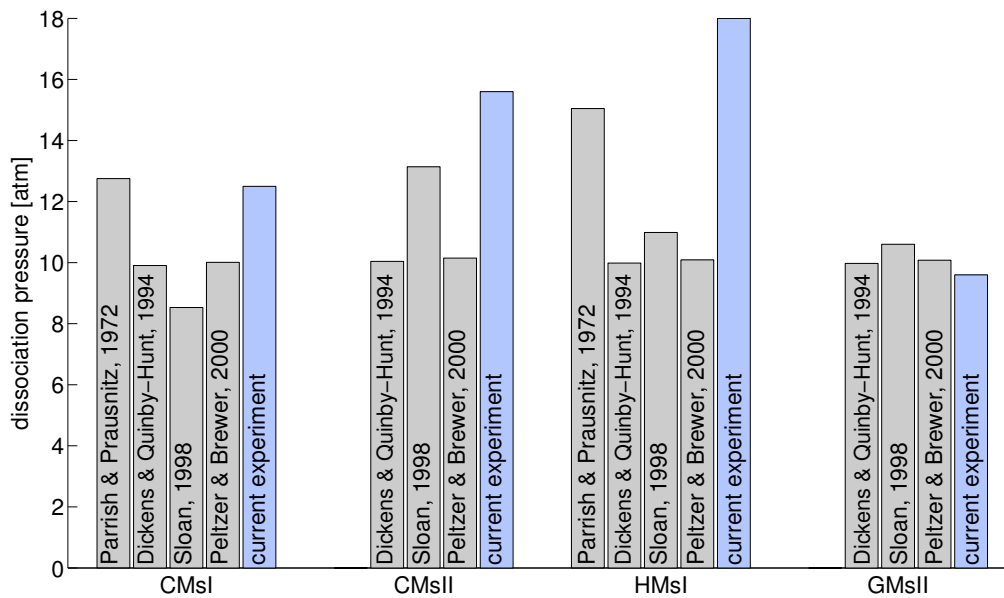
Figure 4.5: Comparison of predicted and acoustically-determined methane hydrate dissociation pressures. Predicted values trend lower than dissociation pressures found acoustically, likely due to the models' neglect of salinity.

at which c_m fell below 95% of the mean of the values of c_m corresponding to the ten highest-pressure data points for each sample. These acoustically-determined dissociation pressures are presented in Fig. 4.5, where they are compared with values predicted by several common models of methane hydrate behavior. The Parrish and Prausnitz model applies only to structure I methane hydrates, and thus does not appear for comparison to experimental data of samples CMsII and GMsII. For samples CMsI and HMsI, the Parrish and Prausnitz predictions appear to be outliers among the model predictions, possibly due to the sample temperature, which in the present experiment was below the 0°C to 27°C range validated in their paper.

Neglecting the Parrish and Prausnitz model, it is evident from Fig. 4.5 that the model predictions for samples CMsI, CMsII, and HMsI trend lower than dissociation pressures determined acoustically. This discrepancy is likely caused by the use of a strong brine in the experiment, as this level of salinity is not taken into account in any of the models. The models may have failed to accurately predict dissociation pressures because they did not fully account for the activity of the fluid molecules surrounding the sample. Although the presence of simple salts does not directly affect the hydrate's enthalpy of formation, dissolved ions in the fluid decrease the entropy of the water molecules, thus decreasing dissociation temperatures [132]. As temperature was held constant in the present experiment, and hydrate dissociation pressure and temperature have an inverse relationship, the high-salinity brine effectively increased the pressure at which the hydrate samples became unstable.

A striking observation, then, is each of the models' seemingly accurate predictions of the dissociation pressure of sample GMsII. The sample was suspended in a brine of 132‰ salinity, yet all three models predict dissociation pressures within 6% of the acoustically-determined value. Here, we are likely seeing not impressive accuracy of the models, but a coincidence of two opposing errors. The first error is caused by the salinity of the host solution, which raises dissociation pressure, and the second error relates to the chemical composition of the gas in the hydrate samples. An overview of the major components of the gas in the samples is given in Table 4.3. While the gas in samples CMsI and HMsI was almost purely methane, and over 80% of the gas

sample	T [°C]	CH$_4$ [%]	C$_2$H$_6$ [%]	C$_3$H$_8$ [%]	C$_4$H$_{10}$ [%]
CMsI	-8.3	99.79	0.21	-	-
CMsII	-4.7	81.89	10.4	3.7	1.40
HMsI	-6.2	99.49	0.14	0.12	0.15
GMsII	-6.5	29.67	15.35	36.61	13.61

Table 4.3: Temperature and major components of gas in hydrate samples. Compositions were determined with a Varian Saturn 2200 mass spectrometer, then quantitatively determined with a Varian CP 3800 gas chromatograph, as described in Ref. [144]. Percentages of butane and isobutane have been combined in the C$_4$H$_{10}$ column.

in sample CMsII was methane, sample GMsII contained a gas comprised of less than 30% methane. Lu et al. experimentally proved a relationship between the gas composition and the stability of a hydrate, showing that stucture I hydrates containing nearly pure methane were the least stable, while structure II hydrates with significant propane and butane constituents dissociated at much lower pressures [144].

4.6   Discussion of Methane Hydrates Experiment

A proof-of-concept test of the experimental procedure and apparatus used in the present experiment gave promising results. For samples of gum rubber, a bulk modulus of 1.81 GPa was measured. This value falls squarely within the range of established bulk moduli of natural gum rubber. When the test was repeated with natural methane hydrates placed in the sample cage, bulk modulus measurements returned values well below those found in the literature. It is possible that a sediment or other impurities in the hydrate

samples had a small effect on the measurements. It is also possible that the sample density and volume fraction measurements were inaccurate due to an obscured view of the level of liquid in the resonator column. As these are key elements of Wood's equation, errors in the measurement of sample density and volume fraction would affect calculated values of bulk moduli. However, it is likely that we are observing the highly frequency-dependent behavior of gassy sediments, explaining why the low-frequency measurements of the present experiment trend lower than the ultrasonic measurements found in the literature. If this is the case, then it is surprising that the low-frequency elastic properties of methane hydrates have not previously been investigated in greater depth. And if bulk moduli of methane hydrates do exhibit such highly frequency-dependent behavior, this must be considered in acoustic mapping and seismic surveys of hydrate-rich regions, as well as in future measurements of the acoustic properties of gas hydrates.

The acoustic measurements of gas hydrate dissociation pressures proved successful. Quantitative error analysis of the experiments is difficult, due in part to unknown effects introduced by sediment in the samples. Moreover, the complex nature of gas hydrates has prevented scientific consensus on any model of hydrate stability. Without established laws of hydrate behavior, exact degrees of error associated with the present measurements cannot be determined. Nonetheless, the acoustically-measured hydrate dissociation pressures are in rough agreement with the available empirical models of hydrate stability. Previous laboratory investigations have measured changes in hydrate

mass or pressure changes in a sealed chamber containing hydrate samples to determine gas hydrate dissociation conditions; however, to the knowledge of the author, no other study has exploited low-frequency acoustics as a tool to measure hydrate dissociation. Given that seismic and low-frequency acoustic techniques are the primary means by which gas hydrates are located, and are common techniques for monitoring hydrate stability, this work may inform current practices and improve the accuracy and effectiveness of in situ measurements.

The present experiment would certainly benefit from a more accurate knowledge of the exact constituents of the samples, or from repeating the procedure with artificial samples of pure methane hydrate. The apparatus and procedures used in this experiment were developed for this work, and thus, have not been sufficiently proven. Additional measurements of the bulk moduli of known materials are necessary to prove the experimental design as an accurate means of determining elastic properties of materials, and tests on pure methane hydrate samples may yield more idealized dissociation pressure measurements. Furthermore, improved confidence in the bulk modulus measurement of a stable methane hydrate sample would allow for analysis of the three-phase case of methane gas, solid hydrate, and liquid, which arises in nature and in the experimental apparatus as the hydrates leave their stability zone.

Chapter 5

Conclusions

Motivations, procedures, and results of three separate experiments have been presented in this thesis. Each of the experiments sought to develop or improve upon low-frequency acoustic techniques of localization, characterization, and monitoring of natural methane hydrates and methane gas ebullition in underwater environments. For this work, methods were developed to measure and monitor single-seep gas flux using passive acoustic remote sensing. Simply by "listening" to the sounds of bubbles as they are released into a liquid, their sizes were determined to a high degree of accuracy. A similar passive acoustic measurement of ebullition from a natural methane gas seep has been performed in situ by Leifer and Tang, however their results showed approximately 20% error. To the knowledge of the author, no other study has successfully used passive acoustic recording to measure gas quantities with a level of accuracy comparable to that of the measurements presented in this thesis. A logical next step in the development of this work would bring the measurement apparatus to a natural methane seep site for an in situ application of the techniques.

It is understood that where ebullition exceeds a certain rate, sounds

84

simultaneously radiated by multiple bubbles will become difficult to resolve. In such cases, it may be useful to consider the bubbly water to act as a bulk acoustic medium with an effective density and compressibility. A measurement of the low-frequency sound speed of such a medium and knowledge of the properties of its constituents could then be exploited to determine the volume fraction of gas in the bubbly liquid using Wood's model. Knowledge of the volume fraction of gas in a bubbly liquid implies a knowledge of quantity of gas in the water column, and thus, a measure of methane ebullition.

Conventionally, Wood's model has been applied with the assumption that the bubbles in the medium it describes behave as an ideal gas. However, as we apply the model to natural methane seep sites, where water depths exceed 50 m, the bubbles of methane in the liquid cannot be modeled as an ideal gas. Chapter 3 highlighted the need to account for the real gas behavior of bubbles in liquids by showing significant differences between measured sound speeds of bubbly media at elevated pressures and sound speeds predicted by Wood's model of a liquid containing ideal gas bubbles. A modified form of Wood's model was developed to account for real gas behavior by considering the compressibility factor of a gas, given its surrounding hydrostatic pressure and temperature conditions. Pressure-dependent sound speeds of a liquid containing bubbles of sulfur hexafluoride were measured, showing respectable agreement with the real-gas form of Wood's model described in Ch. 3. Relating these results to methane hydrates in natural environments, the low-frequency propagation of sound through a two-phase medium of methane bubbles in

deep or shallow water can now be accurately described by the model which was developed for this work.

An investigation of the low-frequency acoustic behavior of solid methane hydrates was presented in Ch. 4 of this thesis. Motivations behind the hydrate experiment were twofold: One goal of this work was to bridge the divide between tabulated properties of gas hydrates, which are typically measured in the laboratory at frequencies in the hundreds of kilohertz range, and in situ behavior of hydrate deposits, which are surveyed at seismic frequencies, several orders of magnitude below the frequencies of the laboratory measurements. The second goal of this experiment was to calibrate a method for acoustic determination of the stability of gas hydrates in a laboratory pressure chamber. The intent was to develop the techniques to be applicable to laboratory experiments and in situ tests performed in natural underwater environments. The laboratory test proved successful, showing the subtle temperature-pressure sensitivities of four gas hydrate samples as they were gradually brought from simulated GHSZ conditions to lower pressures, where dissociation was evident.

The equivocal nature of conventional seismic surveys results in limited effectiveness of hydrate and seep location and quantification. Improved understanding of the low-frequency acoustic behavior of methane gas bubbles and methane hydrate deposits may inform the practice and analysis of seismic and acoustic surveys of methane-rich regions. The objective of this thesis has been to gain a better understanding of the low-frequency acoustic behavior of methane in many of the forms in which it found in nature—as a hydrate, as a

hydrate in water, and as gas in water, at atmospheric as well as elevated pressures. Future work may combine the principles detailed in the development and analysis of each of the three main experiments described in this thesis. For example, a multimodal remote sensing system may monitor methane ebullition of a seep by passively analyzing sounds radiated by newborn bubbles while accounting for the real gas behavior of methane bubbles at depth. At increased rates of ebullition, the system may rely on active techniques to acoustically measure the void fraction, and thus, quantify the methane content of the bubbly liquid in the water column. Further development yet, would allow for the detection and analysis of the three-phase case of methane-hydrate-coated bubbles in salt water at the pressures and temperatures found in the stability zone of gas hydrates. Much work is yet to be done, but the experiments and models developed in this thesis may offer climate and energy researchers a few small stepping stones on their path toward a better understanding of the curious compounds we call methane hydrates.

Appendices

Appendix A

Supplemental Figures
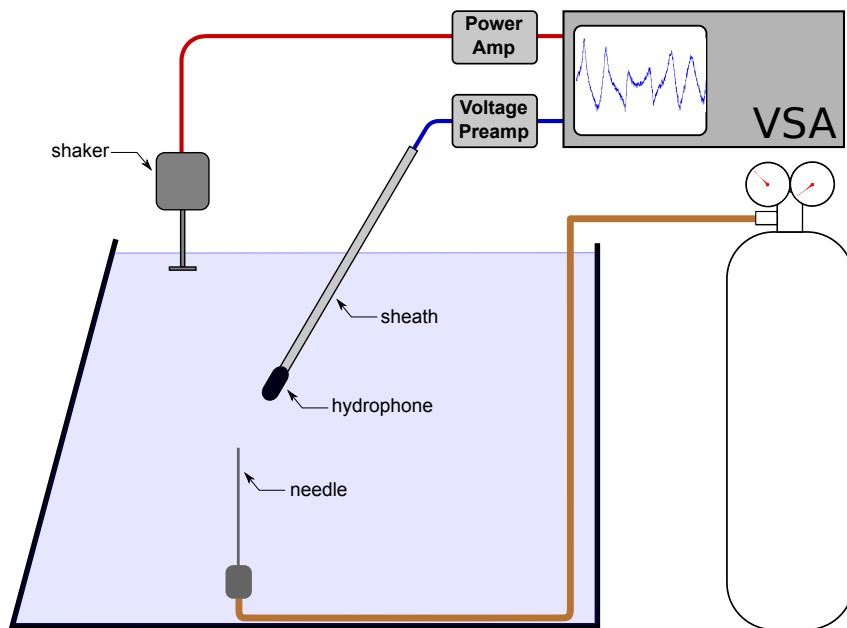
Figure A.1: Schematic of transfer function measurement for determination of water tank resonances, as described in Sec. 2.6. Gas flow was off during transfer function measurements.
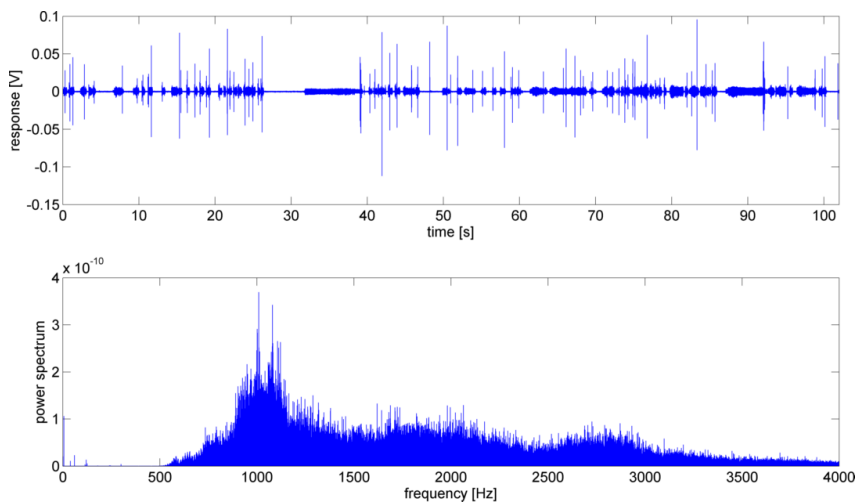
Figure A.2: (a) Time signal and (b) power spectrum of an SNB2 recording described in Sec. 2.6.3.
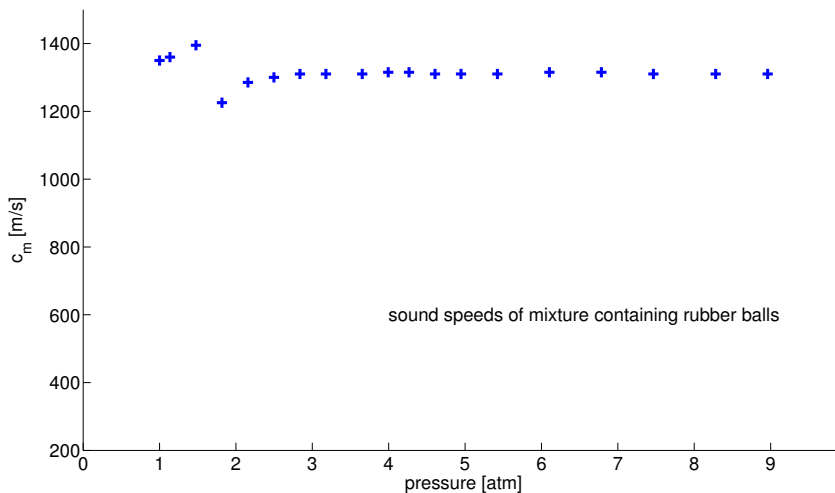
Figure A.3: Sound speeds of mixture containing rubber balls, as described in Sec. 4.4. As expected, sound speed remains relatively constant as a function of hydrostatic pressure. Some variation in sound speed appears between 1 atm and 2 atm, likely due to the resonance of a single bubble which came out of solution during depressurization.
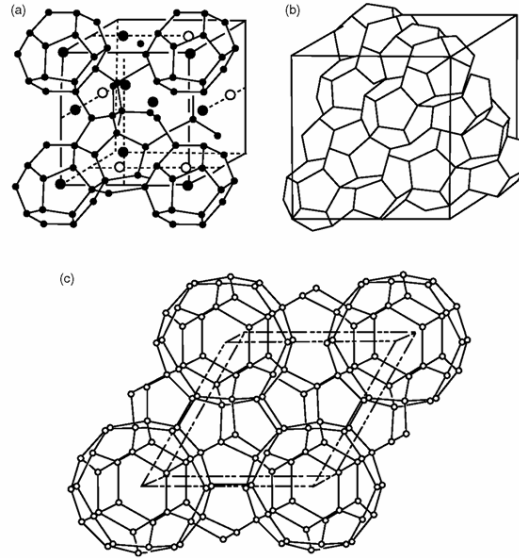
Figure A.4: Gas hydrate unit molecular unit diagrams (a) structure I, (b) structure II, and (c) structure H. Graphic reprinted from Ref. [103].

Figure A.5: Photograph of a methane hydrate sample used in the experiment described in Ch. 4. A significant percentage of mud content in the sample may have contributed to the discrepancy between tabulated properties of methane hydrates and results of the present experiment.

Appendix B

Tabulated Data

gas	ν	$\rho_{g,0}$ [kg/m^3]	$c_{g,0}$ [m/s]	T [℃]	$c_{l,0}$ [m/s]
air	1.18	1.2	315.7	22.3	1489
SF$_6$	-	6.164	139.8	23.0	1491

Table B.1: Properties of air and sulfur hexafluoride used in the bubbly liquids experiment. The polytropic index of air at STP is given by Wilson (Ref. [89]), the STP density of air is taken as its standard value, $c_{g,0}$ is calculated by Eq. 3.31, density of SF$_6$ is calculated from values given in Ref. [145], $c_{g,0}$ for SF$_6$ is interpolated from tabulated data given by Ref. [100], and sound speed of the distilled water is calculated using the temperature- and pressure-dependent expression given by Eq. 5.22 of Ref. [90].

	T	L	$c_{m,m}$	$c_{m,f}$	$c_{w,theo}$	error
distilled water	[°C]	[mm]	[m/s]	[m/s]	[m/s]	[%]
without copper cage	22.6	460	1304	1466	1490	1.6
with copper wire cage	21.8	433	1320	1485	1488	0.2

Table B.2: Data from an experiment to determine the effect of a copper wire cage (sample holder) in the resonator on sound speed measurments. Sound speed calculations were performed on distilled water in a borosilicate tube resonator with and without a copper cage in the resonator. Presented are the water temperature, T; water level, L; measured sound speed of the mixture, $c_{m,m}$; freefield sound speed of the mixture, $c_{m,f}$, as calculated by the Lafleur and Shields model; theoretical sound speed of distilled water, $c_{w,theo}$ for the given temperature at atmospheric pressure; and percent error. Error is calculated as deviation from theoretical sound speed of pure distilled water. It is evident from this data that the presence of the copper wire cage in the resonator has a small $< 1.4\%$ effect on sound speed measurement.

	S	m_h	ρ_h	h_0	h_1	$c_{m,m}$	$c_{m,f}$
sample	[‰]	[g]	[kg/m^3]	[mm]	[mm]	[m/s]	[m/s]
gum rubber	0	44.6	1402	433	446	1312	1497
CMsI	131	28.4	1029	427	440	1353	1558
CMsII	130	30.4	2045	430	437	1298	1478
HMsI	132	31.8	1497	435	445	1266	1431
GMsII	132	36.6	1326	426	439	1335	1537

Table B.3: Data log from measurements on methane hydrates. Table shows brince salinity, S; sample mass, v; sample density, ρ_h; liquid level without sample, h_0; liquid level with sample, h_1; measured sound speed of the stable mixture, $c_{m,m}$; and the freefield sound speed of the stable mixture, $c_{m,f}$, as calculated by the Lafleur and Shields model. The value ΔL is given by $h_1 - h_0$.

Appendix C

Hydrate Stability Models

For a structure I methane hydrate in the temperature range of 0°C to 27°C, Parrish and Prausnitz fit data to a model based on the work of Van der Waals and Platteeuw to predict hydrate dissociation conditions as

$$\ln P = -1212.2 + 44344.0/T + 187.719 \ln T, \tag{C.1}$$

where P is hydrostatic pressure in atmospheres and T is temperature kelvin [130]. Dickens and Quinby-Hunt described the dissociation pressure and temperature of a hydrate in salt water of salinity $S = 33.5‰$ by

$$\frac{1}{T} = 3.79 \times 10^{-3} - 2.83 \times 10^{-4} (\log_{10} P), \tag{C.2}$$

where P is in MPa and T is temperature kelvin [132]. Sloan offered

$$P = \exp(38.98 - 8533.8/T), \tag{C.3}$$

where P is in kPa and T is temperature kelvin [9]. Using Sloan's data, Peltzer and Brewer expanded upon Dickens and Quinby-Hunt's model to obtain

$$\frac{1}{T} = 3.83 \times 10^{-3} - 4.09 \times 10^{-4} (\log_{10} P) + 8.64 \times 10^{-5} (\log_{10} P)^2, \tag{C.4}$$

where P is pressure in MPa and T is temperature kelvin [133].

Appendix D

Matlab Scripts

D.1   Optical Analysis

```matlab
for framenum = 1:3305;
vidfile = 'v26';
mov=aviread([num2str(vidfile),'.avi'],framenum);

needlepx=103-79; % enter width of needle in pixels
needleOD = 0.018; % [inches] outer diameter

[picfile,map] = frame2im(mov(1));
RGB = picfile;
imsz = size(RGB);
RGB = imresize(RGB, [imsz(1) .5*imsz(2)]);
RGB=imrotate(RGB,-90);

% figure(1)
% subplot(1,2,1)
% imshow(RGB);
% xlabel('original image')
% subplot(1,2,2)
threshold = graythresh(RGB);
BW = im2bw(RGB,threshold);
% imshow(BW);
% xlabel('high-contrast image')

dim = size(BW);
col = round(dim(2)/2);
row = find(not(BW(:,col)),1)-1;
connectivity = 8;
num_points  = 500;
try
cont = bwtraceboundary(BW, [row, col], 'W',...
```

```matlab
 connectivity, num_points);

% figure(2)
% imshow(RGB);
% hold on;
% plot(cont(:,2),cont(:,1),'g','LineWidth',2.5);

for n=min(cont(:,2)):max(cont(:,2))
    ind = find(cont(:,2)==n);
    vals = cont(ind,:);
    x(n)=max(vals(:,1))-min(vals(:,1));
end
xtot=sum(x);

px_per_in=needlepx/needleOD;
area = xtot/px_per_in^2;
r_mm = in2mm(sqrt(area/pi));
xlabel([num2str(picfile)])
v_sphere_ml = (4/3)*pi*(r_mm/10)^3;

handle= figure(2); %
el = fit_ellipse(cont(:,2),cont(:,1),handle);

el_a = in2mm(el.a/px_per_in); % [mm] major radius of ellipse
el_b = in2mm(el.b/px_per_in); % [mm] minor radius of ellipse
v_os = (4/3)*pi*(el_a/10)^2*(el_a/10);%[ml] vol obl. spheroid
% xlabel('')

if length(cont)<num_points
save(['bubvols_',num2str(vidfile),'_',num2str(framenum)...
,'.mat'],'vidfile','framenum','el_a','el_b','v_os')
end
catch
end
clc
vidfile
clear
end
```

D.2 Passive Acoustical Analysis

```matlab
%% inputs
bubdata = importdata('PR100316_32.txt');
method = 'analyze'; % 'plot' or 'analyze'
temp = 34.7; % [  C ] temperature
p_bar = 1.0183; % [bar] barometric pressure
hw = 0.333; % [m] height of water
hn = 0.185; % [m] height of needle
G = 100; % [mV] gain on charge amp

dh=.025; % [m] distance from needle to hydrophone
c_b = 331.5*sqrt(1+temp/273.15);
rho_l = 997;

nu=1.366;
P_inf=bar2Pa(1.0183)+rho_l*9.81*(hw-hn+.03);
rho_b = P_inf/(287.05*(temp+273.15));

indstart = 1;
indend = length(bubdata);
fontsize=14;

T = bubdata(indstart:indend,1);
Y = bubdata(indstart:indend,2);
Y = Y-mean(Y);

figure(1)
subplot(2,1,1)
plot(T,Y)
ylabel('response [V]')
xlabel('time [s]')
xlim([0 max(T)])

fmax = 4000; % max frequency of interest for power spectrum
fs = 1/(T(2)-T(1)); % [Hz] sampling rate

switch method
case 'analyze'

%% Plot and solve for multiple bubbles
AutoBubPlot = 'y'; % y or n to plot and solve
 % for multiple bubbles automatically
```

```matlab
tb = .02; % [s] time between bubbles
amplthresh = .015; % amplitude threshold
PS_thresh = .2e-3; % threshold for power spectrum peak finder
bubplot=297; % highest bubble number to plot
plotall = 'n'; % 'y' to plot all bubplot bubbles
n2val = 'fixed'; % ['thresh', 'threshplus', or 'fixed']
 % defines n2 of individual bubble window
 % thresh only works for amplitude over a
 % certain threshold, threshplus adds tb to
 % thresh, and fixed makes tb same for
 % every bubble

ttt=[0 10 15 20 25 30 40 50 60 70 80 100];
ggg=[75.7 74.2 73.5 72.75 72 71.2 69.6 67.9 66.2...
 64.4 62.6 58.8]/1000;
sigma = interp1(ttt,ggg,temp); % [N/m] surface tension

switch AutoBubPlot
    case 'y'
    clear t1 t2 tpad npad n N bubdata ttt ggg
    indie = find(abs(Y)>amplthresh);
    x=1;
    for n=1:length(indie)-1
        if T(indie(n+1)) - T(indie(n)) < tb
            bubnum(n)= x;
        else
            x=x+1;
            bubnum(n)=x;
        end
    end
    bubnum(n+1)=bubnum(n);

    bubtot=bubnum(length(bubnum));
    for n=1:bubplot

    xx=find(bubnum==n);
    n1=indie(xx(2));
    switch n2val
        case 'thresh'
            n2=indie(xx(length(xx)));
        case 'threshplus'
            n2=indie(xx(length(xx)))+.8*tb*fs;
        case 'fixed'
            n2 = n1+tb*fs;
    end
```

```matlab
    if plotall == 'y'
        figure(12)
        subplot(bubplot,2,2*n-1)
        plot(T(n1:n2),Y(n1:n2))
        xlim([T(n1) T(n2)])
    end

    y = Y(n1:n2);
    N=length(y);
    npad = 2^ceil(log2(length(y)))-length(y);
    y=[y;zeros(npad,1)];
    tpad = (npad)/fs;
    t=T(n1):1/fs:T(n2)+tpad;

    p = abs(fft(y))/(N/2);
    p = p(1:floor(N/2)).^2;
    freq = [0:(floor(N/2)-1)]/(max(t)-min(t));

    for nn = 1:length(freq)
        if freq(nn) <=fmax
            nmax = nn;
        end
    end
    p = p(1:nmax);
    freq = freq(1:nmax);

    if plotall == 'y'
        figure(12)
        subplot(bubplot,2,2*n)
        plot(freq,p)
        xlim([0 fmax])
    end

%     for nn=10:length(p)-3;
%         if p(nn) > p(nn+1) && p(nn+1) > p(nn+2) && p(nn+2)...
% > p(nn+3) && p(nn) > p(nn-1) && p(nn) > p(nn-2) && p(nn) >...
% p(nn-3) && p(nn) > PS_thresh
%             resfreq = freq(nn);
%             peakn=nn;
%         end
%     end
%     peakval = p(peakn);

        for nn=1:length(p)
        peakval = max(p(10:length(p)));
```

```matlab
        if p(nn) == peakval
            resfreq = freq(nn);
        end
        end

if plotall == 'y'
    hold on
    plot(resfreq,peakval,'ro')
end

resfreqlog(n) = resfreq;
a_b(n) = c_b/(2*pi*resfreq)*sqrt(3*rho_b/rho_l);
bubvol(n) = (4/3)*pi*(a_b(n)*100)^3; % [ml] bub vol

a=7e-4:1e-5:10e-3;
n_b=1.4; % same as ratio of specific heats for gas
fb = (1./(2*pi.*a*sqrt(rho_l))).*sqrt(3*(rho_b*(c_b^2) + ...
n_b*2*sigma./a) - 2*sigma./a);
a_b_2(n)=interp1(fb,a,resfreq);
bubvol_2(n) = (4/3)*pi*(a_b_2(n)*100)^3; %[ml] bub vol

a_b_3(n)=(1/(2*pi*resfreq))*sqrt(3*nu*P_inf/rho_l);
bubvol_3(n) = (4/3)*pi*(a_b_3(n)*100)^3; %[ml] bub vol

c_b_2 = sqrt(nu*P_inf/rho_b);
fb_2 = (1./(2*pi.*a*sqrt(rho_l))).*sqrt(3*(rho_b*(c_b_2^2)...
+ n_b*2*sigma./a) - 2*sigma./a);
a_b_4(n)=interp1(fb_2,a,resfreq); % includes surface ...
% tension, as shown on Pierce 9-1.40
bubvol_4(n) = (4/3)*pi*(a_b_4(n)*100)^3; %[ml] bub vol

    figure(1)
    subplot(2,1,2)
    hold on
    plot(T(n1:n2),Y(n1:n2))
end
    xlim([0 max(T)])

if plotall == 'y'
    figure(12)
    subplot(bubplot,2,2)
    title('power spectrum')
    subplot(bubplot,2,2*bubplot)
    xlabel('frequency [Hz]')
    subplot(bubplot,2,1)
```

```matlab
            title('bubble resonance')
            subplot(bubplot,2,2*bubplot-1)
            xlabel('time [s]')
        end
    end
clear a n_b fontsize

Total_volume = sum(bubvol)*(P_inf/bar2Pa(p_bar))
Total_volume_2 = sum(bubvol_2)*(P_inf/bar2Pa(p_bar))
Total_volume_3 = sum(bubvol_3)*(P_inf/bar2Pa(p_bar))
Total_volume_4 = sum(bubvol_4)*(P_inf/bar2Pa(p_bar))
end

sig=max(Y); % [V] peak signal voltage
SPL_at_rec=20*log10(sig/((G/1000)*sqrt(2)*1e-6))% SPL @ rec.
sig_1m=sig*(dh/1)^2; % assuming spherical spreading
SPL_at_1m=20*log10(sig_1m/((G/1000)*sqrt(2)*1e-6))% SPL @ 1m
```

D.3 Compressibility Factor Calculator

```matlab
function[Z_calc] = compressibility(gas,T_Kelvin,P_bar)
T = T_Kelvin;
P = P_bar;

switch gas % critical properties from airgas.com
    case 'air'
    Tc = C2K(-140.5); % critical temperature
    Pc = 37.71; % [bar] critical pressure

    case 'CH4'
    Tc = C2K(-82.7); % critical temperature
    Pc = 45.96; % [bar] critical pressure

    case 'SF6'
    Tc = C2K(45.5); % critical temperature
    Pc = 2.26; % [bar] critical pressure

    case 'CO2'
    Tc = C2K(31); % critical temperature
    Pc = 73.825; % [bar] critical pressure

    case 'ethane'
    Tc = C2K(32.2); % critical temperature
    Pc = 48.839; % [bar] critical pressure

    case 'butane'
    Tc = C2K(152); % critical temperature
    Pc = 37.96; % [bar] critical pressure
end
Tr = T/Tc;
Pr = P/Pc;
Z = .2:.0001:1.8;
VanDerWaal = (Z + 27*Pr./(64*(Tr^2).*Z)).*(1 - Pr./(8*Tr.*Z));
ones_vector = ones(1,length(Z));

for n = 1:length(Z);
    if VanDerWaal(n) <= 1
        Z_gen = Z(n);
    end
end
Z_calc = Z_gen;
```

D.4 Generalized Compressibility Plotter

```matlab
% Generalized compressibility factor solver
% Chad Greene 25AUG2009
close all
clear all
clc

%% find Z for specific gas under given T and P
% inputs:
gas = 'CH4';
T = C2K(30); % ambient temp
P = psi2bar(150); % hydrostatic pressure [bar]

%% calculations
switch gas % critical properties from airgas.com
    case 'air'
    Tc = C2K(-140.5); % critical temperature
    Pc = 37.71; % [bar] critical pressure

    case 'CH4'
    Tc = C2K(-82.7); % critical temperature
    Pc = 45.96; % [bar] critical pressure

    case 'SF6'
    Tc = C2K(45.5); % critical temperature
    Pc = 2.26; % [bar] critical pressure
end

Tr = T/Tc;
Pr = P/Pc;

Z = .2:.0001:1.8;

VanDerWaal = (Z + 27*Pr./(64*(Tr^2).*Z)).*(1 - Pr./(8*Tr.*Z));
ones_vector = ones(1,length(Z));

for n = 1:length(Z);
    if VanDerWaal(n) <= 1
        Z_gen = Z(n);
    end
end
```

```matlab
figure(1)
plot(Z,VanDerWaal,Z,ones_vector)
hold on
plot(Z_gen,1,'ro')
axis([min(Z) max(Z) min(VanDerWaal) max(VanDerWaal)])
ylabel('Van der Waals argument')
xlabel('compressibility factor Z')
text(Z_gen+.1,.9,['Z = ',num2str(Z_gen)])
title(['compressibility of ',num2str(gas),' at ...
    P = ',num2str(P),' bar & T = ',num2str(K2C(T)),'  C '])
disp(['Z_generalized = ',num2str(Z_gen)])

%% produce generalized chart:
for Tr = [1 1.1 1.2 1.3 1.5 2];

for m = 1:700
Pr = .01*m;
Z = .1:.0001:1.8;

VanDerWaal = (Z + 27*Pr./(64*Tr^2*Z)).*(1 - Pr./(8*Tr*Z));
ones_vector = ones(1,length(Z));

for n = 1:length(Z);
    if VanDerWaal(n) <= 1
        Z_gen = Z(n);
    end
end

z(m) = Z_gen;
end

figure(2)
p = .01:.01:7;
plot(p,z)
hold on
axis([0 7 .1 1.1])
title('Generalized compressibility chart')
xlabel('reduced pressure, P_r')
ylabel('compressibility factor Z = PV/RT')
end

text(1.05,.36,'T_r = 1')
text(1.45,.48,'T_r = 1.1')
text(1.8,.57,'T_r = 1.2')
text(2.2,.65,'T_r = 1.3')
```

```matlab
text(2.8,.77,'T_r = 1.5')
text(3.5,.935,'T_r = 2')

%% plot air experiment region
Tr_air = C2K(22.6)/C2K(-140.5);
Pc_air = 37.71; % bar
Pairl = psi2bar(14.7);
Pairu = psi2bar(204.2);

m=0;
for Pr = (Pairl:(Pairu-Pairl)/500:Pairu)/Pc_air;
m=m+1;
pair(m) = Pr;

VanDerWaal = (Z + 27*Pr./(64*Tr_air^2*Z)).*(1 - Pr./(8*Tr_air*Z));
ones_vector = ones(1,length(Z));

for n = 1:length(Z);
    if VanDerWaal(n) <= 1
        Z_gen = Z(n);
    end
end

zair(m) = Z_gen;
end
plot(pair,zair,'r','linewidth',3)
text(.2,1.03,'air')

%% plot SF6 experiment region
Tr_sf6 = C2K(23.0)/C2K(45.6);
Pc_sf6 = 2.26; % bar
Psf6l = psi2bar(14.7);
Psf6u = psi2bar(112+14.7-4.4);

m=0;
for Pr = (Psf6l:(Psf6u-Psf6l)/500:Psf6u)/Pc_sf6;
m=m+1;
psf6(m) = Pr;

VanDerWaal = (Z + 27*Pr./(64*Tr_sf6^2*Z)).*(1 - Pr./(8*Tr_sf6*Z));
ones_vector = ones(1,length(Z));

for n = 1:length(Z);
    if VanDerWaal(n) <= 1
        Z_gen = Z(n);
```

```matlab
        end
    end

    zsf6(m) = Z_gen;
end
plot(psf6,zsf6,'m','linewidth',3)
text(1,.21,'SF_6')

%% plot ch4 experiment region
Tr_ch4 = C2K(0)/C2K(-82.7);
Pc_ch4 = 45.96; % bar
Pch4l = 10; %bar
Pch4u = 50;

m=0;
for Pr = (Pch4l:(Pch4u-Pch4l)/500:Pch4u)/Pc_ch4;
m=m+1;
pch4(m) = Pr;

VanDerWaal = (Z + 27*Pr./(64*Tr_ch4^2*Z)).*(1 - Pr./(8*Tr_ch4*Z));
ones_vector = ones(1,length(Z));

for n = 1:length(Z);
    if VanDerWaal(n) <= 1
        Z_gen = Z(n);
    end
end

zch4(m) = Z_gen;
end
plot(pch4,zch4,'g','linewidth',3)
text(.92,.89,'CH_4')
```

D.5   Lafleur & Shields Code

The following script was created by Wilson and adapted by the author [79].

```
%  Script to calculate phase speeds from L&S
%  Maps out Cphase vs. Frequency by displaying the
%  zero contour.
%
%  Good for getting a quick idea of how the system behaves.
%
%  Set C0m, the phase speeds that of interest
%  C1 = intrinsic velocity of sound in fluid (m/s)
%  Cc = compressional velocity of sound in solid (m/s)
%  Cs = shear velocity of sound in solid (m/s)
%
%  b = inner radius of cylinder (m)
%  d = outer radius of cylinder (m)
%  pl = density of liquid
%  pw = density of cylinder wall material
%
%   w = angular frequency (rad/s) - CAN BE AN ARRAY!!
%  C0m = phase velocity of axisymmetric wave in system (m/s)

clear all; close all; clc

%%  Input Parameters
C0m =  1250:5:1500;  %  Here, set sound speed range. (m/s)
fmax = 8000;  %  max frequency, forces k1*b max to 21
fmin = 500;        %  start value frequency (Hz)
N = 50;                  %  number of frequency steps

%  load material parameter file
%props_giant_sand
%props_acrylic_NRL_tap_water
%props_Port_A_PVC3
%props_Panam_City_2006
C1=ctemp(0,22.6)
pl = 998;
material_properties

%% Calculations
wf=2*pi*fmax; % final frequency
```

```matlab
w0=2*pi*fmin;  %  initial frequency

dw=(wf-w0)/(N-1);
for n=1:N
    %n
    w=(n-1)*dw + w0;
    f(n)=w/2/pi;

  sum(n,:) = LandS_eqsolvr(C0m,w,C1,Cc,Cs,b,d,pl,pw);

    if n ==1
        tic
    elseif n ==2
        t=toc;
        time_till_end_in_min = (t*N-2*t)/60
    end
end
figure(6)
set(gca, 'FontSize',14)
k1b=(f.*2.*pi).*b./C1;
contour(f,C0m,sum',[0 0],'r','linewidth',2)
hold on
ylabel('C_0_m')
xlabel('Frequency (Hz)')
toc/60;

sum=sum';
%Cphnorm=C0m./C1;
%save mapoutput f C0m sum
%save VF0p13f f -ascii
%save VF0p13com C0m -ascii
%save VF0p13sum sum -ascii
grid on
%colormap black
%title(['Phase Speed Inside Sample Holder with...
 ',num2str(C1),' m/s Lossless Fluid'])
% if Material == al
%     title('\bf Aluminum/Water L&S Solution')
% elseif Material == pvc
%     title('\bf PVC/Water L&S Solution')
% elseif Material == ss
%     title('\bf SS/Water L&S Solution')
% end
whos
```

```
makgrp = 0;
if makgrp == 1,
    [cc,h] = contour(f,C0m,sum,[0 0]);
    fff=cc(1,2:length(cc));
    w = 2*pi*fff;
    cp=cc(2,2:length(cc));
    c_g = diff(w)./diff(w./cp);
    hold,plot(fff(1:length(fff)-1),c_g,'-r',...
'linewidth',2),hold
    legend('phase velocity','group velocity',3)
end
```

D.5.1 Lafleur & Shields Material Properties

```
%  Material and Geometery Parameters for L&S calculation
%  For PVC, borosilicate, steel tubes.
%  Called from LandS_mapper to load these parameters below
%
%  C1 = intrinsic velocity of sound in fluid (m/s)
%  Cc = compressional velocity of sound in solid (m/s)
%  Cs = shear velocity of sound in solid (m/s)
%
%  b = inner radius of cylinder (m)
%  d = outer radius of cylinder (m)
%  pl = density of liquid
%  pw = density of cylinder wall material
%  p4 = density of liquid surrounding cylinder

% C1 = c_m; % from WoodsEqn.m
% C1 = c_seawater(T,Press,S)
% C1 = c_seawater(6.1,101.325,25.5);
% pl = 1025;    % (kg/m^3)

% C1=220;
% pl = 1500;

% C1 = c_seawater(24.0,101.32,35);
% pl = 1025;

% Motor oil values from Disperse
% C1 = 1740;
```

```matlab
% pl = 870;

Material = 'glass2'; %input('Al, PVC, SS, ...
glass, glass2, multicore? (lowercase)');

switch Material
    case 'al'
        v = 0.33;
        pw = 2710;
        Cc = 6294; % (m/s)
        %  input tube size parameters   (from Allen)
        b = 2.54/100; % inner radius (m)
        d = (2.54+1.27)/100; % outer radius (m)
        Cs = Cc/sqrt(2*(1-v)/(1-2*v)); % (m/s)

    case 'pvc'
        v = 0.38;
        pw = 1427.1;
        Cc = 1910.5; % (m/s)
        %  input tube size parameters
        b = in2m(2.025)/2; % inner radius (m)
        d = in2m(2.375)/2; % outer radius (m)
        Cs = Cc/sqrt(2*(1-v)/(1-2*v)); % (m/s)

    case 'ss'
        Y = 193e+9; %Young's Modulus
        v = 0.28; % estimate from efunda.com
        pw = 8000; % estimate from efunda.com
        Cc = sqrt((Y/pw)*((1-v)/((1+v)*(1-2*v)))); % (m/s)
        %  input tube size parameters   (from Allen)
%       b = 5.25/200; % inner radius (m)  ss tube
%       d = (6.03)/200; % outer radius (m)  ss tube
        b = 66.3/2000; % inner radius (m) tube 2
        d = 89/2000; % outer radius (m) tube 2
        Cs = Cc/sqrt(2*(1-v)/(1-2*v)); % (m/s)

        % Values for pressure vessel (PV).
        % Although the PV is SS316, the following are
        % props for SS304 from PSW's 2003 JASA paper.
        Cc = 5640; %
        Cs = 3070;

%       % values for 316 from
%       Cc = 5720;
%       Cs = 3272;
```

```matlab
%
%       b = in2m(5.750/2);
%       d = in2m(5.75/2+1.456-1.063);

    case 'brass'
        b = 5.25/200; % inner radius (m)
        d = (6.03)/200; % outer radius (m)
        pw = 8400;
        Cc = 4400; %CHECK THIS
        Cs = 2200; %CHECK THIS

    case 'glass' % pyrex
        b = in2m(2.131)/2;
        d = in2m(2.522)/2;
        pw = 2192.7;
        Cc = 5600;
        v = 0.24;
        Cs = Cc/sqrt(2*(1-v)/(1-2*v)); % (m/s)

    case 'glass2' % heavy-walled pyrex
        d = mm2m(69.5)/2;
        b = d-mm2m(9.3);
        pw = 2192.7;
        Cc = 5600;
        v = 0.24;
        Cs = Cc/sqrt(2*(1-v)/(1-2*v)); % (m/s)

        case 'multicore'
        v = 0.38;
        pw = 1427.1;
        Cc = 1910.5; % (m/s)
        d = mm2m(100)/2; % outer radius (m)
        b = d-mm2m(2.5); % inner radius (m)
        Cs = Cc/sqrt(2*(1-v)/(1-2*v)); % (m/s)
end
```

D.5.2 Lafleur & Shields Equation Solver Function

```matlab
% LAFLEUR AND SHIELDS EQ SOLVER
function [sum] = LandS_eqsolvr(C0m,OMEGA,C1,Cc,Cs,b,d,pl,pw)

% pass from calling script:
% C1 = intrinsic velocity of sound in fluid (m/s)
```

```matlab
%  Cc = compressional velocity of sound in solid (m/s)
%  Cs = shear velocity of sound in solid (m/s)
%  C0m = phase velocity of axisymmetric wave in system (m/s)
%  CAN BE AN ARRAY!
%
%  b = inner radius of cylinder (m)
%  d = outer radius of cylinder (m)
%  v = Ratio of Poisson for cylinder wall material
%  pl = density of test liquid
%  pw = density of cylinder wall material
%
%   OMEGA = angular frequency (rad/s): CAN BE AN ARRAY!!
%   must have function 'Lmn.m' in path

q0m = OMEGA./C0m;
kc=OMEGA./Cc;
ks=OMEGA./Cs;
k1=OMEGA./C1;

X0m=sqrt(k1.^2-q0m.^2).*b;
Pm = sqrt(kc.^2-q0m.^2);
Tm = sqrt(ks.^2-q0m.^2);
Em = q0m.^2-ks.^2/2;
Qm = (besselj(0,X0m).*b.*pl.*OMEGA.^2)./...
(besselj(1,X0m).*X0m.*Cs.^2.*pw.*2);

one = Lmn(b,d,1,1,Pm).*Lmn(b,d,0,0,Tm).*...
(q0m.^2.*Pm.^2.*Tm.^2.*pi^2.*b.*d./8./Em.^2);
two = Lmn(b,d,1,1,Tm).*Lmn(b,d,0,0,Pm).*...
(Em.^2.*b.*d.*pi^2./8./q0m.^2);
three = (Lmn(b,d,1,0,Pm).*Lmn(b,d,0,1,Tm)+...
Lmn(b,d,0,1,Pm).*Lmn(b,d,1,0,Tm)).* ...
(Pm.*Tm.*b.*d.*pi^2./8);
four=(Lmn(b,d,1,1,Pm).*Lmn(b,d,1,0,Tm).*b+...
Lmn(b,d,1,1,Pm).*Lmn(b,d,0,1,Tm).*d.*(Qm.*b+1)).* ...
(Pm.^2.*Tm.*pi^2./8./Em - Pm.^2.*q0m.^2.*Tm.*pi^2./8./Em.^2);
five=(Lmn(b,d,1,1,Tm).*Lmn(b,d,1,0,Pm).*b+...
Lmn(b,d,1,1,Tm).*Lmn(b,d,0,1,Pm).*d.*(Qm.*b+1)).* ...
(Pm.*Em.*pi^2./q0m.^2./8 - Pm.*pi^2./8);
six=Lmn(b,d,1,1,Tm).*Lmn(b,d,1,1,Pm).*...
(Qm.*b+1).*(Pm.^2.*pi^2./q0m.^2./8 + q0m.^2.*Pm.^2.*....
pi^2./Em.^2./8 - Pm.^2.*pi^2./Em./4);
sum = 1 + real(one) + real(two) + real(three) ...
+ real(four) + real(five) + real(six);
```

D.5.3 Lafleur & Shields Lmn Function

```matlab
function [out] = Lmn(b,d,m,n,y)
%  calculates Lmn from Eq. (5) in Lafleur & Shields
%  JASA 97(3), p1437
%
%    Lmn(y)=Jm(dy)Yn(by)-Jn(by)Ym(dy)
%
%%  Inputs:
%                   m = index m
%                   n = index n
%                   y = argument of function (can be array)
%                   b = inner radius of cylinder in paper
%                   d = outer radius of cylinder in paper
%
%  Outputs:
%                   out = Jm(d*arg)*Yn(b*arg)-Jn(b*arg)*Ym(d*arg)
%                   where J and Y are Bessel functions of the
%                   first and second kind, resp.

out = besselj(m,y.*d).*bessely(n,y.*b)-...
besselj(n,y.*b).*bessely(m,y.*d);
```

D.6   Bubbly Liquid Predictions and Results Plotter

Code developed to create Fig. 3.7.

```
% plot Wood's eqn for ideal vs real gas
% Chad Greene 14OC2009

close all; clear all; clc
load HurlyData.mat
%% calculate and plot theoretical c(P_inf)

SF6_press_psi = kPa2psi(interp(HurlyData(:,1),300));
c_press = interp(HurlyData(:,2),300);

ho = .348; % [m] height of water column w/o bubbles
h1 = .350; % [m] height of water column w/ bubbles
X1 = (h1-ho)/h1; % void fraction chi

nn=0;
for p_psi_g = 0:112-4;
    nn=nn+1;
    psia_plot(nn) = p_psi_g+14.7;
rho_g_0 = 6.164;
p_Pa_a(nn) = psi2Pa(p_psi_g + 14.7);
c_l = ctemp(Pa2bar(p_Pa_a(nn)),22.3);
Z1 = compressibility('SF6',C2K(22.3),psi2bar(14.7));
Z2 = compressibility('SF6',C2K(22.3),Pa2bar(p_Pa_a(nn)));
rho_l = 998;
Kl = 1./(rho_l.*c_l.^2); % compressibility of liquid
nu = 1.18;

rho_g_ideal = rho_g_0*(p_Pa_a(nn)/p_Pa_a(1));
c_g_ideal = sqrt(nu.*p_Pa_a(nn)./rho_g_ideal);
Kg_ideal = 1./(rho_g_ideal.*c_g_ideal.^2); % compressibility
c_m_ideal(nn) = 1./sqrt(((1-X1).*rho_l + ...
X1.*rho_g_ideal).*((1-X1).*Kl + X1.*Kg_ideal));

rho_g_real = rho_g_ideal*(Z1/Z2);
for mm = 1:length(SF6_press_psi)
    if  psia_plot(nn) ≤ SF6_press_psi(mm)
        c_g_real = c_press(mm);
    end
```

```matlab
end
Kg_real = 1./(Z2*rho_g_real.*c_g_real.^2); % comp. of gas
c_m_real(nn) = 1./sqrt(((1-X1).*rho_l + ...
X1.*rho_g_real).*((1-X1).*Kl + X1.*Kg_real));
end

figure(15)
set(gca, 'FontSize',16)
plot(psia_plot,c_m_ideal,'b',psia_plot,...
c_m_real,'r','linewidth',2)
% plot(psia_plot,c_m_ideal,'b','linewidth',1.5)
ylabel('low-frequency sound speed [m/s]')
xlabel('hydrostatic pressure [psia]')
legend('Wood''s model for ideal gas','Wood''s model...
 for real gas','location','southeast')
% title('sulfur hexafluoride bubbles in distilled water')
text(20,400,'sulfur hexafluoride bubbles in ...
distilled water','fontsize',16)

for tf = 25:46;
load(['data_from_x091012_',num2str(tf),'.mat'])
press = Pgage_psi - 3.9;

n = 1:length(freqs); % <-- Use this as default....
%  Edit if necessary, say for skipping structural resonances
[M,N] = polyfit(n,freqs',1);
c2 = M(1)*2*h1;

hold on
plot(press+14.7,c2,'k*','markersize',8)
end
text(13,210,'VF = 0.57%','fontsize',14)

%% plot another void fraction
clear psia_plot press c_m_real c_m_ideal Kg_ideal ...
Kg_real rho_g_ideal rho_g_ideal nn mm Z1 Z2 n c c2
h2 = .352; % [m] height of water column w/ bubbles
X2 = (h2-ho)/h2; % void fraction chi

nn=0;
for p_psi_g = 0:110;
   nn=nn+1;
   psia_plot(nn) = p_psi_g+14.7;
p_Pa_a(nn) = psi2Pa(p_psi_g + 14.7);
c_l = ctemp(Pa2bar(p_Pa_a(nn)),22.3);
```

```matlab
Z1 = compressibility('SF6',C2K(22.3),psi2bar(14.7));
Z2 = compressibility('SF6',C2K(22.3),Pa2bar(p_Pa_a(nn)));

rho_g_ideal = rho_g_0*(p_Pa_a(nn)/p_Pa_a(1));
c_g_ideal = sqrt(nu.*p_Pa_a(nn)./rho_g_ideal);
Kg_ideal = 1./(rho_g_ideal.*c_g_ideal.^2); % comp of gas
c_m_ideal(nn) = 1./sqrt(((1-X2).*rho_l + ...
X2.*rho_g_ideal).*((1-X2).*Kl + X2.*Kg_ideal));

rho_g_real = rho_g_0*(p_Pa_a(nn)/p_Pa_a(1))*(Z1/Z2);
for mm = 1:length(SF6_press_psi)
    if  psia_plot(nn) <= SF6_press_psi(mm)
        c_g_real = c_press(mm);
    end
end
Kg_real = 1./(Z2*rho_g_real.*c_g_real.^2); % comp. of gas
c_m_real(nn) = 1./sqrt(((1-X2).*rho_l +...
 X2.*rho_g_real).*((1-X2).*Kl + X2.*Kg_real));
end

plot(psia_plot(53:111),c_m_ideal(53:111),'b',...
psia_plot(53:111),c_m_real(53:111),'r','linewidth',2)
% plot(psia_plot(53:111),c_m_ideal(53:111),...
'b','linewidth',1.5)

for tf = 13:23;
load(['data_from_x091012_',num2str(tf),'.mat'])
press = Pgage_psi - 3.9;

n = 1:length(freqs); % <-- Use this as default...
% Edit if necessary, say for skipping structural resonances
[M,N] = polyfit(n,freqs',1);
c2 = M(1)*2*h2;

plot(press+14.7,c2,'ko','markersize',8)
end
text(88,195,'VF = 1.14%','fontsize',14)
axis([0 140 95 450])
box off
```

D.7 Hydrate Mixture Sound Speed Plotter

Code developed to create Fig. 4.4.

```matlab
% Plot Hydrates Sound Speeds
% Chad Greene 26JAN2010
% Plot sound speeds of multiple hydrate samples as...
% a function of hydrostatic pressure
close all; clear all; clc

load Bag2
for n=4:18
    nn=n-1;
    load(['data_from_X100120_',num2str(n),'.mat'])
    P_atm_Bag2(n-3) = psi2atm(Bag2(nn,1)+11.7);
    c_Bag2(n-3) = c;
end

for n=19:56
    nn=n-1;
    load(['data_from_X100120_',num2str(n),'.mat'])
    P_atm_Bag2b(n-18) = psi2atm(Bag2(nn,1)+11.7);
    c_Bag2b(n-18) = c;
end

load Bag3
for n=24:49
    nn=n-23;
    load(['data_from_X100121_',num2str(n),'.mat'])
    P_atm_Bag3(nn) = psi2atm(Bag3(nn,1)+11.7);
    c_Bag3(nn) = c;
end

load Bag4
for n=3:21
    nn=n-2;
    load(['data_from_X100121_',num2str(n),'.mat'])
    P_atm_Bag4(nn) = psi2atm(Bag4(nn,1)+11.7);
    c_Bag4(nn) = c;
end

load Bag5
```

```
for n=53:92
    nn=n-52;
    load(['data_from_X100121_',num2str(n),'.mat'])
    P_atm_Bag5(nn) = psi2atm(Bag5(nn,1)+11.7);
    c_Bag5(nn) = c;
end

figure(2)
set(gca, 'FontSize',16)
plot(P_atm_Bag2b,c_Bag2b,'g*',P_atm_Bag3,c_Bag3,'ro',...
P_atm_Bag4,c_Bag4,'b+',P_atm_Bag5,c_Bag5,'kp',...
'markersize',10,'linewidth',2)
xlabel('hydrostatic pressure [atm]')
ylabel('c_m [m/s]')
% title('low-frequency sound speed of mixture')
legend('sI Cascadia Margin','sII Cascadia Margin',...
'sI Haakon Mosby','sII Gulf of Mexico','location','southeast')
box off
```

D.8 Sample Sound Speed Solver

```matlab
% Solve sound speeds of samples from pressure vessel
%% Enter constants
L2 = .429;
tracefile = 'X100208_2';
sig = importdata([num2str(tracefile),'.asc']);

approxpeaks = 100.*[15 29];% 44 59]; % approx...
% frequencies of resonances [Hz]
tolerance = 300; % look for peaks at 'approxpeaks'...
% locations plus or minus tolerance [Hz].

%% plot spectrum
sig = sig(1:max(find(sig(:,1))),:);% eliminates undesired spectra
freq = sig(:,1);
P_raw = sig(:,2);
P = smooth(P_raw,1);
% P = P_raw;

figure(1),subplot(2,1,1)
plot(freq,P_raw,'k:','linewidth',.5)
hold on
plot(freq,P,'b','linewidth',1.5)
xlabel('frequency (Hz)')
ylabel('amplitude (dB)')
% legend('raw data','smoothed data')
title(['rubber ball pressure test'])

%% Peak finder
ii = 1;
for nn = 1:length(freq)
    for mm = 1:length(approxpeaks)
        if freq(nn) > approxpeaks(mm)-tolerance...
    && freq(nn) < approxpeaks(mm)+tolerance
            prange(mm,ii) = P(nn);
            ii = ii+1;
        end
    end
end

for mm=1:length(approxpeaks)
     peaks(mm,1) = max(nonzeros(prange(mm,:)));
```

```matlab
    end

for ii = 1:length(freq)
    for mm = 1:length(approxpeaks)
        if P(ii) == peaks(mm,1)
            freqs(mm,1) = freq(ii);
        end
    end
end

subplot(2,1,1)
hold on
plot(freqs,peaks,'ro','linewidth',1.5)
xlim([min(freq) max(freq)])

%% plot slopes

subplot(2,1,2)
n = 1:length(peaks); % <-- Use this as default...
% Edit if necessary, say for skipping structural resonances
plot(n,freqs,'ro')
xlim([0,max(n)+1])
c_ph = 4*L2.*freqs'./(2.*n-1);  %  calculates the phase...
% speed given integer multiples of 1/2 lambda at each res_freq

[M,N] = polyfit(n,freqs',1);

display(['Norm of residuals = ',num2str(N.normr)])

hold on
plot(n,M(1).*n + M(2),'k')
xlabel('mode number')
ylabel('resonance frequencies (Hz)')
legend('resonance frequencies',['best linear fit N = ',...
num2str(N.normr)],4) % N is the norm of residuals

c = M(1)*2*L2;
text(.5,.75*max(freqs),['Best fit slope yields c_{eff} = ',...
num2str(c),' m/s'])
hold off
disp(['c_eff = ',num2str(c),' m/s'])
save(['data_from_',num2str(tracefile),'.mat'],'c','freqs')
```

D.9 Rubber Ball Data Plotter

```matlab
% rubber ball in PV data
% Chad Greene 09FEB2010
close all; clear all; clc

%% plot all spectra
load rubber_balls
figure(1)
subplot(2,1,1)
hold on
n=0;
for tracefile = 9:27
sig = importdata(['X100208_',num2str(tracefile),'.asc']);
n=n+1;
P_psig = rubber_balls(n,1)-3;

freq = sig(:,1);
P_raw = sig(:,2);
imagesc(freq,P_psig,P_raw')

end
title('Rubber Ball Data')
xlabel('frequency [Hz]')
ylabel('pressure [psig]')
axis([min(freq) max(freq) min(rubber_balls(:,1))-5...
max(rubber_balls(:,1))+1])

%% plot c(p)
clc
for n=9:27;
    nn=n-8;
    load(['data_from_X100208_',num2str(n),'.mat'])
    P_atm_balls(nn) = psi2atm(rubber_balls(nn,1)+11.7);
    c_balls(nn) = c;
end

subplot(2,1,2)
plot(P_atm_balls,c_balls,'k*')
xlabel('pressure [atm]')
ylabel('c_m [m/s]')
title('low-frequency sound speed of mixture')
xlim([0 max(P_atm_balls)+1])
```

121

D.10 Bulk Modulus and Sound Speed Calculator

```
% Bulk Modulus & Sound Speed Calculator
% Calculates (approx) bulk modulus of a sample in liquid.
% Uses two-phase Wood's model
% Chad Greene 08NOV2010
close all; clear all; clc

%% Enter parameters
L = .446; % height [m]
b = .026; % inner radius [m]
c_m = 1556; % sound speed of mixture [m/s]
rho_l = 998; % density of liquid [kg/m^3]
c_l = 1489; % sound speed of liquid [m/s]
rho_samp = 1402; % density of sample kg/m^3

%% Calculation
c_m_obs = c_m;
kappa_l = 1/(rho_l*c_l^2);
Vtot = pi*b^2*L;
Vsamp = 4*(4/3)*pi*(in2m(.975/2))^3;
VF = Vsamp/Vtot; % void fraction

c_samp=.1:.01:1500;
kappa_samp = (rho_samp.*c_samp.^2).^(-1);
c_m = ((VF.*kappa_samp + (1-VF)*kappa_l)...
 *(VF*rho_samp + (1-VF)*rho_l)).^(-.5);
c_samp_meas = interp1(c_samp,c_m,c_m_obs)
B_samp = rho_samp*(c_samp_meas)^2 %bulk mod
```

Bibliography

[1] Intergovernmental Panel on Climate Change. Climate change 2007: The Physical Science Basis. *Summary for Policymakers. Intergovernmental Panel on Climate Change: Geneva*, 4:1, 2007.

[2] L.C. Smith, G.M. MacDonald, A.A. Velichko, D.W. Beilman, O.K. Borisova, K.E. Frey, K.V. Kremenetski, and Y. Sheng. Siberian peatlands a net carbon sink and global methane source since the early Holocene. *Science*, 303:353, 2004.

[3] K.M. Walter, S.A. Zimov, J.P. Chanton, D. Verbyla, and F.S. Chapin III. Methane bubbling from Siberian thaw lakes as a positive feedback to climate warming. *Nature*, 443:71, 2006.

[4] I. Fung, J. John, J. Lerner, E. Matthews, M. Prather, L.P. Steele, and P.J. Fraser. Three-dimensional model synthesis of the global methane cycle. *Journal of Geophysical Research*, 96:13033, 1991.

[5] K.A. Kvenvolden. Gas hydrates—geological perspective and global change. *Reviews of Geophysics*, 31:173, 1993.

[6] K.M. Walter, J.P. Chanton, F.S. Chapin III, E.A.G. Schuur, and S.A. Zimov. Methane production and bubble emissions from arctic lakes: Iso-

topic implications for source pathways and ages. *Journal of Geophysical Research*, 113:G00A08, 2008.

[7] C.S. Law, S.D. Nodder, J. Mountjoy, A. Marriner, A. Orpin, C.A. Pilditch, P. Franz, and K. Thompson. Geological, hydrodynamic and biogeochemical variability of a New Zealand deep-water methane cold seep during an integrated three-year time-series study. *Marine Geology*, 272:189, 2009.

[8] D.I. Sebacher, R.C. Harriss, K.B. Bartlett, S.M. Sebacher, and S.S. Grice. Atmospheric methane sources: Alaskan tundra bogs, an alpine fen, and a subarctic boreal marsh. *Tellus Series B*, 38:1, 2010.

[9] E.D. Sloan Jr. Physical/chemical properties of gas hydrates and application to world margin stability and climatic change. *Geological Society London Special Publications*, 137:31, 1998.

[10] A.V. Milkov. Global estimates of hydrate-bound gas in marine sediments: How much is really out there? *Earth-Science Reviews*, 66:183, 2004.

[11] J.B. Klauda and S.I. Sandler. Global distribution of methane hydrate in ocean sediment. *Energy Fuels*, 19:459, 2005.

[12] V. Gornitz and I. Fung. Potential distribution of methane hydrates in the world's oceans. *Global Biogeochemical Cycles*, 8:335, 1994.

[13] K.A. Kvenvolden and B.W. Rogers. Gaia's breath–global methane exhalations. *Marine and Petroleum Geology*, 22:579, 2005.

[14] G.R. Dickens. Rethinking the global carbon cycle with a large, dynamic and microbially mediated gas hydrate capacitor. *Earth and Planetary Science Letters*, 213:169, 2003.

[15] E.A. Schuur. The relative contribution of methane and carbon dioxide release to climate change as a result of the decomposition of permafrost carbon (Invited). In *AGU Fall Meeting Abstracts*, page 3, 2009.

[16] T.R. Christensen, A. Ekberg, L. Ström, M. Mastepanov, N. Panikov, M. Öquist, B.H.Svensson, H. Nykänen, P.J. Martikainen, and H. Oskarsson. Factors controlling large scale variations in methane emissions from wetlands. *Geophysical Research Letters*, 30:1414, 2003.

[17] G.R. Dickens, J.R. O'Neil, D.K. Rea, and R.M. Owen. Dissociation of oceanic methane hydrate as a cause of the carbon isotope excursion at the end of the Paleocene. *Paleoceanography*, 10:965, 1995.

[18] J.P. Kennett. *Methane Hydrates in Quaternary Climate Change: The Clathrate Gun Hypothesis*. American Geophysical Union, 2003.

[19] S.J. Hassol and A.C.I. Assessment. *Impacts of a warming Arctic: Arctic climate impact assessment*. Cambridge University Press, New York, 2004.

[20] K.A. Kvenvolden. Methane hydrate–A major reservoir of carbon in the shallow geosphere? *Chemical Geology*, 71:41, 1988.

[21] O. Reynolds. *Papers on mechanical and physical subjects*. University Press, 1901.

[22] J.W.S. Rayleigh. On the pressure developed in a liquid during the collapse of a spherical cavity. *Philosophical Magazine*, XXXIV:94, 1917.

[23] M.S. Plesset. The dynamics of cavitation bubbles. *Journal of Applied Mechanics*, 16:227, 1949.

[24] D.F. Gaitan, L.A. Crum, C.C. Church, and R.A. Roy. Sonoluminescence and bubble dynamics for a single, stable, cavitation bubble. *The Journal of the Acoustical Society of America*, 91:3166, 1992.

[25] V.O. Knudsen, R.S. Alford, and J.W. Emling. Underwater ambient noise. *Journal of Marine Research*, 7:410, 1948.

[26] D. Betteridge, M.T. Joslin, and T. Lilley. Acoustic emissions from chemical reactions. *Analytical Chemistry*, 53:1064, 1981.

[27] J.W.R. Boyd and J. Varley. The uses of passive measurement of acoustic emissions from chemical engineering processes. *Chemical Engineering Science*, 56:1749, 2001.

[28] R. Manasseh, R.F. LaFontaine, J. Davy, I. Shepherd, and Y.G. Zhu. Passive acoustic bubble sizing in sparged systems. *Experiments in Fluids*, 30:672, 2001.

[29] C.A. Greene and P.S. Wilson. Toward passive acoustic remote sensing of ocean-bottom gas seeps (A). *The Journal of the Acoustical Society of America*, 127:1938, 2010.

[30] T.G. Leighton and A.J. Walton. An experimental study of the sound emitted from gas bubbles in a liquid. *European Journal of Physics*, 8:98, 1987.

[31] I. Leifer and D. Tang. The acoustic signature of marine seep bubbles. *The Journal of the Acoustical Society of America*, 121:EL35, 2007.

[32] M.S. Longuet-Higgins, B.R. Kerman, and K. Lunde. The release of air bubbles from an underwater nozzle. *Journal of Fluid Mechanics*, 230:365, 1991.

[33] M. Minnaert. On Musical Air-Bubbles and the Sounds of Running Water. *Philosophical Magazine Series 7*, 16:235, 1933.

[34] T.G. Leighton. *The Acoustic Bubble*. Academic Press, London, 1994.

[35] A. Prosperetti. The thermal behaviour of oscillating gas bubbles. *Journal of Fluid Mechanics*, 222:587, 1991.

[36] M.S. Plesset and A. Prosperetti. Bubble dynamics and cavitation. *Annual Review of Fluid Mechanics*, 9:145, 1977.

[37] M. Strasberg. The pulsation frequency of nonspherical gas bubbles in liquids. *The Journal of the Acoustical Society of America*, 25:536, 1953.

[38] M.R. Loewen and W.K. Melville. A model for the sound generated by breaking waves. *The Journal of the Acoustical Society of America*, 90:2075, 1991.

[39] T.G. Leighton, D.G. Ramble, and A.D. Phelps. The detection of tethered and rising bubbles using multiple acoustic techniques. *The Journal of the Acoustical Society of America*, 101:2626, 1997.

[40] M.S. Longuet-Higgins. Monopole emission of sound by asymmetric bubble oscillations. Part 1. Normal modes. *Journal of Fluid Mechanics*, 201:525, 1989.

[41] M.S. Longuet-Higgins. Monopole emission of sound by asymmetric bubble oscillations. Part 2. An initial-value problem. *Journal of Fluid Mechanics*, 201:543, 1989.

[42] H. Lamb. *Hydrodynamics*. Dover Publications, New York, 1932.

[43] M. Strasberg. Gas bubbles as sources of sound in liquids. *The Journal of the Acoustical Society of America*, 28:20, 1956.

[44] H.D. Hedberg. Relation of methane generation to undercompacted shales, shale diapirs, and mud volcanoes. *American Association of Petroleum Geologists*, 58:661, 1974.

[45] L.I. Dimitrov. Mud volcanoes–the most important pathway for degassing deeply buried sediments. *Earth-Science Reviews*, 59:49, 2002.

128

[46] G. Etiope, A. Caracausi, R. Favara, F. Italiano, and C. Baciu. Methane emission from the mud volcanoes of Sicily (Italy). *Geophysical Research Letters*, 29:1215, 2002.

[47] H. Niemann, T. Lösekann, D. De Beer, M. Elvert, T. Nadalig, K. Knittel, R. Amann, E.J. Sauter, M. Schlüter, M. Klages, et al. Novel microbial communities of the Haakon Mosby mud volcano and their role as a methane sink. *Nature*, 443:854, 2006.

[48] A. Mallock. The damping of sound by frothy liquids. *Proceedings of the Royal Society of London*, 84:391, 1910.

[49] D.A. Wilson and L.N. Liebermann. Attenuation of Sound in Water. *The Journal of the Acoustical Society of America*, 19:286, 1947.

[50] E.L. Carstensen and L.L. Foldy. Propagation of sound through a liquid containing bubbles. *The Journal of the Acoustical Society of America*, 19:481, 1947.

[51] N. Davids and E.G. Thurston. The acoustical impedance of a bubbly mixture and its size distribution function. *The Journal of the Acoustical Society of America*, 22:20, 1950.

[52] E. Silberman. Sound velocity and attenuation in bubbly mixtures measured in standing wave tubes. *The Journal of the Acoustical Society of America*, 29:925, 1957.

[53] H.B. Karplus. Velocity of Sound in a Liquid Containing Gas Bubbles. *The Journal of the Acoustical Society of America*, 29:1261, 1957.

[54] A.L. Anderson and L.D. Hampton. Acoustics of gas-bearing sediments I. Background. *The Journal of the Acoustical Society of America*, 67:1865, 1980.

[55] A.B. Wood. *A Textbook of Sound: Being an Account of the Physics of Vibrations with Special Reference to Recent Theoretical and Technical Developments*. MacMillan, New York, 1930.

[56] H. Medwin. In situ acoustic measurements of bubble populations in coastal ocean waters. *Journal of Geophysical Research*, 75:599, 1970.

[57] S. Vagle and D.M. Farmer. The measurement of bubble-size distributions by acoustical backscatter. *Journal of Atmospheric and Oceanic Technology*, 9:630, 1992.

[58] B.S. McCartney and B.M.K. Bary. Echo-sounding on probable gas bubbles from the bottom of Saanich Inlet, British Columbia. In *Deep Sea Research and Oceanographic Abstracts*, volume 12, pages 285–286. Elsevier, 1965.

[59] H. Medwin. Acoustical determinations of bubble-size spectra. *The Journal of the Acoustical Society of America*, 62:1041, 1977.

[60] D.R. Jackson, K.L. Williams, T.F. Wever, C.T. Friedrichs, and L.D. Wright. Sonar evidence for methane ebullition in Eckernförde Bay. *Continental Shelf Research*, 18:1893, 1998.

[61] I. Leifer, R.K. Patro, and P. Bowyer. A study on the temperature variation of rise velocity for large clean bubbles. *Journal of Atmospheric and Oceanic Technology*, 17:1392, 2000.

[62] S.M. DeBeukelaer, I.R. MacDonald, N.L. Guinnasso, and J.A. Murray. Distinct side-scan sonar, RADARSAT SAR, and acoustic profiler signatures of gas and oil seeps on the Gulf of Mexico slope. *Geo-Marine Letters*, 23:177, 2003.

[63] E.J. Sauter, A. Boetius, M. Schluumlter, E. Damm, and M. Klages. Acoustic detection of methane plumes. *Energy, Exploration & Exploitation*, 21:299, 2003.

[64] C. Aoyama, R. Matsumoto, A. Hiruta, M. Sunamura, H. Tomaru, J. Komatsubara, and M. Hiromatsu. Acoustical Surveys of Methane Plumes by Using the Quantitative Echo Sounder in the Sea of Japan. In *Symposium on Underwater Technology and Workshop on Scientific Use of Submarine Cables and Related Technologies, 2007*, page 249, 2007.

[65] H. Duarte, L. Menezes Pinheiro, F. Curado Teixeira, and J.H. Monteiro. High-resolution seismic imaging of gas accumulations and seepage in the sediments of the Ria de Aveiro barrier lagoon (Portugal). *Geo-Marine Letters*, 27:115, 2007.

131

[66] I. Ostrovsky, D.F. McGinnis, L. Lapidus, and W. Eckert. Quantifying gas ebullition with echosounder: the role of methane transport by bubbles in a medium-sized lake. *Limnology and Oceanography: Methods*, 6:105, 2008.

[67] B.R. Kerman, editor. *Sea surface sound: natural mechanisms of surface generated noise in the ocean.* Springer, New York, 1988.

[68] S.W. Yoon, L.A. Crum, A. Prosperetti, and N.Q. Lu. An investigation of the collective oscillations of a bubble cloud. *The Journal of the Acoustical Society of America*, 89:700, 1991.

[69] A. Prosperetti, N.Q. Lu, and H.S. Kim. Active and passive acoustic behavior of bubble clouds at the oceans surface. *The Journal of the Acoustical Society of America*, 93:3117, 1993.

[70] M. Nicholas, R.A. Roy, L.A. Crum, H. Oguz, and A. Prosperetti. Sound emissions by a laboratory bubble cloud. *The Journal of the Acoustical Society of America*, 95:3171, 1994.

[71] S.L. Means. Low-frequency sound generation from breaking surf. *Acoustics Research Letters Online*, 5:13, 2004.

[72] S.W. Kieffer. Sound speed in liquid-gas mixtures: water-air and water-steam. *Journal of Geophysical Research*, 82:2895, 1977.

[73] J.E. White. Elastic dilatancy, fluid saturation, and earthquake dynamics. *Geophysical Research Letters*, 3:747, 1976.

[74] P.W. Bridgman. The compressibility of five gases to high pressures. In *Proceedings of the American Academy of Arts and Sciences*, volume 59, page 173, 1924.

[75] F.G. Keyes and H.G. Burks. The isometrics of gaseous methane. *Journal of the American Chemical Society*, 49:1403, 1927.

[76] H.M. Kvalnes and V.L. Gaddy. The compressibility isotherms of methane at pressures to 1000 atmospheres and at temperatures from -70 to 200°. *Journal of the American Chemical Society*, 53:394, 1931.

[77] P.M. Dranchuk and J.H. Abou-Kassem. Calculation of Z factors for natural gases using equations of state. *Journal of Canadian Petroleum Technology*, 14:34, 1975.

[78] C.A. Greene and P.S. Wilson. Measurements of sound speed in bubbly liquids under high-pressure conditions (A). *The Journal of the Acoustical Society of America*, 126:2194, 2009.

[79] P.S. Wilson. *Sound Propagation and Scattering in Bubbly Liquids*. PhD thesis, Boston University, 2002.

[80] K.W. Commander and A. Prosperetti. Linear pressure waves in bubbly liquids: Comparison between theory and experiments. *The Journal of the Acoustical Society of America*, 85:732, 1989.

[81] S.G. Kargl. Effective medium approach to linear acoustics in bubbly liquids. *The Journal of the Acoustical Society of America*, 111:168, 2002.

[82] J.D. van der Waals. The equation of state for gases and liquids. *Nobel Lectures in Physics*, 1:254, 1910.

[83] B. Clapeyron. Mémoire sur la puissance motrice de la chaleur. *Journal de l'École Polytechnique*, XIV:153, 1834.

[84] J.D. van der Waals. *Over de Constinuiteid van der gas-en Vlocistoftoestand.* PhD thesis, University of Leiden, 1873.

[85] Y.V.C. Rao. *Chemical Engineering Thermodynamics.* Orient Blackswan, Hyderabad, 1997.

[86] R.K. Bansal. *A Textbook of Fluid Mechanics.* Laxmi Publications, Boston, 2005.

[87] J.D. Anderson. *Modern Compressible Flow: with Historical Perspective.* McGraw-Hill, New York, 3rd edition, 2004.

[88] Y.A. Çengel, J.M. Cimbala, and M. Kanoglu. *Fluid Mechanics: Fundamentals and Applications.* McGraw-Hill, New York, 2006.

[89] P.S. Wilson. Low-frequency dispersion in bubbly liquids. *Acoustics Research Letters Online*, 6:188, 2005.

[90] L.E. Kinsler, A.R. Frey, A.B. Coppens, and J.V. Sanders. *Fundamentals of Acoustics.* John Wiley & Sons Inc., New York, 1982.

[91] P.S. Wilson and K.H. Dunton. Laboratory investigation of the acoustic response of seagrass tissue in the frequency band 0.5–2.5 kHz. *The Journal of the Acoustical Society of America*, 125:1951, 2009.

[92] D.T. Blackstock. *Fundamentals of Physical Acoustics.* Wiley-Interscience, New York, 2000.

[93] P.S. Wilson and R.A. Roy. An audible demonstration of the speed of sound in bubbly liquids. *American Journal of Physics*, 76:975, 2008.

[94] W.J. Jacobi. Propagation of sound waves along liquid cylinders. *The Journal of the Acoustical Society of America*, 21:120, 1949.

[95] P.S. Wilson, R.A. Roy, and W.M. Carey. An improved water-filled impedance tube. *The Journal of the Acoustical Society of America*, 113:3245, 2003.

[96] L.D. Lafleur and F.D. Shields. Low-frequency propagation modes in a liquid-filled elastic tube waveguide. *The Journal of the Acoustical Society of America*, 97:1435, 1995.

[97] V.A. Del Grosso and R.E. McGill. Remarks on axially symmetric vibrations of a thin cylindrical elastic shell filled with non viscous compressible fluid. *Acústica*, 20:313, 1968.

[98] V.A. Del Grosso. Analysis of multimode acoustic propagation in liquid cylinders with realistic boundary conditions—Application to sound speed and absorption measurements. *Acústica*, 24:299, 1971.

[99] T.C. Lin and G.W. Morgan. Wave propagation through fluid contained in a cylindrical, elastic shell. *The Journal of the Acoustical Society of America*, 28:1165, 1956.

[100] J.J. Hurly, D.R. Defibaugh, and M.R. Moldover. Thermodynamic properties of sulfur hexafluoride. *International Journal of Thermophysics*, 21:739, 2000.

[101] K.A. Kvenvolden. Potential effects of gas hydrate on human welfare. *Proceedings of the National Academy of Sciences*, 96:3420, 1999.

[102] H.M. Powell. The structure of molecular compounds; clathrate compounds. *Journal of the Chemical Society*, 16:61, 1948.

[103] E.D. Sloan and C.A. Koh. *Clathrate Hydrates of Natural Gases*. Marcel Dekker, Inc., New York, 2008.

[104] R. Sassen and I.R. MacDonald. Evidence of structure H hydrate, Gulf of Mexico continental slope. *Organic Geochemistry*, 22:1029, 1994.

[105] H. Davy. The Bakerian Lecture: On Some of the Combinations of Oxymuriatic Gas and Oxygene, and on the Chemical Relations of These Principles, to Inflammable Bodies. *Philosophical Transactions of the Royal Society of London*, 101:1, 1811.

[106] W.L. Mao, C.A. Koh, and E.D. Sloan. Clathrate hydrates under pressure. *Physics Today*, 60:42, 2007.

[107] S.Y. Lee and G.D. Holder. Methane hydrates potential as a future energy source. *Fuel Processing Technology*, 71:181, 2001.

[108] W. Xu, R.P. Lowell, and E.T. Peltzer. Effect of seafloor temperature and pressure variations on methane flux from a gas hydrate layer- Comparison between current and late Paleocene climate conditions. *Journal of Geophysical Research*, 106:26413, 2001.

[109] G.J. Moridis. Numerical studies of gas production from methane hydrates. *Society of Petroleum Engineers Journal*, 8:359, 2003.

[110] D.J. Thomas, J.C. Zachos, T.J. Bralower, E. Thomas, and S. Bohaty. Warming the fuel for the fire: Evidence for the thermal dissociation of methane hydrate during the Paleocene-Eocene thermal maximum. *Geology*, 30:1067, 2002.

[111] K. Walter Anthony. Methane: A Menace Surfaces. *Scientific American*, 301:44, 2009.

[112] E.G. Hammerschmidt. Formation of gas hydrates in natural gas transmission lines. *Industrial & Engineering Chemistry*, 26:851, 1934.

[113] J.W. Barker and R.K. Gomez. Formation of hydrates during deepwater drilling operations. *Journal of Petroleum Technology*, 41:297, 1989.

[114] R. Camilli, C.M. Reddy, D.R. Yoerger, B.A.S. Van Mooy, M.V. Jakuba, J.C. Kinsey, C.P. McIntyre, S.P. Sylva, and J.V. Maloney. Tracking Hydrocarbon Plume Transport and Biodegradation at Deepwater Horizon. *Sciencexpress*, page 1, 2010.

[115] J. Achenbach and M.P. Flaherty. Sealing cap placed on oil well as Interior Department issues ban on offshore drilling. *The Washington Post*, July 13, 2010.

[116] M.K. MacLeod. Gas hydrates in ocean bottom sediments. *American Association of Petroleum Geologists Bulletin*, 66:2649, 1982.

[117] I.A. Pecher, T.A. Minshull, S.C. Singh, and R. Huene. Velocity structure of a bottom simulating reflector offshore Peru: Results from full waveform inversion. *Earth and Planetary Science Letters*, 139:459, 1996.

[118] R. von Huene and I.A. Pecher. Vertical tectonics and the origins of BSRs along the Peru margin. *Earth and Planetary Science Letters*, 166:47, 1999.

[119] I.A. Pecher, N. Kukowski, C. Huebscher, J. Greinert, and J. Bialas. The link between bottom-simulating reflections and methane flux into the gas hydrate stability zone-new evidence from Lima Basin, Peru Margin. *Earth and Planetary Science Letters*, 185:343, 2001.

[120] W.T. Wood, P.L. Stoffa, and T.H. Shipley. Quantitative detection of methane hydrate through high-resolution seismic velocity analysis.

Journal of Geophysical Research, 99:9681, 1994.

[121] M.J. Hornbach, W.S. Holbrook, A.R. Gorman, K.L. Hackwith, D. Lizarralde, and I. Pecher. Direct seismic detection of methane hydrate on the Blake Ridge. *Geophysics*, 68:92, 2003.

[122] M.E. Weber, F. Niessen, G. Kuhn, and M. Wiedicke. Calibration and application of marine sedimentary physical properties using a multi-sensor core logger. *Marine Geology*, 136:151, 1997.

[123] D.E. Gunn and A.I. Best. A new automated nondestructive system for high resolution multi-sensor core logging of open sediment cores. *Geo-Marine Letters*, 18:70, 1998.

[124] S.N. Domenico. Elastic properties of unconsolidated porous sand reservoirs. *Geophysics*, 42:1339, 1977.

[125] A.L. Anderson and L.D. Hampton. Acoustics of gas-bearing sediments. II. Measurements and models. *The Journal of the Acoustical Society of America*, 67:1890, 1980.

[126] K.U. Heeschen, A.M. Tréhu, R.W. Collier, E. Suess, and G. Rehder. Distribution and height of methane bubble plumes on the Cascadia Margin characterized by acoustic imaging. *Geophysical Research Letters*, 30:1643, 2003.

[127] E.J. Sauter, S.I. Muyakshin, J.L. Charlou, M. Schlüter, A. Boetius, K. Jerosch, E. Damm, J.P. Foucher, and M. Klages. Methane discharge

from a deep-sea submarine mud volcano into the upper water column by gas hydrate-coated methane bubbles. *Earth and Planetary Science Letters*, 243:354, 2006.

[128] G. Rehder, P.W. Brewer, E.T. Peltzer, and G. Friederich. Enhanced lifetime of methane bubble streams within the deep ocean. *Geophysical Research Letters*, 29:21, 2002.

[129] C.J. Wilson, P.S. Wilson, C.A. Greene, and K.H. Dunton. Seagrass leaves in 3-D: Using computed tomography and low-frequency acoustics to investigate the material properties of seagrass tissue. *Journal of Experimental Marine Biology and Ecology*, 395:128, 2010.

[130] W.R. Parrish and J.M. Prausnitz. Dissociation pressures of gas hydrates formed by gas mixtures. *Industrial & Engineering Chemistry Process Design and Development*, 11:26, 1972.

[131] J.H. van der Waals and J.C. Platteeuw. Clathrate solutions. *Advances in Chemical Physics*, 2:1, 1959.

[132] G.R. Dickens and M.S. Quinby-Hunt. Methane hydrate stability in seawater. *Geophysical Research Letters*, 21:2115, 1994.

[133] E.T. Peltzer and P.G. Brewer. *Natural Gas Hydrate in Oceanic and Permafrost Environments*. Kluwer Academic Publishers, New York, 2000.

[134] P.S. Wilson, A.H. Reed, W.T. Wood, and R.A. Roy. The low-frequency sound speed of fluid-like gas-bearing sediments. *The Journal of the Acoustical Society of America: Express Letters*, 123, 2008.

[135] N.D. Richardson, K.L. Williams, K.B. Briggs, and E.I. Thorsos. Dynamic measurement of sediment grain compressibility at atmospheric pressure: acoustic applications. *IEEE Journal of Oceanic Engineering*, 27:593, 2002.

[136] W.K. Moonan and N.W. Tschoegl. Effect of pressure on the mechanical properties of polymers. 2. Expansivity and compressibility measurements. *Macromolecules*, 16:55, 1983.

[137] L.A. Wood and G.M. Martin. Compressibility of natural rubber at pressures below 500 kg/cm^2. *Journal of Research National Bureau of Standards*.

[138] M.W. Lee, D.R. Hutchinson, T.S. Collett, and W.P. Dillon. Seismic velocities for hydrate-bearing sediments using weighted equation. *Journal of Geophysical Research*, 101:20347, 1996.

[139] M.B. Helgerud, J. Dvorkin, A. Nur, A. Sakai, and T. Collett. Elastic-wave velocity in marine sediments with gas hydrates: Effective medium modeling. *Geophysical Research Letters*, 26:2021, 1999.

[140] W.F. Waite, M.B. Helgerud, A. Nur, J.C. Pinkston, L.A. Stern, S.H. Kirby, and W.B. Durham. Laboratory measurements of compressional

and shear wave speeds through methane hydrate. *Annals of the New York Academy of Sciences*, 912:1003, 2000.

[141] B.I. Pandit and M.S. King. Elastic wave propagation in propane gas hydrates. In *Proceedings of the 4th Canadian Permafrost Conference*, pages 335–342, 1982.

[142] D. Gei and J.M. Carcione. Acoustic properties of sediments saturated with gas hydrate, free gas and water. *Geophysical Prospecting*, 51:141, 2003.

[143] J.A. Priest, A.I. Best, and C.R.I. Clayton. A laboratory investigation into the seismic velocities of methane gas hydrate-bearing sand. *Journal of Geophysical Research*, 110:B04102, 2005.

[144] H. Lu, Y. Seo, J. Lee, I. Moudrakovski, J.A. Ripmeester, N.R. Chapman, R.B. Coffin, G. Gardner, and J. Pohlman. Complex gas hydrate from the Cascadia margin. *Nature*, 445:303, 2007.

[145] W.H. Mears, E. Rosenthal, and J.V. Sinka. Physical properties and virial coefficients of sulfur hexafluoride. *The Journal of Physical Chemistry*, 73:2254, 1969.

Vita

Chad Allen Greene always knew he'd be an engineer. Growing up in a small town in Virginia, he was raised to drink sweet iced tea and eat tomato sandwiches in the summertime, pick a mean banjo at the hootenannies, and always find a way to fix the family tractor when it broke down. It was one repair in particular, in which his cunning use of bailin' wire and twine convinced the townfolk that this boy was goin' places. Sure enough, in 2002, he graduated from the local high school and went into the the big city—*Richmond*—where he attended Virginia Commonwealth University for mechanical engineering and mathematics. Clever as he was, he proved himself a true college boy, earnin' a genuine diploma in 2007. It was then that he moved away, perhaps for good, in search of greater pursuits. Only time will tell if he'll ever go back... Only time will tell...

Permanent address: 814 Keasbey St.
Austin, Texas 78751

This thesis was typeset with LaTeX 2_ε by the author.